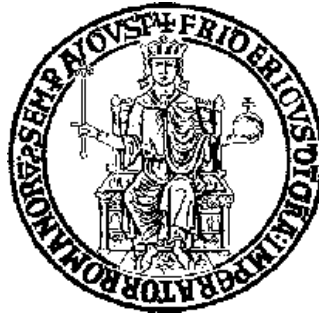


**University of Naples Federico II**

**Department of Chemical, Materials and Production Engineering**



PhD Program in

**INDUSTRIAL PRODUCT AND PROCESS ENGINEERING**

XXXV CYCLE

**Cold spray deposition of metallic coatings on polymers: analysis of process feasibility and coating properties**

**Advisor**

Prof. Antonello Astarita

**Co-Advisor**

Dr. Antonio Viscusi

**Ph.D Candidate**

Roberta Della Gatta



# Contents

<b>Abstract</b> .....	<b>4</b>
<b>CHAPTER 1 - Cold spray application on polymers and composite materials</b> .....	<b>6</b>
<b>1.1 Literature overview</b> .....	<b>6</b>
<b>1.2 Theories of bonding mechanisms in cold spray</b> .....	<b>11</b>
1.2.1 Bonding mechanisms on thermoplastic .....	14
1.2.2 Bonding mechanisms on thermosetting .....	16
1.2.3 Windows of deposition for polymers.....	18
1.2.4 Interlayer concept for bonding.....	22
<b>1.3 Process Parameters</b> .....	<b>23</b>
1.3.1 Feedstock powder.....	23
1.3.2 Gas pressure .....	26
1.3.3 Gas temperature.....	27
1.3.4 The surface morphology and the fiber influence .....	28
<b>1.4 Properties of the coatings</b> .....	<b>31</b>
1.4.1 Microhardness.....	31
1.4.2 Electrical conductivity.....	32
1.4.3 Adhesion .....	34
<b>CHAPTER 2 – Experimental campaign: manufacturing of substrates and cold spray deposition</b> ...	<b>35</b>
<b>2.1 Deposition of metallic coating on thermoplastic- matrix composite substrates</b> .....	<b>35</b>
2.1.1 Manufacturing of GFRP Composites .....	35
2.1.2 Cold Spray deposition.....	36
2.1.3 Coating Characterization .....	38
<b>2.2 Deposition of metallic coatings on PLA functionalized thermosetting composites</b> .....	<b>40</b>
2.2.1 Manufacturing of PLA functionalized thermosetting composites substrates .....	40
2.2.2 Cold Spray deposition.....	40
2.2.3 Coating Characterization .....	41
<b>2.3 Deposition of metallic coatings on 3D-printed substrate</b> .....	<b>42</b>
2.3.1 Manufacturing of 3D-printed substrate .....	42
2.3.2 Cold Spray deposition.....	47
2.3.3 Coating Characterization .....	48
<b>CHAPTER 3 - Cold-sprayed metallic coating on composite substrate</b> .....	<b>50</b>
<b>3.1 AlSi10Mg metallic coatings on GFRP with thermoplastic matrix</b> .....	<b>50</b>
3.1.1 Characteristics of AlSi10Mg coating.....	50
3.1.2 Influence of substrate manufacturing and process parameters.....	57
3.1.2.1 Effect of substrate layer thickness .....	57
3.1.2.2 Effect of process parameters .....	59
<b>3.2 Steel 316L metallic coatings on GFRP with thermoplastic matrix</b> .....	<b>62</b>

3.2.1 Characteristics of Steel coating .....	62
3.2.2 Influence of process parameters.....	67
3.2.2.1 Deposition mechanism.....	67
3.2.2.2 Effect of the laminate stratification.....	68
3.2.2.3 Effect of process parameters .....	68
<b>3.3 Thermosetting substrate.....</b>	<b>69</b>
3.3.1 Cold sprayed coating on PLA thermosetting composites .....	69
3.3.1.1 Analysis of the substrate .....	69
3.3.1.2 Indentation test results .....	71
<b>CHAPTER 4 - Cold-sprayed metallic coating on 3D- Printed Onyx substrates.....</b>	<b>76</b>
<b>4.1 Aluminum coating on Onyx substrate (different reinforcement infill).....</b>	<b>76</b>
4.1.1 Characteristics of the coatings.....	76
4.1.2 Effects of panels characteristics and process parameters .....	80
4.1.2.1 Effects of the surface texturing.....	80
4.1.2.2 Effects of the panels' manufacturing strategy on CS deposition.....	80
<b>4.2 Onyx substrate (different matrix infill) .....</b>	<b>82</b>
4.2.1 Characteristics of the panel substrate .....	82
4.2.1.1 Substrate Morphology.....	82
4.2.1.2 Substrate distortion .....	84
4.2.2 Characteristics of the coatings.....	86
4.2.3 Effects of panels characteristics and process parameters .....	90
4.2.3.1 Effect of fibres .....	90
4.2.3.2 Effect of the infill density.....	91
4.2.3.3 Effect of the superficial matrix layer thickness .....	93
<b>CHAPTER 5 – Model development .....</b>	<b>94</b>
<b>5.1 Introduction to the model .....</b>	<b>94</b>
<b>5.2 Model development .....</b>	<b>96</b>
5.2.1 Calculation of $E_p$ .....	96
5.2.2 Calculation of $E_a$ .....	97
5.2.3 Model formulation.....	103
<b>5.3 Materials and methods for experimental validation .....</b>	<b>104</b>
<b>5.4 Results.....</b>	<b>108</b>
5.4.1 Model validation.....	108
5.4.2 Application of the model to literature cases.....	112
<b>5.5 Discussion .....</b>	<b>114</b>
5.5.1. Adhesion mechanism .....	114
5.5.2. Role of the fibers.....	115
5.5.3 Predictive simulations through Vi-Pe-R-A equation .....	116

5.5.4 Influence of the fiber volume percentage within the composite substrate .....	119
<b>Conclusion</b> .....	<b>121</b>
<b>References</b> .....	<b>123</b>

## **Abstract**

Nowadays, the consumption of polymeric materials and polymeric matrix composite materials is increasing because of the many advantages of polymeric materials compared to other materials, such as metals or ceramics. They are widely used in aerospace and military due to their low density, high specific strength and rigidity, and other noteworthy properties such as ease of formability and machining. Although these materials have various benefits, some more applications are still precluded because bulk polymers cannot guarantee appropriate electrical conductivity, erosion resistance, and high operating temperature. To give these materials such properties, their metallization with an additive manufacturing technique appears to be a promising solution to wide their applications. Among different techniques, the Cold Spray one can be considered the most prominent. The Cold Gas Dynamic Spray generally referred Cold Spray (CS), is a relatively new spray technology that falls under the larger family of thermal spray processes. The cold spray uses less thermal and more kinetic energy, so the powder particles remain in a solid-state upon impact with the substrate. During CS depositions, upon particles' impact with the target surface, a conversion of kinetic energy into plastic deformation occurs, and the solid particles deform and bond together for the coating formation and growth. Therefore, it can cope with the production of different kinds of coatings, pure metals, alloys, composites, nanostructured materials as well as amorphous materials, on a wide variety of substrates. Although this technique is widely used to create coatings on metals, its implementation on polymers and FRPs is relatively new. The experimental evidence of cold spray deposition of metal particles on polymers has been proved, but all the involved phenomena are not clear. To date, despite the rich excess of approaches dealing with which is the best strategy to achieve adhesion, the wide range of materials and parameters make it difficult to identify which is the best strategy to follow, and the phenomena that govern the adhesion are not clear. It is known that PMCs metallization's quality through cold spray depends on substrate typology and stratification, which in turn, depend on PMCs manufacturing processes. Anyway, the manufacturing of the substrate is usually not considered, and the influence of the fibre is not well understood. Therefore, the customization of PMCs to be used as substrates for the cold spray deposition is crucial, the target surface should be designed and manufactured to fit better the cold spray requirements. Also, there is no model in the literature that aims to thoroughly examine and explain the phenomena that lead to the adhesion of metallic particles on composite substrates. On this basis, this thesis aims to give a complete knowledge of the Cold Spray process, trying to understand why certain phenomena occur and answer the main unsolved questions about the subject matter: (i) Is it possible to achieve deposition on all the substrates? (ii) What are the main phenomena occurring because of the impact of a particle on a composite

substrate? (iii) How can the stratification of the composite and the fiber typology contribute to the effectiveness of CS depositions? (iv) Which is the role of the reinforcement when spraying on composites? (iv) is it possible to model the process? To answer all these questions, a complete study of the process is required starting from an interpretation of the phenomena occurring to the manufacturing of the substrate and the optimization of process parameters. The aim of the doctoral project is therefore to resolve the open questions about this type of process. A comprehensive approach has been proposed by considering three main research flows to be developed at the same time: to develop a numerical model that makes us able to understand the physical mechanisms that regulate adhesion between polymer and metals; provide guides for the choice of process parameters closely related to the choice of materials so that we can also achieve adequate growth of the coating; customized realization of the substrate so that we can identify the best strategy for a panel to be coated. For these two-last purposes, in the experimental set-up, both the layup sequence and stratification of the substrates and the manufacturing technology and the cold spray process parameters were varied to study the manufacturing process in its wholeness. The three flows are closely linked: since the mechanisms are not clear, the feasibility of the process for different substrate/powder pairs cannot be predicted and experimental work is necessary. To achieve these goals, this thesis aims: to find the best process and strategies for the manufacturing of the substrate, optimize process parameters and provide an interpretation of the phenomena occurring during cold spraying though the development of an interpretative model able to clarify and discuss what are the involved phenomena.

In the first chapter of this work, a wide literature overview of the cold spray process and its application to composite materials will be shown, highlighting all the gaps presented in the literature. In the second chapter, the manufacturing of the substrates used for the experimental campaign and the cold spray process parameters used for the deposition will be widely discussed for each combination. Three different types of substrates are analyzed: thermoplastic substrates, thermosetting substrates and 3D-printed substrates. In the third- and fourth-chapter analysis of the feasibility of the cold spray process and analysis of the influence of process parameters, substrate material and manufacturing will be extensively discussed. In the fifth chapter, a preliminary development of an analytic model has been proposed to analyze and clarify which phenomena occur as a result of the impact of a particle on a composite substrate that leads to the coating formation.

# CHAPTER 1 - Cold spray application on polymers and composite materials

## 1.1 Literature overview

In the last decade, the research community, as well as manufacturing industries, are focusing their attention on additive manufacturing processes [1]. Under the terms of additive manufacturing, several different technologies, based on the common concept of obtaining a final part by the addition, layer by layer, of feedstock material, can be represented. These techniques offer a broad range of intriguing possibilities, and their full potential is far to be completely exploited, so the research stream is continuously increasing and seems to be endless. In this context, the Cold Gas Dynamic Spray (CS) technique, which is outlined in the wider family of thermal processes, can be fully framed in the category of additive manufacturing technologies [2]. The operating principle ruling the thermal spray processes, i.e. wire arc [3, 4] and flame spray [5], is that the particles dragged by a carrier gas are heated to the material melting point and deposited onto the target substrate to be coated [6]. However, contrary to these above-mentioned processes, in the cold spray, the particles rely more on kinetic energy than thermal energy and remain in a solid state throughout the process [7]. Briefly, the particles are accelerated to high velocities (ranging from 300-1200 m s<sup>-1</sup>) by a supersonic carrier gas (air, nitrogen, helium, or mixtures of the above) in a de Laval nozzle, then exit from the nozzle at high velocities, impact the substrate, undergo significant plastic deformation, and bond together with the substrate [8]. Successful deposition of the coating requires that the particles exceed a threshold impact velocity, called critical velocity [9].

The use of protective and functional thermal-sprayed coatings is a low-cost method to improve the superficial properties of the material or to prolong the lifetime of the components [10]. Since its initial stages, the cold spray has been employed to produce metallic coatings on metallic substrates, and the deposition of various powders on various substrates has been investigated. The comprehension of the complex phenomena ruling the adhesion of the impinging particles on the substrates has requested many years and a lot of experimental work. The most prevailing hypotheses on the bonding mechanisms are mainly related to interfacial restructuring or amorphization, mechanical interlocking, oxide-layer break-up, and adiabatic shear instability [11]. It is worth noting that the actual bonding mechanism for cold spray particles is still a debated topic under the recent focus of investigations. In fact, in a very recent work, Hassani et al. [12] affirmed that adiabatic shear instability is not essential for coating formation.

In the last years, most of the interest of the additive manufacturing community has been devoted to the fabrication of hybrid structures [13–15] to meet the more demanding requirements of the

aerospace and automotive industries [16]. In this scenario, a lot of researchers of cold spray tried to produce metallic coatings on polymeric substrates to couple the lightweight polymers with the wear resistance, physical properties and hardness of metals [17–19]. Several applications of polymers and polymer matrix composites, such as CFRPs (carbon fiber-reinforced polymers) or GFRPs (glass fiber-reinforced polymers), are still excluded, to date, because they are not capable to ensure some specific properties successfully, such as electrical conductivity, electromagnetic shielding, thermal conductivity, erosion, radiation, and lightning protection. To this end, the metallization of the polymer-based substrates can represent the potential solution to give these materials the above-mentioned properties.

Compared to other techniques, the cold spray offers some intriguing advantages when spraying metallic particles on polymeric or FRPs substrates: (i) the deposition is made possible by only a mechanical interlocking mechanism, and no chemical reactions are required to take place between the particles and the substrate that would be almost impossible between a metal and a polymer; (ii) suitability of powder granulometry's is less restrictive than for conventional thermal spraying. Then, cold spraying covers a broader range of powder sizes, i.e., from micron down to submicron; (iii) compared with thermal spray processes, less heat input is required in the cold spray so that the powders can retain their primary properties during deposition.

As a low-temperature process, since the gas temperature remains below the melting point of the particle's material, CS can minimize the causes of evaporation, oxidation and other frequent issues related to thermal spray processes [20]. Hence, it is obvious that CS represents a potential solution for temperature-sensitive materials; it can be used for the manufacturing of various types of coatings, such as pure metals, alloys, polymers, nanostructured materials as well as amorphous materials [21, 22] on a variety of substrates, including composites and plastics.

The study of the cold spray method for the metallization of polymers is still in its early stage and the deposition mechanisms of metals on polymer-based materials are not thoroughly understood yet. In literature, an increasing number of papers is available, as summarized in Fig. 1.

Polymers and fibre-reinforced polymers (FRPs) are gaining interest due to their specific properties in various fields, such as aerospace and military [23–25]. Several applications of these materials are still excluded, to date, because they are not capable to ensure some specific properties successfully, such as electrical conductivity, electromagnetic shielding, thermal conductivity, erosion, radiation, and lightning protection [26–30]. To this end, the metallization of the polymer-based substrates can represent the potential solution to give them the above-mentioned properties. There exist various conventional methods such as PVD [31] or CVD [32, 33], electroplating [34], electroforming [35], and thermal spraying processes that can be used for the surface metallization

of polymers and FRPs [36]. However, these techniques suffer from a series of disadvantages, for instance, the high equipment and processing costs, and the size limitations of the workpieces are some of the drawbacks characterizing the former two.

For this purpose, cold spray technology appears to be a promising technique for the metallization of polymers and fibre-reinforced polymers due to its peculiar assets such as low operating temperature and low maintenance costs [37]. There exist two kinds of equipment based on the cold spray technology that are classified generally on the gas pressure values involved for the acceleration of the particles: i) the high-pressure cold spray (HPCS) and ii) the low-pressure cold spray (LPCS). The working schemes of both the processes are shown in Fig. 2a and b, respectively. As it can be seen from Fig. 2a, in the HPCS processes, the compressed gas typically helium, nitrogen, or air, is divided into two gas streams. The former, at room temperature, is fed by the powder feedstock material in form of fine particles (powder mean size in the range of 1-50  $\mu\text{m}$  [38]) which are accelerated through a powder injection tube into a convergent-divergent de Laval nozzle. At the same time, the latter (that is the main gas stream) is heated up to elevated temperature by an electric heater and introduced into the nozzle at high pressure, where the heated gas and the powder are mixed. The gas-powder mixture is accelerated through the nozzle to supersonic conditions [39].

In LPCS processes, as schematically shown in Fig. 2b, the compressed gas is heated up in an electric heater and directly injected into the de Laval nozzle. The injection point is in the nozzle divergent section where the local gas pressure is sufficiently low to take advantage of the Venturi effect experienced by the gas in that section. This allows the powder to be delivered from the powder feeder at room pressure into the carrier gas. These differences make the low-pressure cold spray systems more flexible and not expensive compared to high-pressure ones. Also, due to the lower pressure values of the gas involved in the LPCS system, this latest equipment is more suitable for the metallization of soft materials, like polymers.

From a wide literature analysis, as reported in Table 1, it can be pointed out that quite different approaches have been used to metallize the polymers through the cold spray. In general, most authors investigated different values of cold spray process parameters for the deposition in terms of gas temperature and pressure and standoff distance (which is the distance between the exit of the nozzle and the substrate surface, (SoD)) and for different combinations of substrate and powder types. For the same powder/substrate configuration, the depositions were made at room temperature as well as at 100 °C, at low pressures and higher-pressure values, and so on.

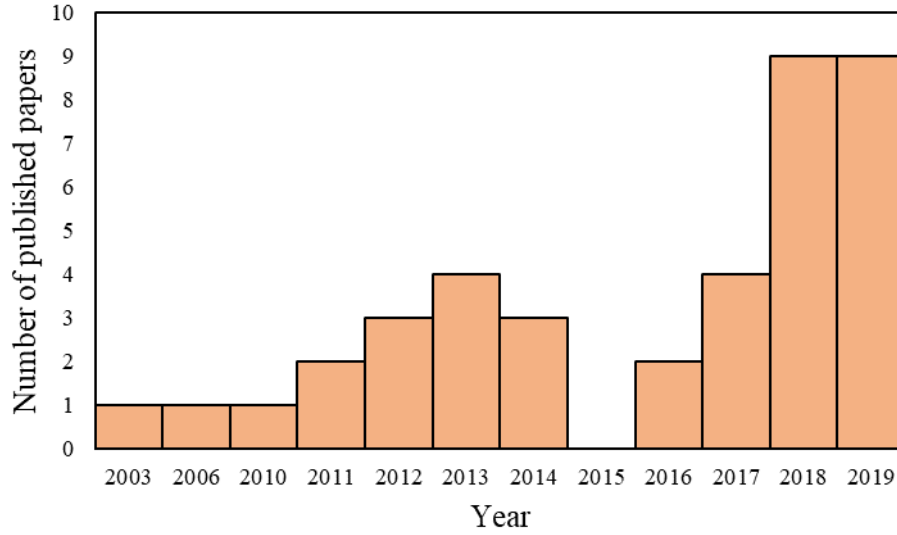


**Fig. 1** - Number of published papers

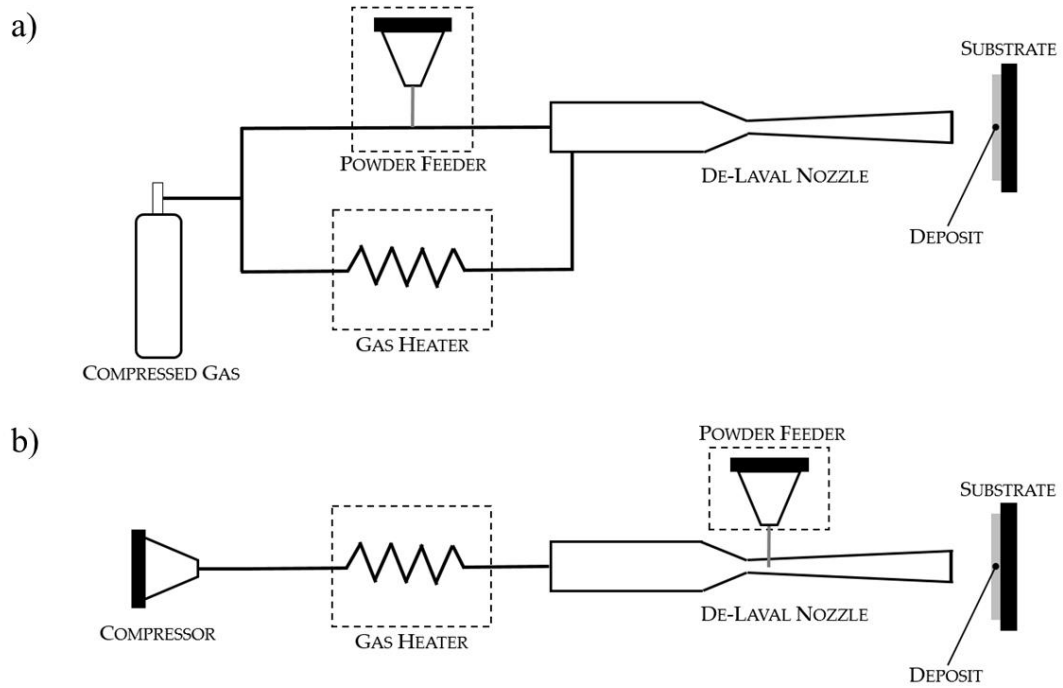


**Fig. 2** Working schemes of high-pressure **a** and low-pressure **b** cold spray

**Table 1** - List of papers on CS deposition on polymers in the last until 2019

Year	Substrate type	Powder Type	Gas Temperature [°C]	Gas Pressure [MPa]	SoD [mm]	Ref
2019	PEEK-PEI-ABS	AL7075,CP Al	225 to 450	0,31 to 0,48	25 to 102	[57]
2019	Hemp-PLA	Al-Si12 + 0, 15, 30, and 45% Al2O3 wt. %.	100	0,7	50	[58]
2019	CFRP	Cu – 0.1% Ag	330	0,8	30	[59]
2019	ABS-PEEK-PEI-CFRP- Steel	Cu	250 to 550	2	40	[60]
2019	GFRP	Al	160	0,5-0,6	20-25-35	[61]
2019	CFRP	mixed SS/Fe mixed Cu Zn Sn	300	0,3-0,5-1,4	18	[62]
2019	BS/PA6	AlSi12	150 to 600	0,4-0,8	10 to 80	[63]
2019	CFRP	Mixed Al -Cu-Zn	300 to 500	0.4	10-20	[64]
2019	CFRP	AlSi12	150	0,6	20 to 35	[17]
2018	CFRP	Sn-10 wt. % Cu)	300	0,41	18	[65]
2018	PEEK	Cu	300	1,2-1,6-2-2,4	30	[66]
2018	HDPE -ptfe	Cu	room	0,5 to 3	40	[67]
2018	Polycarbonate	Al, Sn, mixed Al-Sn	200-400	0,5-0,9	10-15-30	[68]
2018	Polystyrene	Ti	600	2,8	30	[69]
2018	CFRP	Sn-10 wt. % Zn Sn-10 wt. % Al	280-300	0,41 to 0,7	18	[70]
2018	CFRP-ABS-PEI-PEEK	Cu-Sn-Fe	200-445	0,3-0,5-1,4	18	[71]
2018	CFRP (PEEK)	mixed Cu-PEEK	-	-	-	[72]
2018	Hemp-PLA	AlSi12	150 to 600	0,4 to 0,8	10 to 80	[18]
2017	CFRP – THERMOSET	mixed Cu-Zn-Sn	280–300-350	0,41–0,55-0,69	18	[73]
2017	PEEK	Al	427	23	40	[74]
2017	PA6	mixed Sn + Al2O3, Cu	200-300	0,9	10	[75]
2017	CFRP	Cu-Sn	25 to 425	0,29 to 1,39	18	[76]
2016	HDPE -PTFE	Cu	room	0,5 to 3	40	[77]
2016	CFRP	Mixed PEEK-Cu	300 to 500	1-1,5-2	80	[19]
2014	Lexan	A5001	140	1,25	15	[78]
2014	PEEK	Ti	-	-	-	[79]
2014	HDPE	Mixed Cu-Zn-Sn	150	2,5	55	[80]
2013	Epoxy-PVC	Ti-Cu	100 to 400	1,0-2,0-3,0	30	[81]
2013	PEEK	Ti	-	-	-	[82]
2013	Nylon 6 -PU - PTFE - HDPE - PP - PC	Cu	150 to 350	2,5	30	[83]
2013	PU	Cu	400	2,5	30	[84]
2012	PVC	Cu,Tin	100 to 400	1,0-2,0-3,0	30	[85]
2012	HDPE - Nylon 6	Cu	100	2	30	[86]

2012	PA 66	Al	150 to 300	1,5 to 3	40	[87]
2011	CFRP	Sn	300-600	0,5-2	150	[88]
2011	CFRP	Al-Cu	300-450	1,2-1,9	15-20	[89]
2010	PC-ABS-PS-PP-GFRP	Al, Cu, Tin	300	0,5-3	40	[90]
2006	CFRP	Si	300	2	40	[91]
2003	ABS	Al	Room	2,5	20	[92]

It can be seen that the most used powders are Cu, particularly affine to biomedical applications, and softer materials like aluminium or tin, which are more prone to be deposited due to lower energy generated upon the impact on the surface. In fact, only a few works are focused on the use of harder powder materials, such as steel, owing to the major difficulties encountered in the deposition, which resulted in erosion of the polymeric substrate. A wide assortment of substrates is used as well. In particular, PEEK, ABS, HDPE and PEI are mostly used for their properties, which combine adequate stiffness, lightweight and greater deformation than epoxy ones. Anyway, the latest research, as reported in Table 1, are focusing on the application of the cold spray process on CFRPs and GFRPs. These materials are more requested, especially in aerospace applications, for their higher mechanical properties compared to the bulk polymer [76, 77]. Due to their higher mechanical properties, CFRP [78] and GFRP [79] materials are widely used with both thermoplastic and thermosetting materials as the matrix.

To sum up, the presence of these combinations of various parameters and the absence of optimal spraying conditions suggests that the mechanisms ruling the adhesion are not known, so a trial-and-error approach was used instead of one based on theoretical considerations.

## 1.2 Theories of bonding mechanisms in cold spray

The bonding between the cold sprayed powders and the metallic substrate has been extensively analyzed in literature [80, 81]; the scientific community agrees in attributing the bonding process to two different mechanisms, known as mechanical interlocking and metallurgical bonding [82]. The former refers to the mechanical embedding of the particles into the substrate material without considering chemical interactions between the powder and the substrate. This is due mainly to the mutual deformation of both the particles and the impacted substrate. In contrast, metallurgical bonding occurs at the particle-to-particle and particle-to-substrate interfaces due to chemical interactions attributable to the nature of both the powder and the substrate. In addition, it is generally accepted that the predominant

phenomenon ruling the metallurgical bonding is the adiabatic shear instability [83] that occurs at the particle-substrate interface: the particles impact the substrate leading to the jetting formation, and the oxide layer surrounding the particles is destroyed, and a pure metal-to-metal bond is achieved, resulting in greater deformation of the particles. Note that it is the jetting that leads to the bonding due to a high deformation rate at the particle-substrate interface [84].

Under these conditions, the metallurgical bonding for cold spray, which is connected to adiabatic shear instability to occur, is limited to the metallic substrate; that means that the only possible bonding mechanism for the polymer substrate is the mechanical interlocking. Before investigating in detail the mechanical interlocking mechanisms taking place when metallic particles impact the polymer-based substrates, it is worth noting that the polymers cover a wide range of material types, and their behaviour depends on the chemical structure of the polymer itself.

Polymeric materials are classified into two main categories: i) thermoplastic and ii) thermosetting [85]. Although these two types of polymers may appear similar, their structural properties are different. Thermoplastics, simply called plastics, consist of linear or branched polymer chains that can become soft when they are heated and hard if they are cooled. On the other hand, thermosets contain polymer chains organized in a network structure formed during the curing process as a result of an irreversible chemical reaction [86]. The main difference is that the thermoplastic polymers can be melted leading to a liquid physic state to be processed, without inducing any deterioration of the material; contrary, the thermosetting plastics cannot be re-melted after the curing process but instead remain in a solid state and deteriorate when the temperature is increased.

In the optics of the cold spray deposition and based on the main bonding mechanisms above described, the bonding can be achieved successfully for ductile materials, meaning that the ductile nature of thermoplastics promotes the particle anchoring and the CS deposition.

On this subject, Ganesan et al. [64] were the first authors who tried to explain the difference between the behaviour of these two types of polymers upon the impact of cold sprayed particles. Fig. 3 shows the first attempt at a schematic representation of a spherical copper particle interacting with a thermoplastic PVC substrate (Fig. 3a) and an epoxy-based surface (Fig. 3b). The authors found that the accelerated copper particles can penetrate deep into the PVC substrate with the surrounding polymer that covers the particle, and in this way, the interlocking mechanism is promoted.

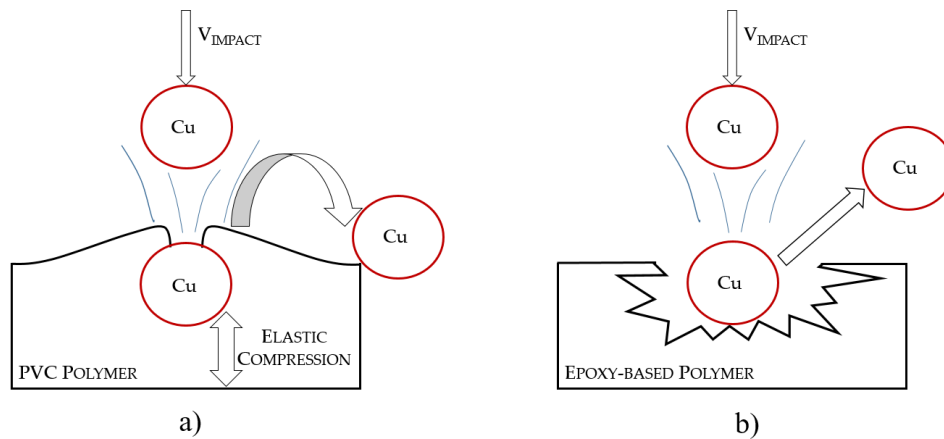


**Fig. 3** - Schematic representation of the interaction of a cold-sprayed Cu particle on **a** PVC, **b** epoxy resin [64]

As it is known in the literature, in cold spray depositions, the particles can be trapped by the surrounding softer substrate if the substrate materials are softer or less dense than the sprayed particles [87]; this is the behaviour experienced by the thermoplastic substrates (Fig. 3a). In contrast, for the epoxy-based substrates, the high-velocity impact of the particle (the copper particle in Fig. 3b), results in a brittle fracture in the impact region, leaving a wider crater where the copper particles simply stick due to the fragile behaviour of the polymer.

Similar results were obtained by Lupoi et al. [60], who analyzed the deposition on thermoplastic and thermosetting substrates under the same spraying conditions. The copper powders were cold sprayed on high-density polyethylene (HDPE) and polytetrafluoroethylene (PTFE), which are thermoplastic and thermosetting polymers, respectively, as shown in Fig. 4.

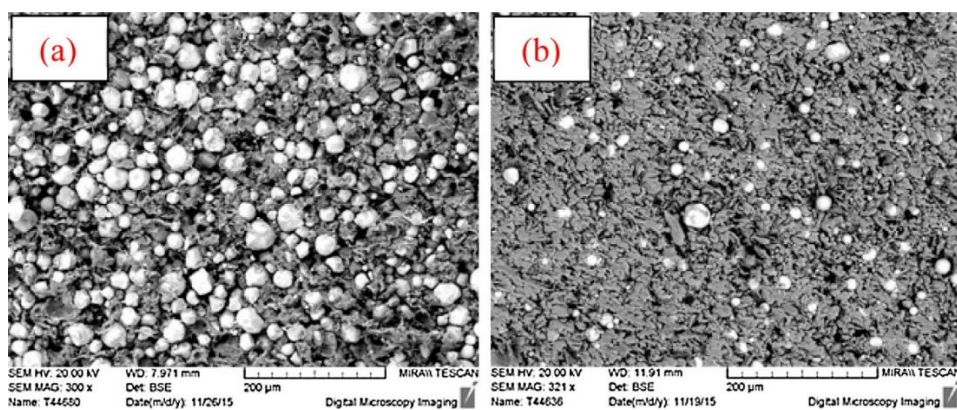


**Fig. 4** - SEM images of cold sprayed Cu powder on **a** HDPE and **b** PTFE [60]

In both cases, the deposition efficiency (DE) of the process was analyzed. It was found a higher value of DE for the thermoplastic panels, because the polymer matrix, despite being bombarded at the surface, showed to be able to maintain a continuous structure capable of holding the particles.

On the thermosetting substrate, the particles bounced off and created empty craters on the surface. The particle bombardment resulted in a shattering of the thermoset surface, indicating that the conditions were less suitable for a high degree of particle impregnation. In the next sections, a deeper analysis of the bonding theories associated with the two polymer types will be discussed separately.

### *1.2.1 Bonding mechanisms on thermoplastic*

The deposition of metallic particles through cold spray is more successful with thermoplastic substrates due to their ductile nature [88]. The most used thermoplastic materials for CS applications are ABS, PEEK, PVC, HDPE, and PP.

King et al. [66] used the cold spray technology to embed copper particles into 6 different polymers finding that the substrate deformation is caused by the combination of two main factors: thermal softening and particle impact energy. Upon impact, the substrate undergoes a rapid plastic deformation which induces a rapid local temperature rise that promotes the substrate softening and the formation of mechanical interlocking within the substrate.

Due to the different properties like hardness and density of the particle/substrate materials, the particles penetrate the softer and less dense substrate, resulting in the dissipation of the kinetic energy of the impacting particle. This behaviour can be related to hard/soft metal bonding proposed by Bae et al. [89], where the plastic dissipation was induced by an adiabatic temperature rise. In the case of a thermoplastic substrate, it is obvious that this phenomenon depends on the intrinsic properties of the material, in particular on the glass transition temperature of the material, indicated as  $T_g$ . The glass transition temperature is a temperature above which the polymer changes from a visco-elastic state to a rubber state and loses some of its stiffness, which is caused by the sliding of the polymer chains [90]. When the temperature experienced by the polymer is above  $T_g$ , the substrate is more inclined to deform, the particles anchored to the substrate leading to an increase in the deposition efficiency. When the temperature is much lower than the glass transition one, the polymer is relatively hard and brittle and the deposition is difficult to be achieved. A further condition is when the temperature is significantly higher than  $T_g$ ; in this case, due to the drastic lowering of the polymer strength, the deposition becomes complicated again, as it is easy to erode the substrate under these conditions.

Experimental tests conducted by Che et al. [54] have proved these phenomena; an example is the cold sprayed copper particles on ABS substrate by setting a carrier gas temperature at 425 °C (Fig. 5a).

Under these conditions, the particles impacting the surface can reach an impact temperature that exceeds 200 °C, which is far beyond the glass transition temperature of the polymer. The result is an extensive deterioration of ABS strength and erosion of the substrate itself. On the contrary, successful results can be obtained with the relatively more performant PEEK material (Fig. 5b) if it is coated with copper particles at 425 °C. The studies carried out by Chen et al. [49] corroborated the above-described mechanisms. The authors analyzed the impact of a single Cu particle on PEEK. Besides, the FEA modelling was developed to give more insights into the bonding mechanisms during metal/polymer bonding. It was observed that the material jet of PEEK substrate formed by the penetration of Cu particle is more evident as the propelling gas pressure increases, which causes the severe plastic deformation of the substrate side. The deformation features of PEEK substrate have a good consistency with the experimental observation of the single particle morphology. The high-temperature zone can be noticed from Fig. 6 at the contact zone, where localized plastic deformation occurred, for all the examined gas pressure values. Such phenomena were owing to the plastic dissipation induced adiabatic temperature rise, which is frequently found in the bonding between hard/soft metals, as explained before [89].

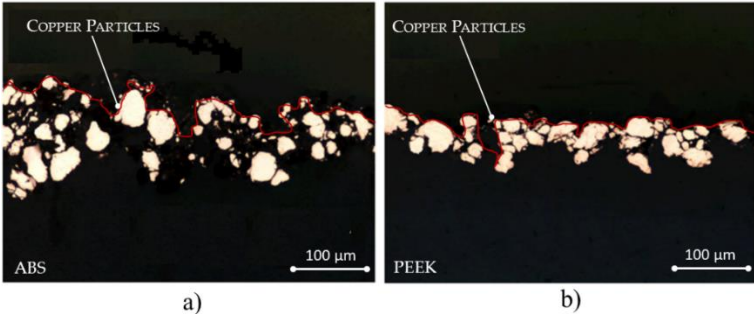


**Fig. 5** - Optical micrographs of cold sprayed Cu coatings at 425 °C at 1.0 MPa on **a** ABS and **b** PEEK [54]

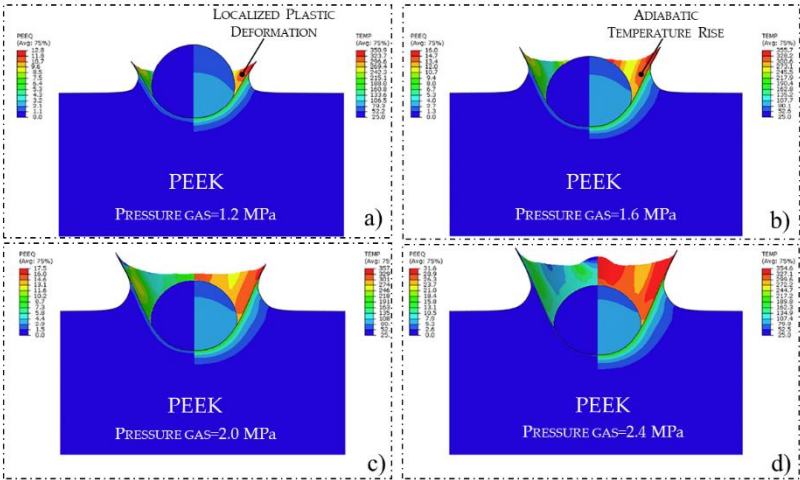


**Fig. 6** - Distribution of temperature and effective plastic strain of a single Cu particle depositing onto PEEK substrate at different gas pressures [49]

It is possible to note that the temperature in the jetting zone is higher than the glass transition temperature of the PEEK, which is nearby 143 °C: the result is that as the temperature overcomes the glass transition point, the polymer material will pass in a viscous state from a brittle one. The accompanying plastic dissipation induced temperature to rise rapidly, softening the PEEK substrate and promoting the formation of mechanical interlocking that captures the deposited particle within the substrate.

### *1.2.2 Bonding mechanisms on thermosetting*

Thermosetting polymers start to degrade when heated-up, due to their intrinsic nature. Their properties change with the operating temperature and the behavior is usually brittle and fragile [91]. Because of these properties, the deposition of cold sprayed powder results difficult, especially at higher impact energies, and therefore the mechanical interlocking is not easy to be attained.

As proved by Che et al. [56], the particle cannot undergo severe plastic deformation after the impact to the thermosetting substrates for relatively low velocities. On the opposite, when the particles impact at high velocities, the substrate is damaged. The cause of this behavior is attributed to the low erosion resistance and fragile behavior of the thermoset polymers, thus the high-velocity particles contribute to the substrate fracture and consequent void formation rather than the deposition. Similar observations were found by the same authors [43]. Looking at Fig. 7, it is possible to notice cavities in the CFRP substrate at the impact spots, which is a sign of erosion, with the particles that are not firmly interlocked with the substrate.

However, in this work [92] was proved that relatively soft materials like tin can be deposited successfully on epoxy-based substrates and, based on the results, the authors proposed a theory to explain the bonding mechanisms for this powder/substrate combination. This theory, based on “crack-filling mechanism” is explained below. When the soft particles (like tin) are injected into the hot carrier gas, the surface of these particles begins to melt. Due to the short residence time in the nozzle, the particles cannot melt before they exit the nozzle, so the cores of particles remain solid. When these particles impact the brittle substrate, many micro-cracks in the surface epoxy are generated. Then, the molten external part of the particles is forced into these cracks to fill and solidify. In this way, the mechanical anchorage of this first layer is high enough to avoid further erosion. Then, the upcoming particles impact this first layer and build-up a coating. With this mechanism, melting is a crucial factor, therefore, it does not apply to materials that have high melting points and would erode the CFRP before bonding. A schematization of the crack filling mechanism is shown in Fig. 8.

After the deposition of the first layer, the build-up of the coatings with subsequent layers is differentiated [54]. In the light of further studies [93, 94], it has been proved that, in the case of CFRP with epoxy matrix, the presence of these micro-cracks is more likely to be observed around the carbon fiber area and not on the pure polymer surface.

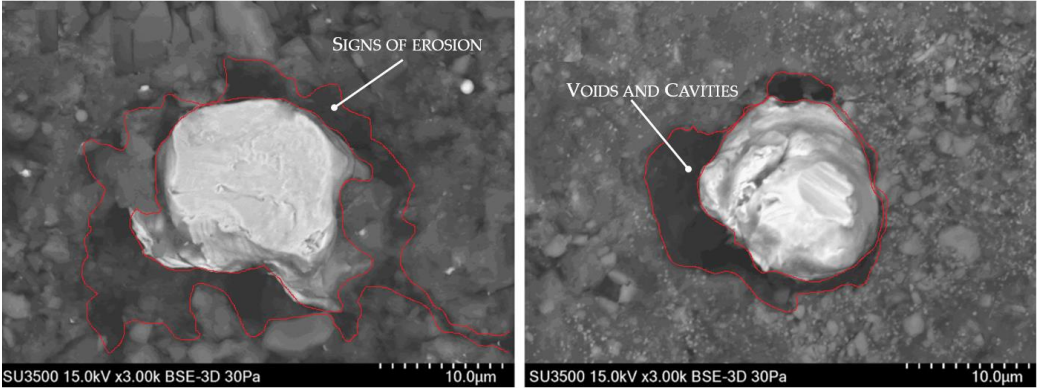


**Fig. 7 - SEM images showing voids and cavities at the impact spots on CFRP substrate left by copper particles at two different gas temperatures: 425 °C (on the left) and 250 °C (on the right) [43]**

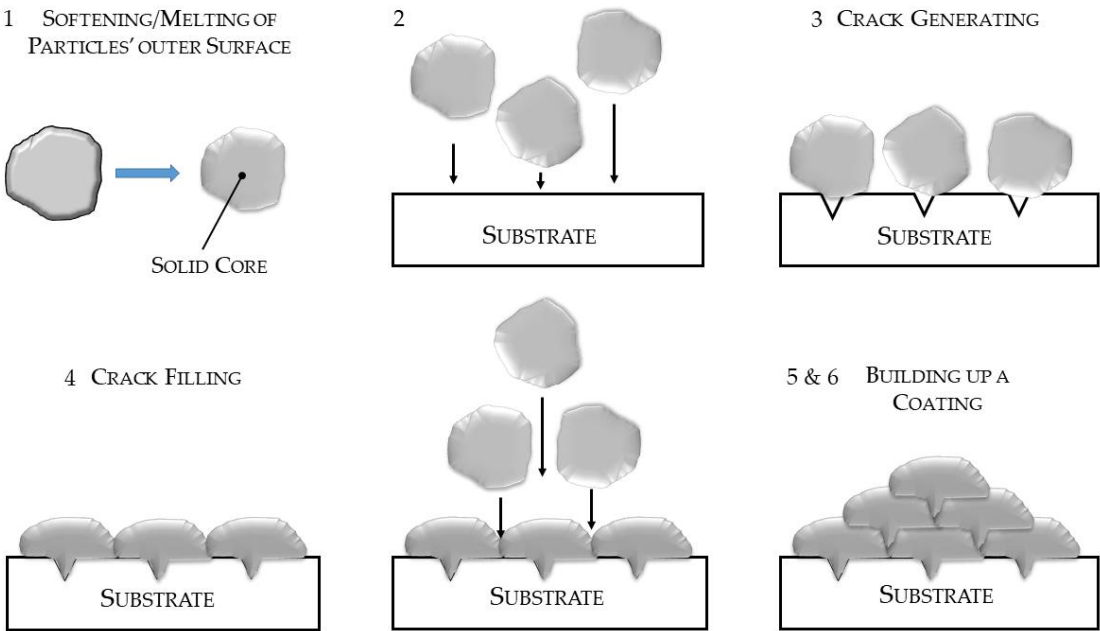


**Fig. 8 - The schematization of crack filling mechanism for thermosetting bonding [92]**

This theory of the suggested “crack-filling” mechanism can be observed by the crack occurring on the surface, as presented in Fig. 9, suggesting the potential bonding of the metallic tin directly with the carbon fibre [94].

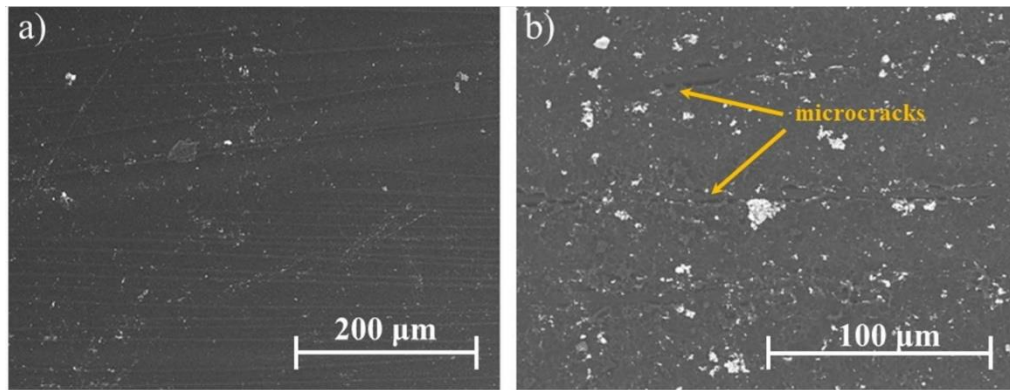


**Fig. 9** - SEM acquisition of a Sn-10Al5083 coating on CFRP **a** before spraying and **b** after spraying and peeling [94]

### *1.2.3 Windows of deposition for polymers*

From the above-reported discussion on the influence of the substrate typology on CS bonding mechanisms, it is evident that different responses are expected by the coating process depending on the nature of the impacted surface.

The bonding mechanisms involved when the metal particles impact the polymers are strictly dependent on the powder/substrate properties; moreover, it appears clear that, after the formation of the first layer, the subsequent particles go to impact a metallic surface and different bonding phenomena occur when the critical velocity is properly set. Based on these premises, a detailed discussion on the main issues involving the critical velocity [95] and the cold spray deposition window [96] related to the cold spray deposition on polymers needs to be carried out.

First of all, the deposition of cold sprayed coating can be divided into two different steps: i) firstly, the deposition of the first layer and then ii) the coating build-up, in agreement with the impacting surface typology. For the first layer, the interaction is between particles and the surface and the adhesion of this layer is significant for the adhesion strength of the coating. The subsequent particles impacting the substrate start to build-up the coating upon the first deposited layer. The particles firstly impact the polymeric surface and then with the metallic coating. Since the deposition of metals on polymers is also dependent on the substrate properties, the conventional deposition rules developed for the metallic substrate by assuming that the particle and substrate materials are identical are not applicable in the case of polymer substrates [97]. Consequently, two different windows of depositions should be identified, one for the first layer and another one for the coating build-up. The deposition of the first layer is dependent on both the cold sprayability of the metal powder and the substrate properties, mainly the  $T_g$  of the polymer. Also, less impact energy is required for the particle-substrate polymer while for the bonding between the first

sprayed layer and the subsequent particles a higher energy input is required to activate the metallurgical bonding [98].

All the above-mentioned conditions have been summed up by Che et al. [93] and shown in Fig. 10. The phenomenon that rules the deposition of the first layer is only the mechanical interlocking (as discussed above extensively) since there is no metallurgical bonding. This implies that the particles have to reach a sufficiently high velocity, defined as  $v_{int}$ , that is the velocity above which the particle interlock with the substrate, without exceeding the erosion velocity,  $v_{ero,pl}$ , that is the velocity above which the particle erode the substrate. On the other hand, the window of deposition for the build-up process is limited by  $v_{crit}$ , which is the critical velocity of the material powder type, and  $v_{ero}$ , which is the velocity above which the particles are not deposited and previous layer are eroded.

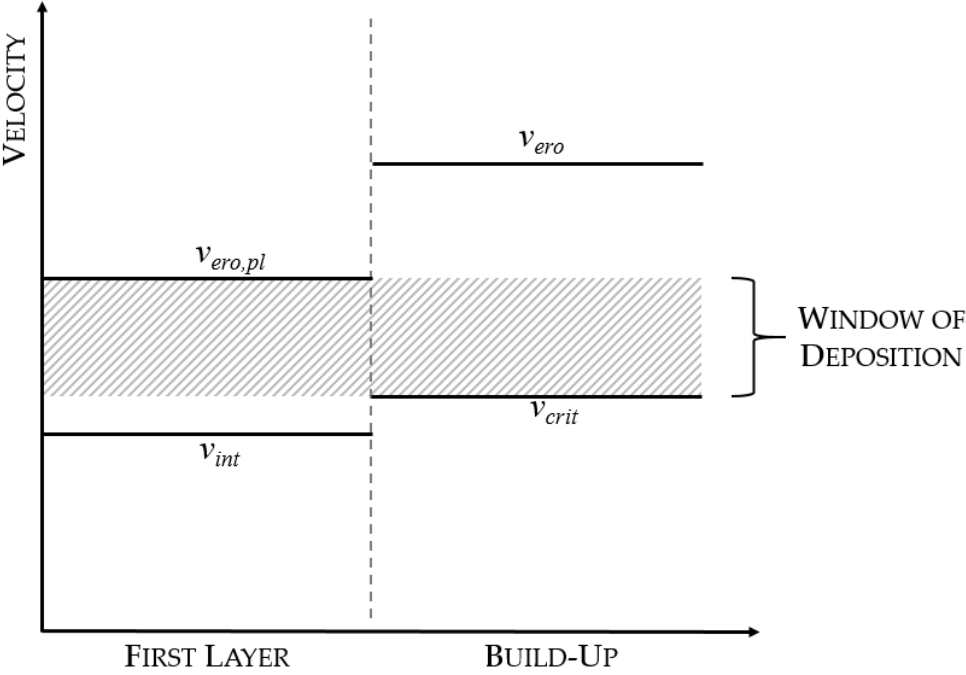


**Fig. 10** - Schematization of the cold spray window of deposition for polymer [93]

While the window for the build-up process is compared to the conventional cold spray window of metal powder, regardless of the metallic substrates (the values can be taken from the literature or calculated theoretically), for the first layer the window should be experimentally calculated. Physical properties of both the metal powders and the substrate and the chosen CS process parameters must be considered. Therefore, the process parameters should be set to meet the two windows of deposition at the same time. This implies that the particle velocity must exceed the

critical velocity of the metal powder but cannot exceed the limit above which the first layer will be eroded. Nevertheless, the deposition becomes extremely narrowed and challenging.

Anyway, following the cold spray depositions of various Sn/Al mixtures, Liberati et al. [99] observed unusual coating morphologies attributed to different phases of the deposition. These authors proved that, depending on the gas pressure, two distinct deposition levels can be obtained: a direct deposition effect, described above for the deposition of the first layer, and an indirect deposition effect.

When the powder velocities are close to the erosion velocity, some peculiar phenomena can be observed. As shown schematically in Fig. 11a, the particles that reach velocities higher than the relative erosion velocity,  $v_{ero}$ , can rebound on the substrate and then a small fraction of rebounded powders may be re-deposited in the boundary of the main spray area. These powders can rebound from the substrate, come back into the gas stream, and then accelerated to a lower velocity (in the same deposition window), leading to a possible redeposition of the powders.

As the gas pressure increases, this re-deposition effect would be predominant as more particles achieve velocities above the erosion one (Fig. 11b). When the powders hit the substrate, they can be moved across by the gas flow rather than bounce back, gradually lose speed and reenter into the deposition window.

From these considerations, it is relevant that an analysis of metal powder velocity and the impact energy is required to study in more detail the deposition window, namely the set of processing conditions for the CS deposition on polymers.

Stenson et al. [50] explored the effects of the process parameters of Cu deposition on HDPE. Their findings show that particle impact velocities in the region of  $258 \text{ m s}^{-1}$ , resulted in poor surface coverage as well as limited penetration depth. Larger embedding depths require higher pressures, leading to greater impact speeds and providing greater surface coverage. However, care must be taken when increasing the impact velocity, not to enter the erosion window when the impact velocity exceeds  $433 \text{ m s}^{-1}$ .

As detailed in the above sections, the polymer materials with high erosion resistance, high ductility, high toughness, and good plasticity should be more easily coated. Further to this, soft particles may interlock with the polymer substrate better than the hard particles which may cause severe erosion of the substrate.

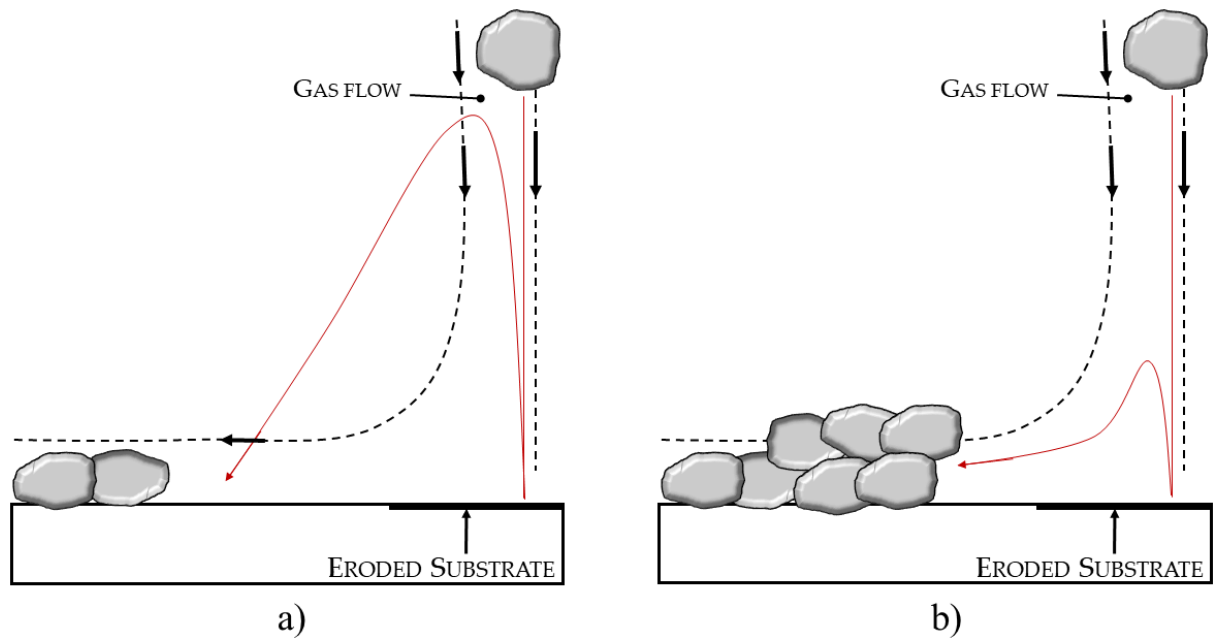


**Fig. 11** - Illustrative sketch of indirect deposition mechanisms: **a** re-deposition of rebounding powders and **b** deposition of laterally swept powders [99]

On these premises, Lupoi et al. [73] tried to predict the deposition behavior for different typologies of metallic powders cold sprayed on polymer substrates, so defining three different windows of deposition, as shown in Fig. 12.

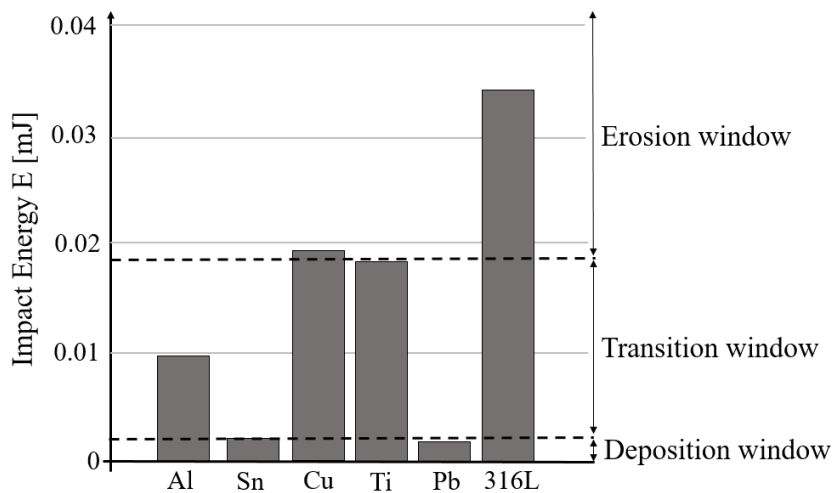


**Fig. 12** - Prediction of the deposition behavior for different typologies of metallic powders cold sprayed on polymer substrates [73]

For this case, the critical particle velocity required for adhesion within the deposition window was calculated, for each material, by supposing a given particle diameter equal to 25  $\mu\text{m}$  and using the theoretical approach provided by Schmidt [100]. The chart shown in the Figure reports the impact energy of dissimilar materials at the critical velocity. For low strength metals, such as tin, the

critical velocity is low, resulting in low impact energy transferred on the substrate that should not promote the erosion with the deposition that becomes attainable. A particle of copper has an impact energy about 10.7 times higher than tin. Therefore, erosion is more attainable with copper. In fact, strong and dense materials, such as copper and steel, are predicted to cause erosion of the substrate. Despite its high density, the lead would only produce relatively low levels of impact energy resulting in a possible deposition. On the other hand, titanium places itself on the boundary within the transition window alongside aluminum. For these cases erosion may be negligible, however, the critical velocity is high.

To establish the particle deposition window, Tsai et al. [101] developed a model to analyze the response of the polymer deformation during the impact. The scope was to define the conditions for which the particles will embed and not rebound on the surface forming a basis for subsequent adhered coatings. The numerical results have been mapped into diagrams from the responses of the particle's kinetic energy lost after impacting and further validate the experiment results of cold spraying  $\text{Al}_2\text{O}_3$  and Cu powders on a polyamide substrate. In particular, they analyzed the total energy distribution as the total amount of friction dissipation energy, internal energy (plastic dissipation energy, strain energy, and artificial energy), and kinetic energy.

#### *1.2.4 Interlayer concept for bonding*

Taking into account all the difficulties related to the cold spray deposition of the first layer, with the particle velocity that must exceed the critical velocity of the metal powder, but cannot exceed the limit above which the first layer will be eroded, some authors proposed a helpful technological solution based on the interlayer concept [64]. The key idea is to deposit a layer of soft metal powders, such as tin, to be used as an interlayer for the deposition of harder powder, such as copper, to promote the coating formation and grow-up.

Because of its low critical velocity and softness, tin is typically used as a coupling material for the interlayer. As shown by Zhang et al. [75] the possibility of depositing a coating was attributed to the low melting temperature point of tin.

Małachowska et al. [51] achieved deposition of aluminium particles on polycarbonate substrate by using a tin interlayer. As shown in Fig. 13, the aluminium particles penetrated the tin interlayer creating a well-mixed first layer of Al and Sn mixture. They proved that the use of the interlayer significantly improved the properties of the coatings, which enabled achieving a bonding strength at the level of about 3 MPa. Moreover, Małachowska et al. [58] also used the interlayer solution made of a mixture of Sn and  $\text{Al}_2\text{O}_3$  particles for the metallization of polyamide 6 polymer through dendritic copper powders.

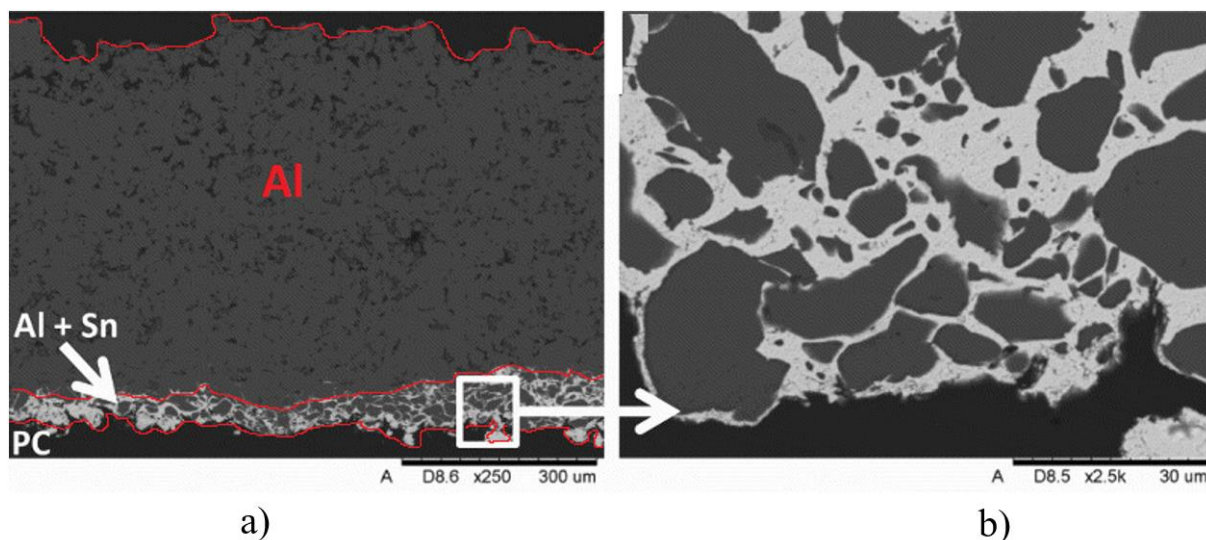


**Fig. 13** - Micrographs of cold sprayed aluminium coating on **a** tin interlayer and **b** enlargement of the selected area [51]

The relevance of the interlayer solution has been also observed by Ganesan et al. [68] who managed to deposit a Cu coating on a PVC substrate using a tin powder interlayer. Due to the soft nature of tin particles, the sprayed powders did not damage the substrate surface but deformed and covered the polymer surface. Subsequently, Cu powders impact on the interlayer and metal-metal bonding is obtained to facilitate the build-up of the coating.

### 1.3 Process Parameters

#### 1.3.1 Feedstock powder

The effectiveness of the cold spray deposition does not depend only on the substrate typology but also on the powder materials.

Owing to the differences in properties like density and hardness of the particle/substrate materials, the particles penetrate the substrate that is softer and less dense, which results in the dissipation of the kinetic energy of impinging particles [102]. Light materials (such as aluminium), characterized by both low density and high deposition velocity, can generate negligible erosion levels on the substrate as the impact energy is relatively low [73].

In some cases, it has been observed that adding a secondary component to the feedstock powder improves the deposition. Che et al. [53] deposited successfully mixed powders made of Sn-Zn and Sn-Cu at different weight percentage compositions, onto CFRP under various conditions. It was found that the addition of a second metal powder can enhance the deposition efficiency of the entire mix, even though one of the powders used for the mix cannot be successfully deposited on the substrate. The DE for all mixed powders in this work is higher than the predictions and a

potential cause of this improvement is the tamping effect of the Cu particle: when a Cu particle impacts on tin or another Cu particle, it tends to bounce away due to insufficient kinetic energy; whereas if a tin particle impacts on tin or an anchored Cu particle, deposition of the tin particle can be achieved.

Similar observations were made by Liberati et al. [99] who deposited mixed Sn-Al powders onto CFRP and found out that the addition of aluminium led to better DE than with pure tin at a higher temperature. Perna et al. [41] studied the manufacturing of coatings of Al-Al<sub>2</sub>O<sub>3</sub> on substrates with thermoplastic PLA matrix and hemp fibers. The authors found that the introduction of alumina in the mixture leads to an improvement in the surface properties of the components in terms of wear behavior, in particular up to 60% when the concentration of Al<sub>2</sub>O<sub>3</sub> does not exceed the 15%. A further increase of alumina weight percentage up to 45% was proved to cause deterioration of the surface. Liberati et al. [94] proved that when adding a second component to tin powder, the DE of pure tin on epoxy-CFRP substrate increases: in particular, the highest improvement is obtained when adding Al5083 (an increase of DE from 14 to 27%). Bortolussi et al. [103] studied the cold spray deposition of copper powder added with PEEK particles on CFRP substrates. The addition of polymer powders, in this case, is believed to act as a binder for the Cu powders, resulting in a successful deposition.

It is obvious that the deformation experienced by the particle at impact depends on the powder material; however, several studies also prove that the particle shape and size can have a key role in the deposition. Małachowska et al. [58] found out that the probability of the formation of copper coatings on the polymer is related to powder morphology. Dendritic powders have an irregular shape and therefore many different points of contact with the substrate surface. In that way, the presence of these different contact points can limit the erosion and enable the deposition of copper particles. On the other hand, the irregular surfaces can reduce the bonding between metallic powders and favor the presence of porosity. Ganesan et al. [64], summarized the previous consideration in the scheme presented in Fig. 14.

The dendritic particles have an irregular surface and different points of contact that can make the particles easily attached to the substrate. However, the deposited particles do not endure the impact of the subsequent incoming particle due to the weak bonding between the polymeric substrate and the dendritic particles. Therefore, the bonding between two different layers of particles and the consequent coating build-up are difficult to attain. Also, it was reported elsewhere [93] that Cu particles with non-spherical morphologies were shown to greatly increase the DE of tin up to 44%. Given that powders with irregular morphologies are known to travel at faster velocities [104],

these would have increased kinetic energy and could, as a result, have increased potential for powder embedment into the substrate.

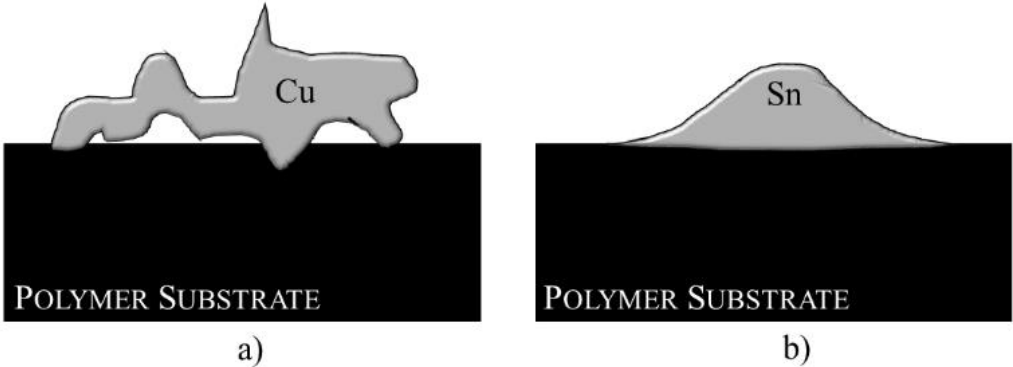


**Fig. 14** - Schematic representation of cold sprayed particle interaction with polymer substrate: **a** dendritic copper and **b** tin [64].

Gillet et al. [42] analyzed the influence of different copper powder size distribution (fine (F), medium (M) and large (L)), to avoid substrate damage, erosion and coating delamination. Using fine powder for the first layer led to a homogeneous copper coating, with around 120  $\mu\text{m}$  thickness and a  $DE > 28\%$ . The use of medium and large powder led to isolated particles or small aggregates impinged at the surface of CFRP, with  $DE$  lower than 2%. Such observations suggested that medium/large particles induce too much energy to the substrate during impact which can degrade the coating properties. Also, the same authors tried different combinations of mixed powder for the build-up. M/M, L/M, M/L, and L/L combinations were not suitable for the deposition because of the elevated level of erosion; these experimental outcomes suggest that M and L powders have too much kinetic energy and, therefore, the particle velocity is higher than the erosion limit. As an example, M/F/M and L/F/L combinations are shown in Fig. 15.

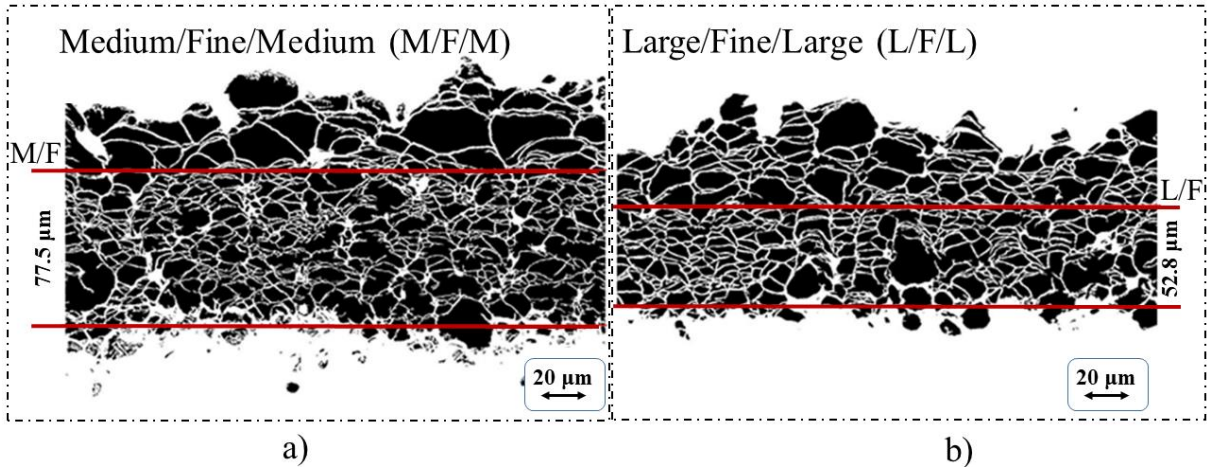


**Fig. 15** - Post-treated pictures of **a** mix of M/F/M Cu and **b** mix of L/F/L Cu [42]

Starting from the bottom of the coatings, some big particles can be spotted at the interface, the second layer coating of fine particles can then be identified. This layer densifies the former by including small particles in the gaps left by the larger particles, with a consequent increase of the coating thickness, while the third layer composed of M or L can be observed at the top. This deposition strategy led to an internal porosity of the coating under 0.5%.

### *1.3.2 Gas pressure*

The influence of the gas pressure on the coating deposition mechanisms for polymers was widely studied by Lupoi et al. [73]. The authors analyzed the effect of the powder impact speed on the deposition characteristics of glass-fiber composite materials at different inlet gas pressure in the range 5-30 bar. It was found that at a gas pressure of 30 bar, less powders were deposited onto substrate in respect to the lower pressure case, proving that at lower gas pressure the deposition is more successful. This result can be observed and justified by the optical images of the copper coatings shown in Fig. 16. At small inlet pressure, namely, when low energy impacts occur, the first layer of particles embeds below the surface, as shown in Fig. 16a. Incoming particles impacting on top of this first layer do not adhere and recoil off the surface as they do not have sufficient energy to adhere to the lower metal layer due to their insufficient speed. In this case, the impact energy is sufficient to penetrate the polymer surface only, but not to form a coating. Such behavior suggests that once the first sprayed layer is deposited, the deposition mechanism on subsequent layers is like the one observed for metallic substrates. In fact, the interaction between the metallic particles and the polymer substrate can only occur on the first layer of the coating. When increasing the nozzle inlet pressure (i.e. the particle speed) in order to form a solid coating, heavy erosion of the substrate occurs, as shown in Fig. 16b. In this case, although the particle speed is optimal for the copper to create a metal coating, the impact energy, and related impact stresses transmitted from the particle to the substrate go beyond the material strength, hence, dense erosion takes place; the impacts of the particles damaged the coating zone and broken fibers are visible in the Figure.

Giraud et al. [70] stated that by increasing the carrier gas pressure the particle penetration into the polymer increases. Anyway, at higher pressure, the deformation of the particle does still not occur while the substrate could be easily deformed or even cracked.

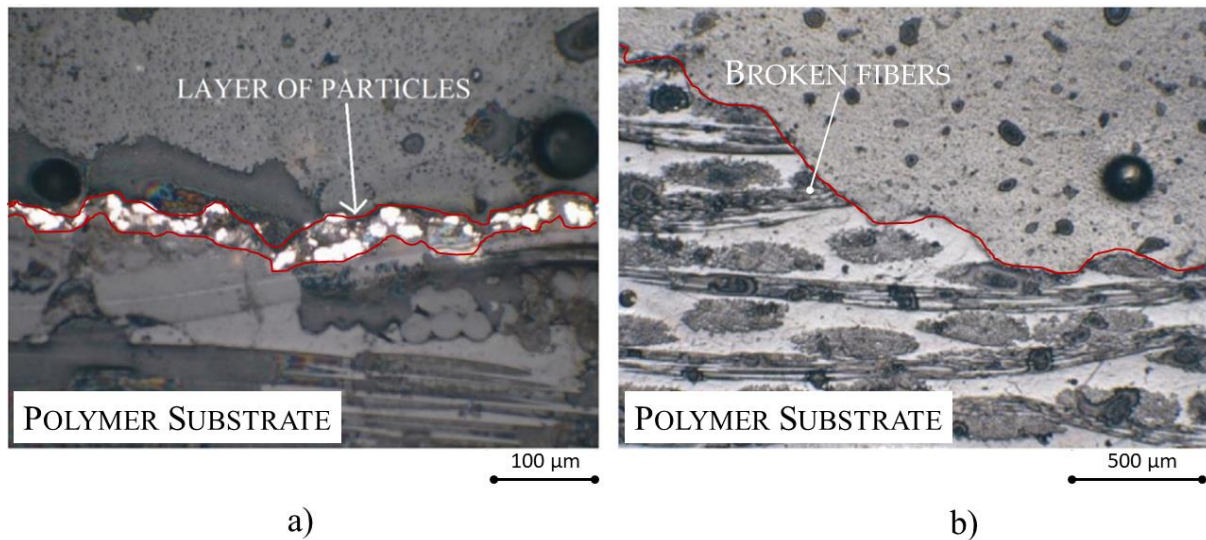


**Fig. 16** - Optical micrographs of the cross-section for copper coating: **a** low speed 5 bar and **b** high speed 30 bar nozzle inlet pressure onto glass-fiber reinforced composite [73]

### 1.3.3 Gas temperature

It is known from the literature that the gas temperature has a prominent influence on particle velocity, as proved by Ganesan et al. [64]. Moreover, the relatively hot gas impinging on the substrate also was proved to affect the bonding phenomena: at higher temperatures, the thermal softening of the substrate increased the numbers of embedded particles.

As shown in Fig. 17, the DE of the various powders on the thermoplastic (PVC) and thermosetting (epoxy) polymer substrates was measured concerning the gas pressure and temperature. The DE gradually increases in the initial stage, literally up to 473 K, and then drops sharply after 473 K. It is worth noting that the substrates soften at higher gas temperature until the glass transition temperature depending on the substrate material. In fact, this behavior has not been observed on the epoxy substrate, where the DE increases gradually up to 673 K.

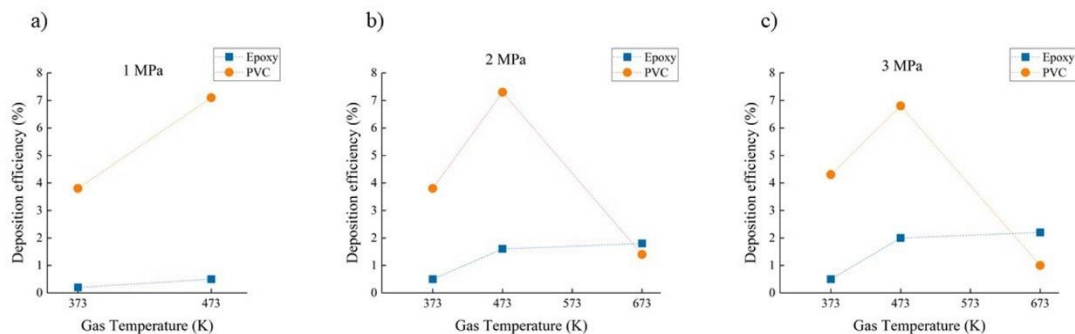


**Fig. 17** - Deposition efficiency of various powders with respect to process gas temperature and pressure: **a** 1 MPa, **b** 2 MPa, **c** 3 MPa [64]

As seen by Che et al. [43], the influence of the gas temperature is more consistent when analyzing the deposition of a single particle. In Fig. 18, a single particle of Cu is cold sprayed on PEEK at 350 °C and 425 °C.

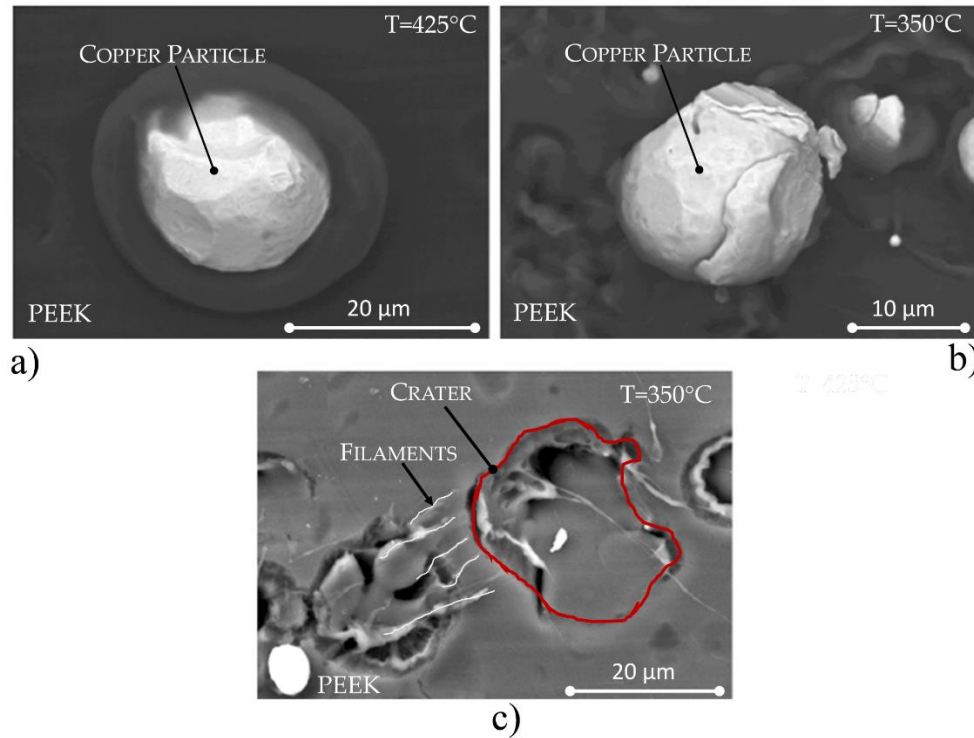


**Fig. 18** - SEM images showing copper particles cold sprayed onto PEEK at **a** 425 °C and **b** 350 °C, and **c** the craters at the PEEK surface at 350 °C [43]

At the highest temperature, the copper particle is well anchored to the substrate and an interaction zone between the particle and the substrate is clearly observed. On the other hand, at the lowest temperature of 350 °C, only a few particles remained adhered to the substrate resulting in low anchorage, and a lot of impact craters are left on the substrate (Fig. 17). The authors have also observed an interesting phenomenon, called ‘Spinnbarkeit’, characterized by the presence of a fused and rapidly cooled filament of the polymer substrate. This suggests that some localized substrate melting and bonding have been achieved at the impact sites with the bonding that was proved to be inadequate to hold the particles.

#### *1.3.4 The surface morphology and the fiber influence*

It is known from the literature that the morphology of the substrate [105] plays a leading role in the cold spray deposition process for metals [106, 107] These considerations were proved to be valid also for polymer-based substrates.

First sprayed particles impinging onto the substrate can bounce off, leaving impact craters onto the substrate and changing its morphology [71]. Only after a given delay, discussed in Papyrin [108] work, the coating can start to build-up. The main result from these phenomena is that the substrate cavities may promote the adhesion of the particles to the substrate. Based on these experimental observations, Kromer et al. [57] proposed to treat the surface of a PEEK substrate with laser surface texturing, to increase the adhesion strength and the deposition efficiency of the coating.

As shown in Fig. 19, the creation of cavities, which are characteristics of the textured surface, permitted to limit bounce due to a larger in-contact area, and the adhesion test revealed a small adhesion enhancement from  $18\pm 2$  to  $23\pm 2$  MPa. That means the textured surface increased the window of deposition, but it was limited by erosion.

Similar results were found by the study carried out by Che et al. [59] on the metallization of carbon fiber reinforced polymers by cold spray. The authors furtherly proved that the cavities produced by the rebounding of the particles can produce erosion if the cold spray process parameters are not properly set.

Although the substrate morphology affects the deposition behavior of the cold sprayed powder, it is evident that the fibers within the polymer to form composite materials, like CFRP, change the morphology of the polymer surface that can affect the deposition [109]. Moreover, if the fibers are exposed to the impacted surface, erosion, and disruption of them can be observed resulting in a poor coating with the substrate tending to deteriorate.

For the cold spraying of aluminum and copper powders at high gas pressures [75], no successful coatings were obtained with all the presented conditions; erosion was found to be the key problem for developing a continuous coating. This is also confirmed by the experimental results carried out by the same authors [59]; it was found that deep cavities form in the CFRP substrate at the impact spots suggesting that erosion takes place and the particles are not firmly interlocked with the substrate. Generally, two distinct areas the authors observed in the impacted sample, one area with the surface epoxy removed and the carbon fibers exposed as a result, and the other area with some surface epoxy left. Within the exposed carbon fiber area, fracture of the carbon occurs, and no particles can be found on or among the exposed carbon fibers. Better results were found for tin particles. In contrast to aluminum and copper, tin could be deposited onto the exposed carbon fibers, and tin clusters can be found, as shown in Fig. 20. Furthermore, no spherical particles can be observed in the cluster, indicating that the particles underwent permanent deformation during the impact and the building-up.

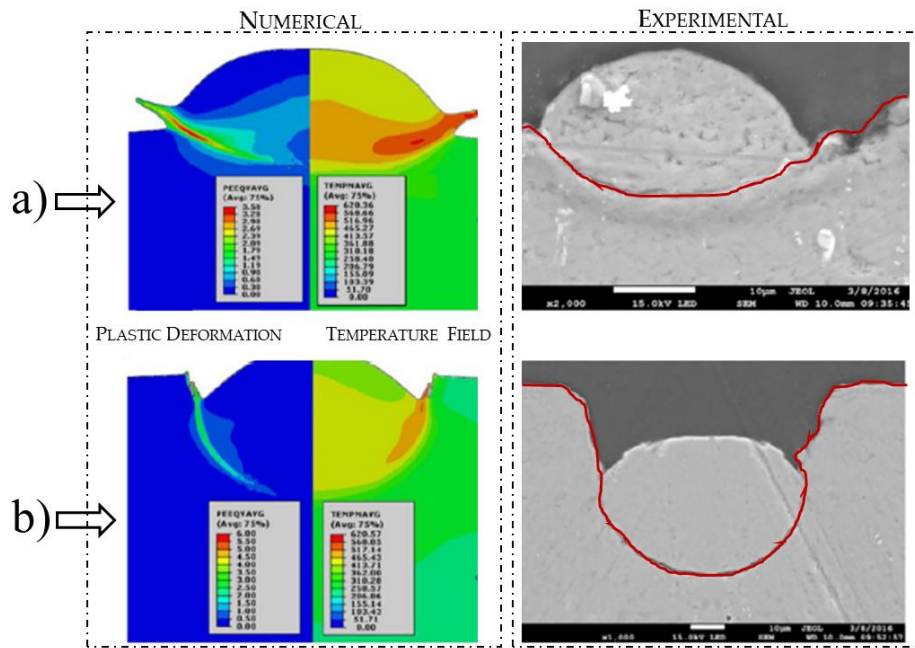


**Fig. 19** - Numerical and experimental observations of a single particle impact on planar **a** and textured **b** PEEK surface [57]

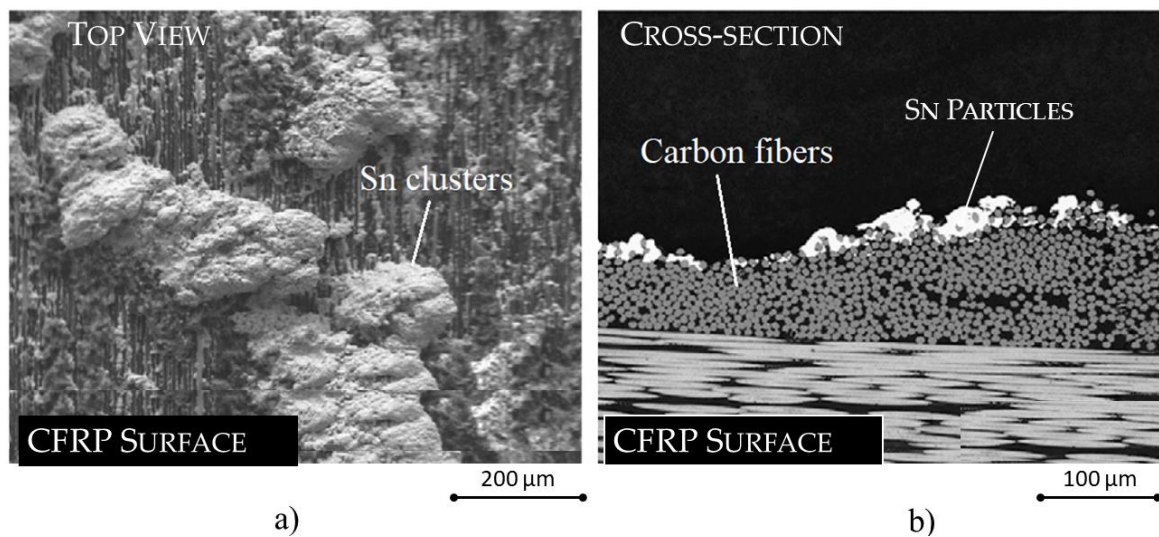


**Fig. 20** - **a** Top and **b** cross-section micrographs of the CFRP samples after cold spray of Sn powder

To avoid the fiber disruption, Bortolussi et al. [103] proposed an innovative solution involving the addition of PEEK particles to Cu powder. The polymer powder act as a binder for the Cu powders: PEEK particles impact the surface and adhere to the fibers, while copper particles rebound; once a few amounts of PEEK adhere to the surface, Cu particle impact on deposited PEEK and embed to the substrate.

When spraying on FRPs, the erosion of the fibers is one of the key issues and, for this reason, several authors stated that a superficial matrix layer is needed to facilitate the build-up of the metal coating. Moreover, if the substrate is thick enough, only the upper part of the substrate contributes to the cold spray deposition [72].

For this purpose, Gillet et al. [42] analyzed the influence of a single and a double PEEK layer on the FRP surface. They proved that the coating characteristics were similar for both composites, but single PEEK samples showed an irregular coating-substrate interface that rooted to a higher peeling effect, compared to double PEEK samples. Accordingly, under a certain value of substrate thickness, the samples exhibited a not homogeneous and well compacted coating-substrate interface. That behavior can be addressed to a lower contribution of the elastic modulus and elastoplastic behavior when spraying on a single PEEK substrate, which is the opposite when spraying on a double PEEK substrate. In this last case, higher resistance to the incoming particles of the subsequent layers is expected.

## **1.4 Properties of the coatings**

### *1.4.1 Microhardness*

Zhou et al. [72] analyzed the properties of Al and mixed Al/Cu coatings. They measure the microhardness of the coatings of pure aluminum. It was found that the Al and Cu coatings retain microstructures like those of the feedstock powders, without any generation of oxides. They found out that the microhardness of the pure Al coating is about 42 HV0.1. For the Al/Cu mix, the microhardness of the pure Al bottom layer reaches 52 HV0.1, and the microhardness of the pure Cu layer of the bimetallic coating is about 140 HV0.1. In the second case, the higher value of microhardness of the Al layer is attributed to the compacting effect caused by the successive impacts of Cu particles. The Al and Cu layers are dense and uniform, and the porosity of the Al layer is reduced to 1.1% due to the bombarding by the Cu particles. These results coincide with those obtained by Małachowska et al. [51]: the hardness of aluminum coatings on a sandblasted substrate reached on average 46.8 HV0.1, and the hardness value on a tin interlayer was slightly less than and equal to 36.5 HV0.1. This confirms the low deformation of aluminum particles caused by the soft substrate and the insufficient particle velocity.

Further studies analyzed in more detail the relation between microhardness of copper coatings and powder deformation or process parameters. In these works [49, 58], deposited copper coatings reached low microhardness values due to a low deformation grade of feedstock material. In this other work [49] the authors analyzed the influence of the propelling gas pressure; when the gas

pressure increases, the microhardness increases due to the stronger peening effect of the subsequent impact of successive particles that lead to a more evident work-hardening effect.

Rokni et al. [40] were able to measure the microhardness on the first layer of sprayed powder and the coating after multiple passes. They found out that the first layer showed microhardness of  $1.26 \pm 0.18$  GPa, approximately the hardness of 7075 Al powder [110] while the metal layers subsequently deposited showed higher hardness values (1.5-1.8 GPa). The hardness of the bonding layer is indicative of a low degree of plastic deformation (work hardening) in this region and indicates the absence of peening [111, 112], attributed to more particle deformation resulting from metal/metal particle interactions in the build-up layers of the deposit.

#### *1.4.2 Electrical conductivity*

Electrical conductivity is a commonly used parameter to analyze the effectiveness of substrate metallization. It correlates with the cohesive strength of the coating and can be used to evaluate the coating quality, representing the fraction of a well-bonded interface [113]. Normally, the electrical conductivity mainly is believed to depend on the internal defects inside the coating [114]. Che et al. [49] found out that the electrical conductivity values of the cold sprayed Cu coating on PEEK substrate are 35.9% - 55.4% of the bulk copper. It can be detected that the electrical conductivity of the Cu coating increases as the propelling gas pressure increases. The same occurs for the coating microhardness. This increase of electrical conductivity when increasing propelling gas pressure can be attributed to better particle bonding between Cu particles and to lower presence of internal defects like pore and micro-cracks. When increasing the propelling gas pressure, the deposited particle experienced more plastic deformation. At the same time, the higher gas pressure brought an enhanced peening effect of the successive particle impact with higher impact velocity, which can restrict the porosity and interparticle boundaries. As a result, the increased propelling gas pressure leads to the higher electrical conductivity of the Cu coating on the PEEK surface, which can effectively broaden its application in industrial fields.

The electrical conductivity measurements performed on various Sn-Cu coatings [115] proved that the cold sprayed tin coating is approximately 49% as conductive as bulk tin, indicating the bonding in the cold sprayed state is not as conductive as the “100%” metallic bonding in the bulk material. Moreover, even though copper is several times more conductive than tin, the Sn-Cu coatings exhibit a comparable conductivity to the cold sprayed tin coating and, in some cases, a much lower conductivity (Fig. 21). In general, the addition of copper, that is more conductive than tin, did not increase the overall conductivity but led to a decrease instead; the decrease may be caused by the porosity and the increasing number of Cu/Sn interfaces in the coating, which may behave as the

barriers for electrons. Similar to the as-sprayed state, the addition of the more conductive copper did not improve the overall conductivity of the mixture coating, indicating the Cu-Sn boundaries are not beneficial to electron flux.

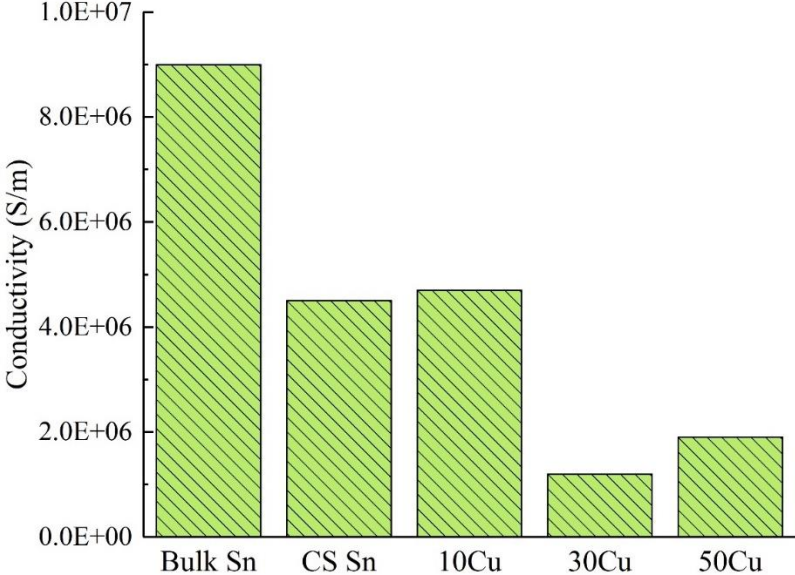


**Fig. 21** - Electrical conductivity measurements for various coatings cold sprayed at 300°C, 60 psi [53]

As for the electrical property of the coatings [72], it was proved that the volume resistivity of the coatings, which is responsible for CFRP damage and degradation, increases with the growth of the gas temperature (Fig. 22).

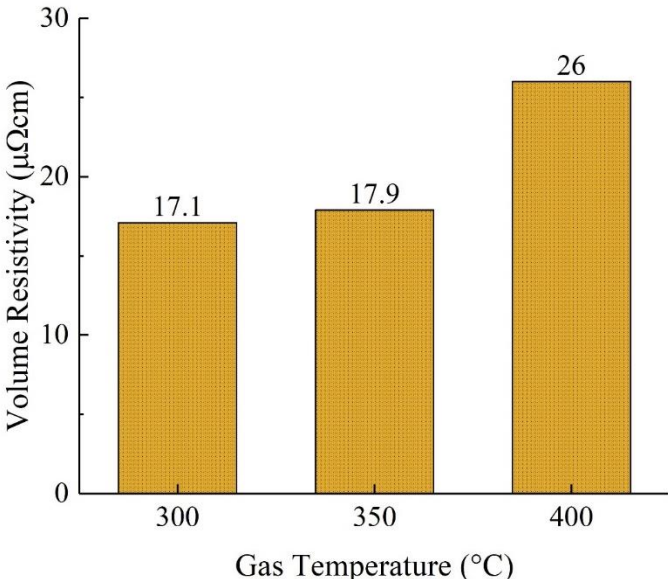


**Fig. 22** - Volume resistivity of aluminum cold sprayed onto CFRP [72]

### 1.4.3 Adhesion

Adhesion tests are commonly used to determine the strength of bonding to the composite substrates. A wide analysis of coating adhesion was made by Rokni et al. [40]. They analyzed the deposition of Al7075 and pure Al on different substrates, as seen in Fig. 23. In all the cases, failure occurred at the deposit/substrate interface. Comparing Fig. 23a and 23b, Al deposits showed generally lower adhesion properties than 7075 Al deposits. These values are in the same range reported previously for metallic coatings/polymeric substrates [68, 73, 75] but higher in the case of 7075 Al. The difference noted for pure Al and 7075 Al is attributed to two different causes: the hardness differences between the Al powder particles and the polymer substrates, and residual stresses in the deposits. The relatively soft pure Al particles do not penetrate the polymeric substrates as deeply as the harder 7075 Al particles. Additionally, it must be considered that the residual stress mainly depends on the coating thickness [116]. Considering the substrate polymer, it is evident from Fig. 23 that PEEK and PEI substrates yield much greater adhesive strength values than the ABS substrate. The lower yield strength and  $T_g$  of ABS [117] caused these combinations to yield the lowest adhesive strengths.

In general, in most works, the adhesion of the substrate is lower, reaching a maximum of 10 MPa. In Zhou et al. [72] the mean bonding strength of coatings is evaluated in 2.26 MPa. In Małachowska et al. [58] work, the bonding strength of copper coatings amounted to  $3.6 \pm 0.2$  MPa. It has been also proved in this work [51] that the use of an interlayer can increase the bonding strength.

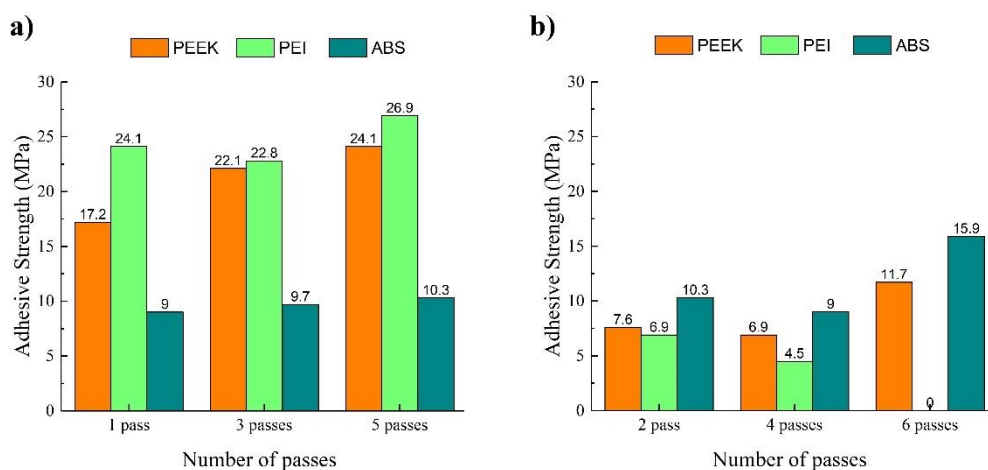


**Fig. 23** - Coating thickness of **a** 7075 Al with 1, 3, and 5 passes, and **b** pure Al with 2, 4, and 6 passes

[40]

Higher values were obtained by Che et al. [59]. The tin coating cold sprayed at 300 °C and 4.1 bar had the strongest adhesion to the CFRP substrate, which averaged 7.6 MPa. Anyhow, when the gas pressure was increased to 5.5 bar, the adhesion strength decreased to below 3 MPa, indicating the higher kinetic energy deteriorated the coating/substrate interlocking/interface. In fact, as proved by Gillet et al. [42], lower deformation of the powder and the inhomogeneity of the coating correspond to lower adhesion. Accordingly, higher deformation of the powders and homogeneity of the coating at lower pressure can guarantee a better adhesion of the first sprayed layer. This is in contrast to the conventional observation that the adhesion strength basically increases with increasing particle velocity when cold spraying metals on the metal substrates [118]. In general, the adhesion strength of the tin coatings to the CFRP substrates was low, especially when compared with the conventional metal/metal adhesion when cold spraying onto metal substrates. These observations may indicate that the bonding between tin particles and CFRP substrate is entirely mechanical

## **CHAPTER 2 – Experimental campaign: manufacturing of substrates and cold spray deposition**

### **2.1 Deposition of metallic coating on thermoplastic- matrix composite substrates**

#### *2.1.1 Manufacturing of GFRP Composites*

Polypropylene (PP) was chosen as a thermoplastic matrix while bidirectional glass fiber fabric of 160 g/mm<sup>2</sup> was taken as reinforcement. To control the laminate dimension, sheets in polypropylene (PP) and glass fibers fabric were cut in a rectangular shape of 150mm x 100mm. Composite laminates were realized with a compression molding technique. For each laminate, 15 different sheets were used, alternating fibers and matrix sheets. Then, the whole composite has been placed in an oven and heated at 210°C for 15 minutes. To limit the damage of the fibers, a polymer layer has to be placed on the top of the substrate.[42] The layer thickness of the superficial matrix layers is considered a process parameter. The building strategy of the FRP to obtain protective polymer layers of different thicknesses for the fibers on the top of the substrate is investigated. As shown in Fig. 24 two different types of laminates have been produced by superimposing matrix and fiber layers in different ways: in the first case, a single matrix layer is placed on the top of the panels while in the second case two matrix layers are used. The actual matrix layer thickness was calculated as the mean value of five different measures performed in 5 different points of the panel, and the results are summarized in Table 2.

**Table 2** - Mean value of the thickness of the superficial layer for the two typologies of GFRP.

Panel typology	ID Panel	Mean substrate layer thickness "t" [ $\mu\text{m}$ ]
Single configuration	GFRP-1	149
Double configuration	GFRP-2	254

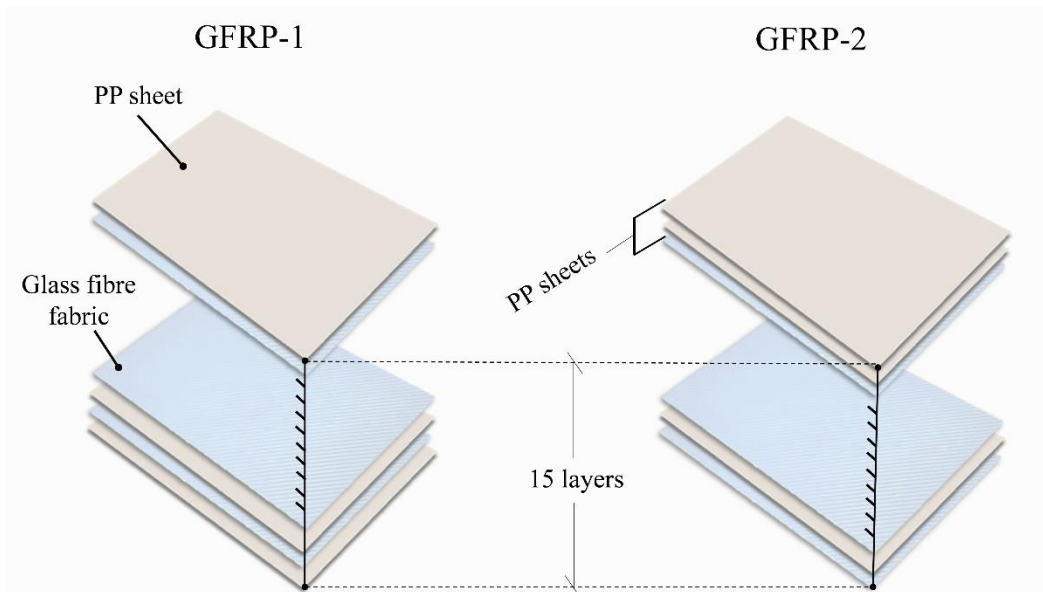


**Fig. 24** - Exemplificative sketch of laminate build-up in two different configurations.

### 2.1.2 Cold Spray deposition

For the deposition, two different feedstock materials were chosen. Gas-atomized AlSi10Mg and Steel 316L powders by LPW South Europe were chosen with a size dimension from 15  $\mu\text{m}$  to 45  $\mu\text{m}$  and are reported in Fig25.

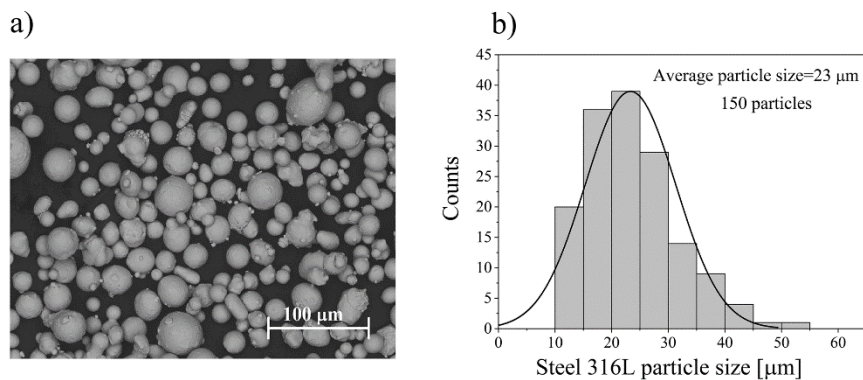


**Fig. 25** - SEM acquisition and particle size distribution of AlSi10Mg a) b) and Steel 316L c) d) powders

**Table 3 - GFRP sample with different parameters combination**

Substrate	Powder	Gas Type	Gas P	SOD	Sample Number
			[bar]	[mm]	
GF-PP1	AlSi10Mg	Air	0,5	20	1
				25	2
				35	3
		0,6	20	4	
			25	5	
			35	6	
	Nitrogen	0,5	20	25	7
				25	8
				35	9
		0,6	20	25	10
				25	11
				35	12
	Steel 316L	Nitrogen	0,5	20	13
				25	14
				35	15
		0,6	20	25	16
				25	17
				35	18
GF-PP2	AlSi10Mg	Air	0,5	20	19
				25	20
				35	21
		0,6	20	25	22
				25	23
				35	24
	Nitrogen	0,5	20	25	25
				25	26
				35	27
		0,6	20	25	28
				25	29
				35	30
	Steel 316L	Nitrogen	0,5	20	31
				25	32
				35	33
		0,6	20	25	34
				25	35
				35	36

The deposition was accomplished with a low-pressure cold spray machine Dymet 423 and air and nitrogen were used as the carrier gas. The process was automated by a numerically controlled pantograph while the nozzle moved at a set speed and a set standoff distance when spraying onto the substrate. The panel was placed on a platform while the working gun was placed vertically above the substrate at a fixed standoff distance. To analyze the interaction between the cold sprayed powder and the polymer and study the bonding mechanism, only one spray layer is deposited on the panel.[119] For each set of process parameters, a single track of about 100 mm length has been deposited. The inlet gas temperature was set at 150 °C and maintained constant at the set temperature. Different propellant gas pressures (0.5 MPa, 0.6 MPa) and different standoff distances (20 mm, 25 mm, 35 mm) were used to investigate their influence on the deposition. The substrate temperature was about 110 °C, below the PP melting temperature, and it was measured with a k-type thermocouple. For the experimental campaign, 36 different coatings were produced and characterized by different spraying conditions by varying the SoD distance and the gas inlet pressure. Table 3 summarizes all the obtained samples with different parameter combinations.

### *2.1.3 Coating Characterization*

The experiments aim to evaluate the surface coverage of the coating, the powder morphology and the penetration depth of the particles. After the deposition, each sample was cut perpendicularly to the sprayed surface with a hacksaw to obtain a small specimen of about 1 cm width. As pictured in Fig. 26., observations of the specimens were taken in two different directions: cross-section direction, perpendicular to the cutting direction and top-view direction, parallel to the cutting direction. Firstly, top-views of the coatings were observed by a Scanning Electron Microscope (SEM - Hitachi TM 3000) and Confocal Microscope (Leica DCM3D Scan). Afterward, each sample was mounted, prepared through different grinding and polishing phases with sandpapers and diamond suspensions and then metalized. The cross-sections of the coatings were observed with the same SEM and an Optical Microscope (Askiop 40 by Zeiss). To qualify the effectiveness of the deposition, the amount of coated surface should be evaluated. The effective coated area was calculated from SEM acquisition by creating a binary mask of the surface and evaluating the pixel threshold (ImageJ), where particles are identified in white while the polymer substrate in black (Fig. 27). The percentage coverage of pixels was then quantified and the surface coverage was visually calculated as the mean value of three different acquisitions. Coating height was estimated by the analysis of both the Confocal Microscope and the Optical Microscope acquisitions, the first from the top-view direction while the second from the cross-section direction. Top-view observations were carried out through the generation of a three-dimensional surface taken from a

random area of the coated surface. After the creation of the surface, as seen in Fig.28, results have been exported to LeicaMap software for the profile extraction. Subsequently, maximum height was measured as the mean value of the 3 maximum profile values.

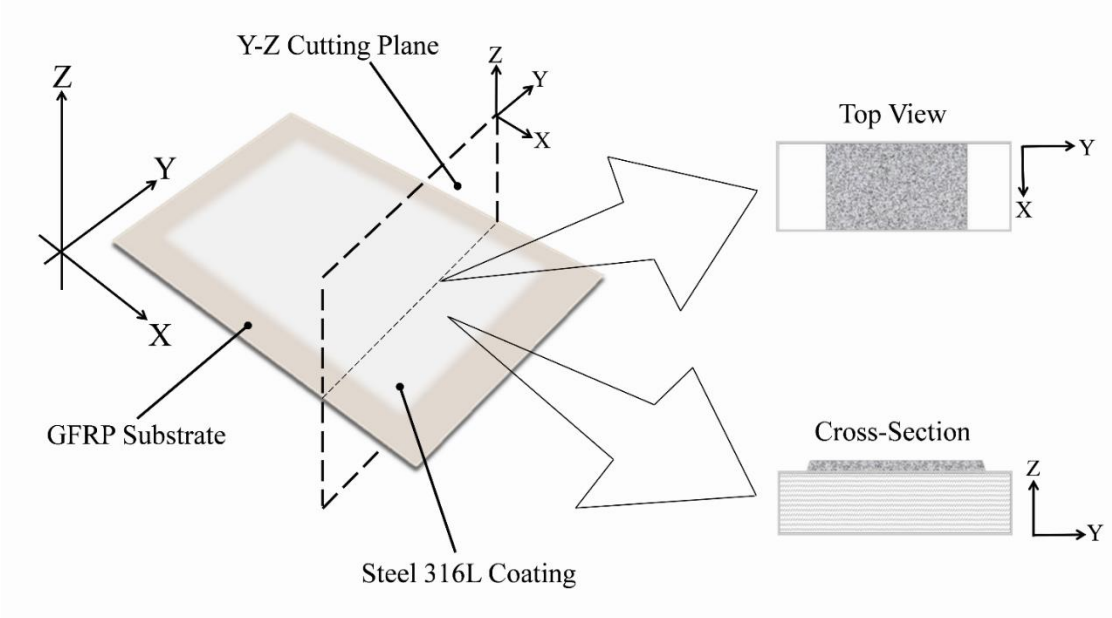


**Fig. 26** - Scheme of different direction of coating characterization.

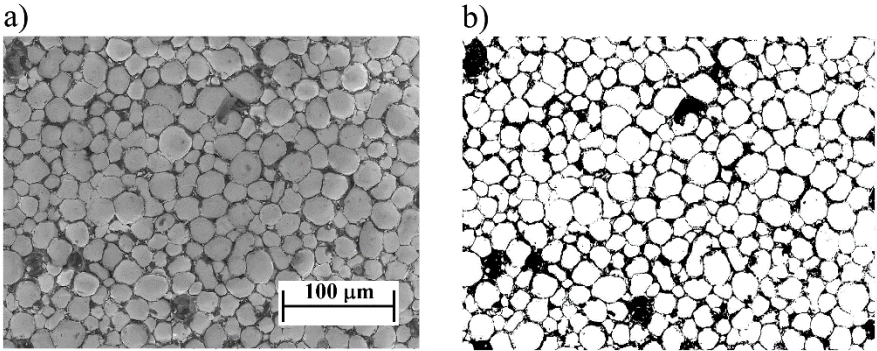


**Fig. 27** - Top view acquisition with SEM (a) and ImageJ (b).

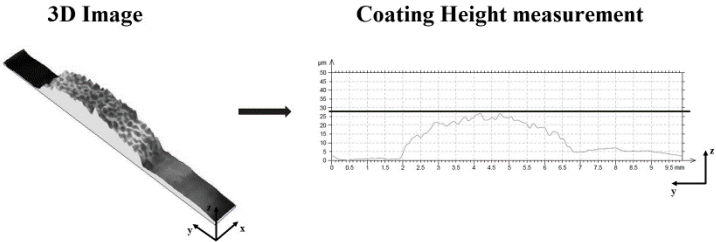


**Fig. 28**- Profile extraction with LeicaMap for maximum coating height analysis.

To compare the coating height before and after the sample preparation, further analyses with the Optical Microscope in the cross-section direction were required. The coating height values were visually measured from the substrate surface up to the highest point of the coating in three different acquisitions and then a mean value is determined. To estimate the penetration depth of the particles, coatings were examined with SEM acquisition in a cross-section direction. As done in the previous study[60, 66, 120], this length was identified from the substrate surface down to the deepest point of the coating and its value was taken as the mean of ten different measurements in several points of the coating.

## **2.2 Deposition of metallic coatings on PLA functionalized thermosetting composites**

### *2.2.1 Manufacturing of PLA functionalized thermosetting composites substrates*

Basalt fibre (BS) reinforced plastic square laminates, 400 mm inside, were manufactured through the resin vacuum infusion technology by using plain-woven basalt fabrics, 200 g/m<sup>2</sup> (Basaltex NV) and an epoxy infusion system by Gurit (Prime 20LV). 16 fabric layers 0/90 were stacked to obtain a thickness of 2.50 mm. In order to fabricate a metal coating on the BFRP substrates, a novel solution was here proposed based on PLA film treatments performed on the epoxy surface, so promoting the metal anchoring. In particular, a commercial thermoplastic PLA film with a thickness of 30 µm was positioned on the surface of each sample and a heated plate press of the Collin model P 200 E was used to favour the PLA-composite coupling.

Since the melting temperature of the polylactic acid is between 180 °C and 220 °C, the dishes were brought to a temperature of 200 °C, and then a pressure of 5 bar was applied for about 5 min.

### *2.2.2 Cold Spray deposition*

AlSi10Mg were used for the spraying process. Different coating tracks with a travel speed of the spraying gun equal to 8 mm/s were preliminary produced by varying the process parameters in a wide range (inlet gas temperature: 150–600 °C, inlet gas pressure: 4–8 bar, stand-off distance (SoD) 10–80 mm). In details, a 90×90 mm square form coating was developed on the composite substrate specimens' surface by spraying the one-single layer of aluminium particles according to the schematization reported in Fig. 29.

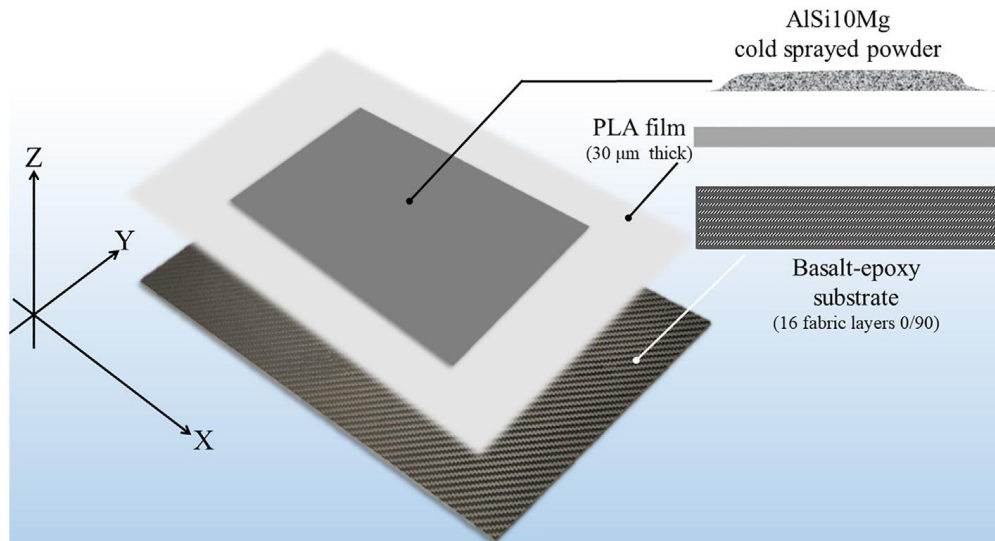


**Fig. 29** - Schematization of hybrid composite structure made of basalt-epoxy substrate, PLA film and AlSi10Mg cold sprayed powder.

### 2.2.3 Coating Characterization

After a first visual inspection, the coated samples were observed through both optical and SEM microscopy to highlight the morphology of the coating, thus to set the best CS process parameters. The range of the process parameters was selected to accelerate the particles up to the required velocity. This approach permits to obtain adhesion without inducing damages within the panel due to overheating and particle bombardment.

Low-velocity impact tests (maximum impact velocity,  $VI = 4$  m/s) were carried out by a falling weight machine, Ceast Instron Fractovis FK4 (Turin, Italy), at three different energy levels ( $U = 10$  J,  $20$  J,  $30$  J) to avoid the penetration and to measure the indentation depth.

The rectangular specimens,  $100 \times 150$  mm, cut by a diamond saw from the original panels, were supported by the clamping device suggested by the ASTM D7137 Standard and were centrally loaded by an instrumented cylindrical impactor with a hemispherical nose,  $19.8$  mm in diameter. Tests were conducted using an impactor with a mass,  $m$ , equal to  $3.640$  kg that combined with the drop heights allowed to obtain the selected impact energy.

After the impact tests on both neat and cold sprayed substrate, the specimens were observed by visual inspection to investigate the coating quality and the surface damage, whereas a confocal microscope, Leica DCM3D, was used to measure the indentation depth with a magnification of  $10\times$ . Also, the delaminated areas were inspected using a US Multi2000 Pocket  $16 \times 64$  system by M2M: examinations were performed with a linear phased array probe,  $5$  MHz,  $64$  elements.

The phased array systems could be used for all inspection types, traditionally made using conventional ultrasonic flaw detectors. The advantages of phased array technology, in comparison

to traditional ultrasonic, derive from the possibility of being able to use several elements assembled in a single transducer to guide, focus and scan the beams. The apparatus operates in the form of reflection. The probe metallized for the emission and the reception of the ultrasonic waves. During the acquisition, the pulse Echo technique was adopted: short duration ultrasound pulses are transmitted into the region to be studied, and echo signals resulting from scattering and reflection are detected and displayed as a C-scan.

To obtain reliable results from the ultrasound controls (US), it was necessary to set the apparatus carefully to take into account the absorption coefficient of the signal, different from carbon and glass fibres. In fact, due to the anisotropy and non-homogenous characteristics of the composite materials, the velocity of ultrasound waves propagation changes as the material changes. In particular, the velocity depends on the fibre and matrix type, fibre orientation, thickness and composite stacking sequence. So, the detection of the velocity is complicated for the composites, and it also depends on the operator's manual skills. In this case, using the pulse-echo technique, the depth of a reflective structure is inferred from the delay between pulse transmission and echo reception. Thanks to this technique, analysing an undamaged sample, the correct plate thickness is obtained, and the acquisition system is calibrated.

### 2.3 Deposition of metallic coatings on 3D-printed substrate

#### 2.3.1 Manufacturing of 3D-printed substrate

The 3D-printed composite materials were made through the FFF technology (Markforged X7).

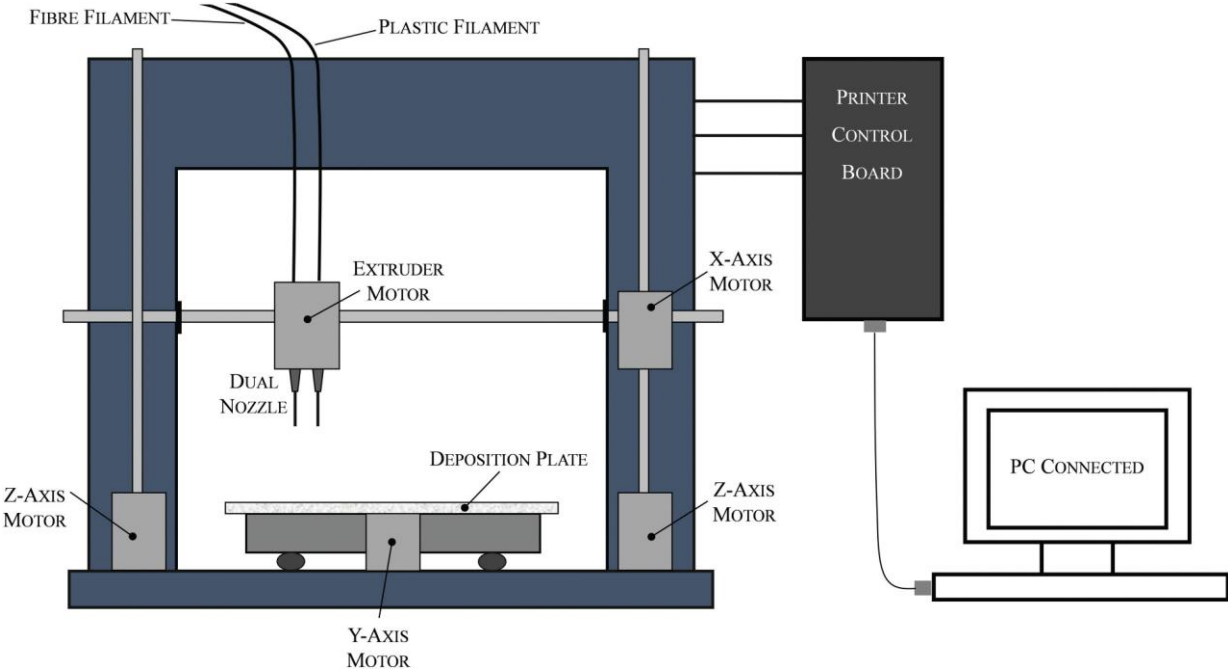


Fig. 30 - Simple sketch of FFF technology for the 3D-printed polymer-based materials.

The used matrix is Onyx, a novel nylon-based material with short carbon fibers dispersed in it. It represents a high strength thermoplastic material, with excellent surface finishing that can be molded unreinforced or reinforced with continuous fibers in order to give a resistance comparable to aluminum. The material provides greater strength and a matte black surface finish to the 3D-printed parts. Compared to traditional nylon, Onyx is about 3.5 times more resistant and has a greater hardness and a HDT (Heat Deflection Temperature) of 140° C [121]. The short carbon fibres dispersed in the nylon filament, modify the behaviour of the material on cooling, inducing lower thermal deformations so that the dimensions of the moulded pieces faithfully reproduce the model designed in CAD. By selecting printing parameters, such as deposition strategy, and the characteristics of the materials involved, the cloud-based software optimize the process in order to quickly obtain a printout of the desired part. The dual extruder system generates the composite part, layer-by-layer, according to the Continuous Fibre Fabrication (CFF) process technology. The first nozzle builds the plastic matrix and the second wrap the fibre. With a built-in laser micrometre, the printer automatically scans the processing plate with 1 µm precision to create a contour map of its surface. At this point, it calibrates its measurements with the extrusion readings to correctly set the height of the nozzle and the dynamic adjustment of the topography. In this way, the printer ensures that your printouts are precisely positioned inside the printing chamber (Fig. 30). Given the excellent surface finish obtainable, no further chemical or mechanical processing is required on the moulded parts, with a considerable saving in terms of time.

The long carbon fibre used to produce the fibre-reinforced polymers is made up of thin elemental carbon filaments. Fibres have extremely variable chemical and physical properties. The modulus of elasticity varies from about 350 kg/cm<sup>2</sup>, a value between the glass fibres and aluminium ones, up to 7000 kg/cm<sup>2</sup>, or three times greater than the modulus of steel [121].

The manufacturing of the specimens was carried out in two parts, one to identify the influence of the fiber content, the other one to identify the influence of both matrix content and building strategy.

The first part of the experimental campaign was carried in order to investigate how the fiber out by defining three macro-typologies for the samples, referred now as FO (Full Onyx), LFC (Low Fiber Content) and HFC (High Fiber Content). They are characterized by different fiber volume fractions and layup sequences; in particular:

- FO: Onyx laminates made of nylon, as a thermoplastic matrix, and chopped carbon fibers randomly dispersed in it;
- LFC: Onyx reinforced with a continuous carbon fiber deposited alternating one layer of fibers at [0]° and two layers of matrix;

- HFC: Onyx reinforced with a continuous carbon fiber filament in each layer deposited following the sequence  $[0/45/90/135]^\circ$ .

Each panel is 135 mm in length and 36 mm in width. Each layer constituting the stratified panel is about 0.125 mm with a final thickness of the samples equal to  $t = 4 \pm 0.2$  mm.

For both the reinforced configurations (referred to as LFC and HFC in this activity), the bottom, as well as the top surfaces of the panels, were made by depositing four consecutive layers of Onyx matrix. This strategy is used to avoid exposing the fibers on the outer surface and to take advantage of the higher quality surface finish and accuracy ensured by the unreinforced Onyx.

Printing is performed at  $260^\circ\text{C}$  with an estimated speed of  $6.90 \text{ cm}^3/\text{h}$  for the Onyx layers and  $2.39 \text{ cm}^3/\text{h}$  for the carbon fiber layers. For the LFC configuration, the layup sequence “matrix-matrix-reinforcement” was repeated throughout the panel’s thickness in its wholeness with a symmetric configuration; the same procedure was applied for the  $[0/45/90/135]^\circ$  layup construction. The scan pattern used for the panels’ manufacturing is reported in Fig. 32. Concerning the matrix layer, firstly the nozzle defines the boundaries of each layer (the red pattern performed in the x-y plane in Fig. 32) and then the rectangular filler for the matrix core structure. The fiber scan strategy is performed in agreement with the layup sequence defined during the design phase. For the sake of clarity, the fiber scan pattern at  $0^\circ$  only is reported in Fig. 31.

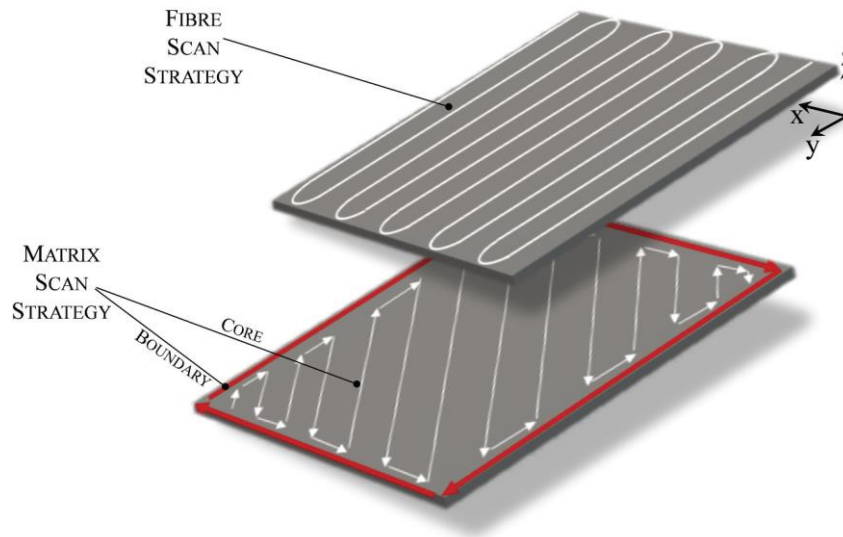


**Fig. 31** - Scan pattern for the panels’ manufacturing.

The surface finishing of each manufactured panel was observed by means of confocal Leica DCM3D Scan and optical microscopes aiming to analyze the surface characteristics and chose the most appropriate face upon which the deposition can be carried out effectively. An explanatory sketch of the panel stratification and layup is reported in Fig. 32 and data are reported in Table 4.

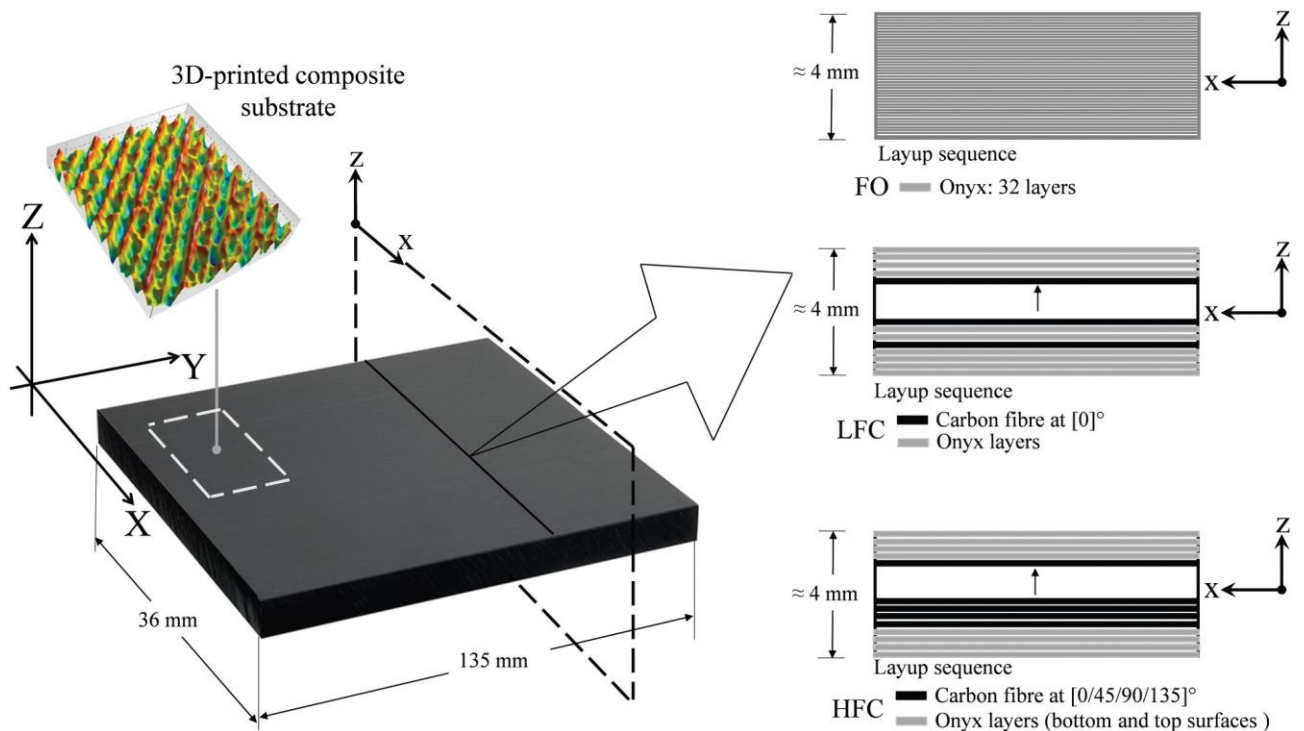


**Fig. 32** - Layup sequences and stratification of 3D-printed composite substrates. (For the clarity of the picture, the layup sequence repetition was not drawn throughout the panel thickness for reinforced laminates).

**Table 4** – 3D substrate with different reinforcement infill

	FO	LFC	HFC
Matrix Typology	Onyx	Onyx	Onyx
Long carbon fibre layers	NO	YES	YES
Printing temperature [°C]	260	260	260
Layer thickness [mm]	0.125	0.125	0.125
Panel thickness [mm]	4±0.2	4±0.2	4±0.2
Layup sequence	[Onyx sym <sup>16</sup> ]	[Onyx <sub>4</sub> /0°/Onyx <sub>2</sub> /0°/Onyx <sub>2</sub> /0°/Onyx <sub>2</sub> /0°/Onyx <sub>2</sub> ] sym	[Onyx <sub>4</sub> /(0°/45°/90°/135°) <sub>3</sub> ] sym
Number of layers	32	32	32

In the second part of the experimental campaign Pure Onyx panels as well as reinforced laminates were manufactured in this activity and are referred below as *3D-O* and *3D-F*, respectively the substrates were manufactured by varying the building parameters, in particular the matrix filling ratio. The infill pattern chosen for the Onyx matrix is triangular in the core and three different percentages filling values (30%, 40% and 50%) were considered for all the samples, as shown in

Fig. 33, schematically; meanwhile, the outermost surfaces of the panels were printed with one, two or three layers of 100% fill Onyx filament (the so-called infill solid strategy at 45° [122]) to take the advantages of the resulting higher surface finishing (the details in Fig. 33). A 0/90 symmetric configuration was set for the reinforced samples which were produced alternating one layer of matrix and one layer of fibres, following the lay-up sequences shown in Fig. 34.

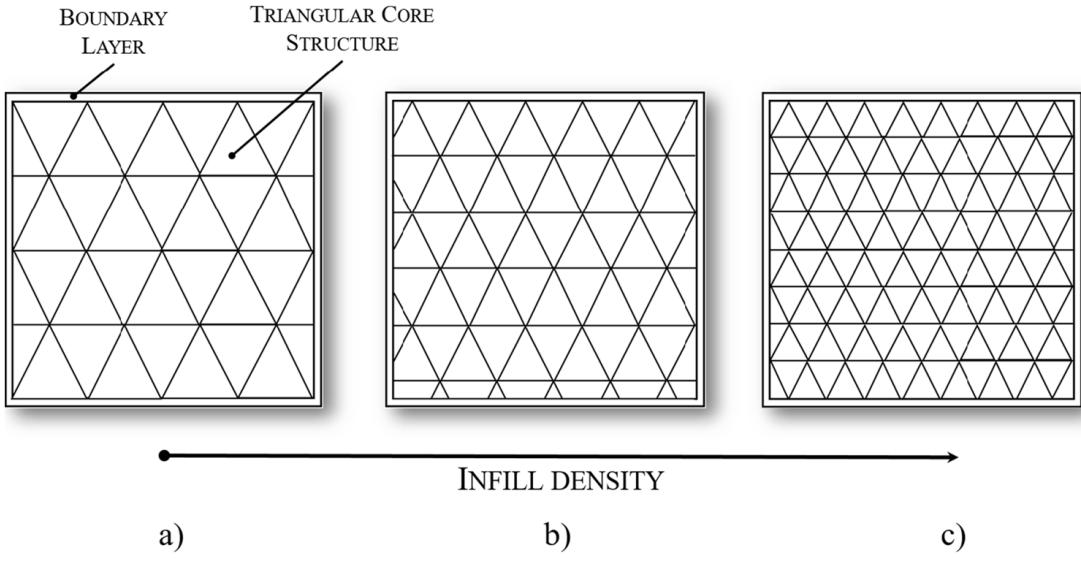


**Fig. 33** - Illustrative sketch of Onyx-based matrix printing strategy by varying the infill density: a) 30%, b) 40%, c) 50%

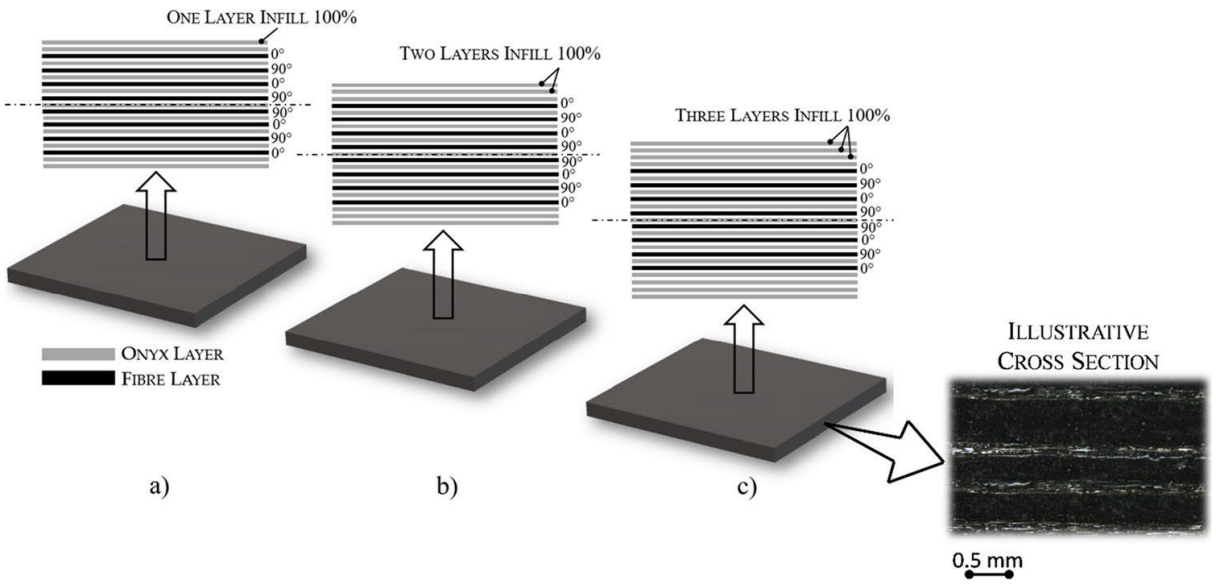


**Fig. 34** - Simple scheme of a 0/90 symmetric configuration of reinforced samples. The figure highlights the superficial matrix thickness of the outermost surfaces: a) one layer, b) two layers; c) three layers

Concerning the matrix layer, firstly the nozzle defines the boundaries of each layer and then the triangular pattern for the matrix core structure. As summarized in Table 5, 18 different samples were 3D-printed. The table also reports the main geometric characteristics of each specimen. The

square-shaped panels ( $80 \times 80$  mm) have a thickness in the range 2.0–2.5 mm depending on the number of layers used for the outermost surfaces. Each layer constituting the stratified panel is about 0.125 mm depending on the heated nozzle geometry.

**Table 5** - 3D-panels with different matrix infill and different superficial matrix layer

ID Panel	N. of superficial layers	Infill density [%]	Layer thickness [mm]	Panel thickness [mm]	Layup sequence
<b>Pure Onyx panels</b>					
3D-O <sub>1,30</sub>	1	30	0.125	2.0	\\
3D-O <sub>1,40</sub>	1	40	0.125	2.0	\\
3D-O <sub>1,50</sub>	1	50	0.125	2.0	\\
3D-O <sub>2,30</sub>	2	30	0.125	2.25	\\
3D-O <sub>2,40</sub>	2	40	0.125	2.25	\\
3D-O <sub>2,50</sub>	2	50	0.125	2.25	\\
3D-O <sub>3,30</sub>	3	30	0.125	2.5	\\
3D-O <sub>3,40</sub>	3	40	0.125	2.5	\\
3D-O <sub>3,50</sub>	3	50	0.125	2.5	\\
<b>Fibre reinforced panels</b>					
3D-F <sub>1,30</sub>	1	30	0.125	2.0	[0/90]sym
3D-F <sub>1,40</sub>	1	40	0.125	2.0	[0/90]sym
3D-F <sub>1,50</sub>	1	50	0.125	2.0	[0/90]sym
3D-F <sub>2,30</sub>	2	30	0.125	2.25	[0/90]sym
3D-F <sub>2,40</sub>	2	40	0.125	2.25	[0/90]sym
3D-F <sub>2,50</sub>	2	50	0.125	2.25	[0/90]sym
3D-F <sub>3,30</sub>	3	30	0.125	2.5	[0/90]sym
3D-F <sub>3,40</sub>	3	40	0.125	2.5	[0/90]sym
3D-F <sub>3,50</sub>	3	50	0.125	2.5	[0/90]sym

### 2.3.2 Cold Spray deposition

Cold spray deposition of micron-sized AlSi10Mg aluminium powders, provided by LPW South Europe, was carried out by means of a Dycomet 423 low-pressure equipment, using air as the carrier gas [123]. The powders used have a mean diameter of 20  $\mu$ m and have a spherical shape. For the first part of the experimental campaign, different coating tracks with a travel speed of the spraying gun equal to 8 mm/s were preliminarily produced by varying the process parameters in a wide range (inlet gas temperature: 150–600°C, inlet gas pressure: 4–8 bar, standoff distance (SoD): 10–80 mm). In detail, a single-track coating was developed on the surface of each laminate by spraying, layer-by-layer, aluminum particles. The number of passes of the spray gun was set to 3. The inlet gas pressure and the standoff distance were set to 6 bar and 45 mm, respectively, and

kept constant during the deposition. Different propellant gas temperatures (250°C, 300°C, 350°C and 400°C) were used to investigate their influence on the deposition of Al powder on each laminate. 12 different samples are provided with a combination of the above-mentioned parameters.

For the second set of 3D-printed substrates, the inlet gas pressure and temperature were set to 6 bar and 300 °C, respectively, the SoD was set to 45 mm and kept constant during the deposition. The coating tracks produced are shown in Fig. 35. Note that both the pure Onyx and the reinforced specimens with one layer of matrix on the outermost surfaces only are shown, for the sake of brevity.

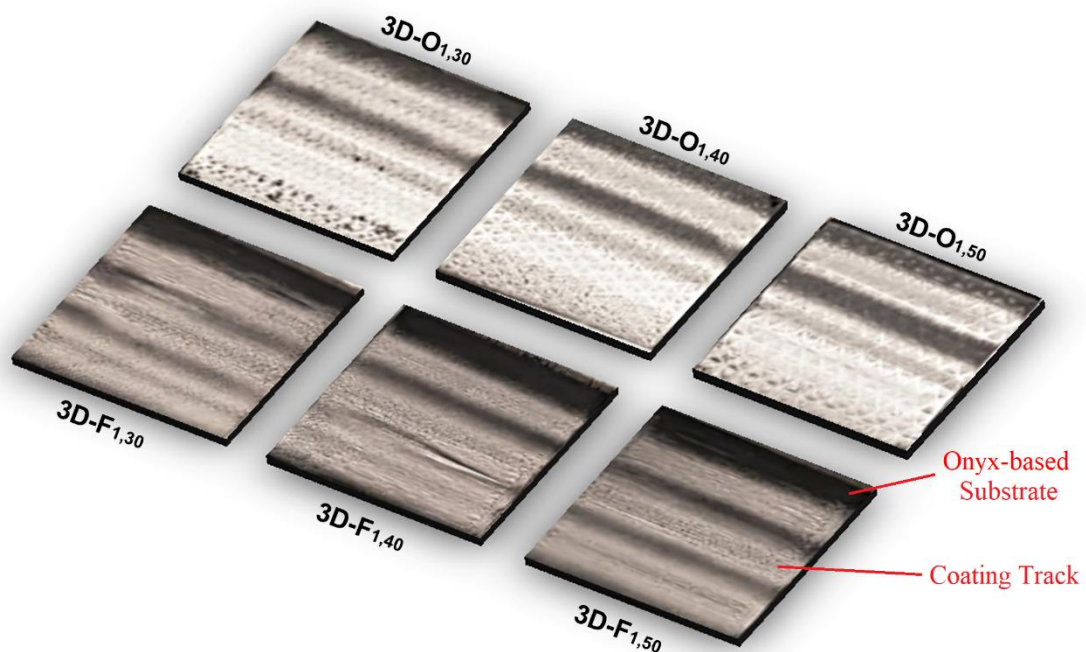


**Fig. 35** - Coating tracks made of AlSi10Mg powders produced by CS on both the pure Onyx (3D-O<sub>i</sub>) and the reinforced (3D-F<sub>i</sub>) specimens with one layer of matrix on the outermost surfaces

### 2.3.3 Coating Characterization

Microscope observations were carried out on each specimen aiming to analyze the influence of the substrate typology and characteristics on the CS deposition process. For this purpose, samples were cut perpendicularly to the sprayed surface by a precision hacksaw and observed from two different directions: top surface view and cross-section view.

The surface observations were carried out by using a Hitachi TM 3000 SEM and confocal microscope (Leica DCM3D Scan). Optical microscope analyses were also carried out. Aiming to quantify the deposition, the surface coverage and the coating thickness of each coating were

calculated similarly to what was done in previous studies. The amount of the covered surface, indicated as surface coverage, can be considered as an indicator for effective deposition, and, for this purpose, investigations of SEM images have been carried out using the commercial software Image J. To estimate coating heights and roughness measurements, the generation of three-dimensional surfaces of selected coating areas was performed through confocal analyses. After the creation of the surface, results have been exported to LeicaMap Software for the profile extraction. To analyze the morphology of the deposited particles, cross-section analyses were performed. Samples were incorporated in a thermosetting resin by a cold mounting process and then polished and metallized for SEM observations.

It is worth to note that the non-reinforced samples showed a visible distortion of the substrate due to the cold spray process, while the reinforced ones showed no distortion at all due to the obvious stiffening effect of the fibres. To quantify this distortion, indicated as  $\delta$  (%), and analyse the effects of both the Onyx infill strategy and the surface matrix thickness, the approach of Rokni et al. [124] was followed and the following formula has been used-

$$\delta = \frac{d-t-d_0}{d_0} \%$$

$d$  ( $\mu\text{m}$ ) is the distance between the lowest and the highest points of the distorted samples calculated as shown in Fig. 36,  $t$  ( $\mu\text{m}$ ) is the coating height and  $d_0$  ( $\mu\text{m}$ ) is the sample thickness before spraying. Nevertheless, in this work, the distortion was calculated as a percentage of the initial substrate thickness.

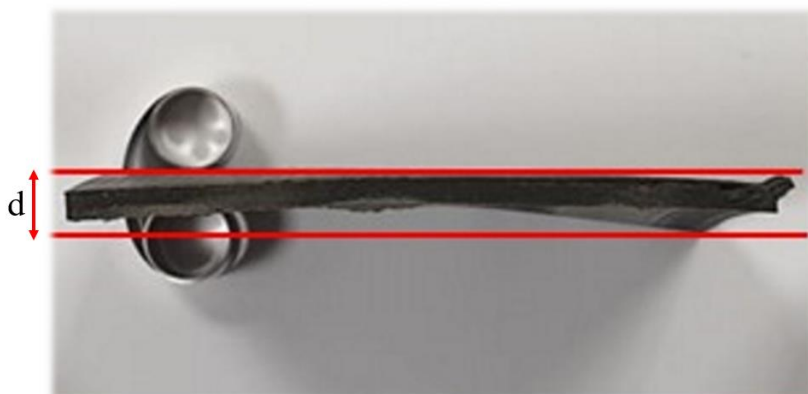


**Fig. 36** - Cross-section photography of the distorted panel;  $d$  is the distance between the lowest and the highest points of the sample

The adhesive strength was measured using following the ASTM D4541 standard and by using a PosiTest ATM. Aluminium dollies with a 10 mm diameter were bonded to the top surface of the

cold sprayed deposits using cyanoacrylate glue. Any excess adhesive or coating surrounding the dolly was removed with a drill bit. To assess the success of the test, dolly surfaces were analysed by means of an optical microscope in order to quantify the amount of the removed coating.

## **CHAPTER 3 - Cold-sprayed metallic coating on composite substrate**

### **3.1 AlSi10Mg metallic coatings on GFRP with thermoplastic matrix**

#### *3.1.1 Characteristics of AlSi10Mg coating*

From top view observations of aluminum coatings, it was found that the morphology of the sprayed powders is identical for each sample and it does not depend on the process parameters or the substrate layer thickness, as it can be assumed by observing Fig. 37. Preliminary considerations highlighted the feasibility of the deposition which resulted achievable for each spraying condition but, for the sake of brevity, it was chosen to show images of a limited number of samples that are representative for all the tests. The deformed polymer surface was able to hold the particles and maintain a continuous homogeneity of the coating. Despite this, it was evident that few particles have not adhered to the substrate and left voids on the surface. Also, it can be noticed that changing the carrier gas type (air and nitrogen) did not produce any notable differences, as reported in Fig. 38. Hence, the influence of the standoff, inlet gas pressure and carrier gas type were not relevant to the powder morphology. Although the coating morphology remained the same by varying process parameters, a subsequent investigation was required to confirm the effectiveness of the deposition. To observe the homogeneity of the surface coverage among the coating length, bulk and boundary regions of the single cold-sprayed tracks were separately analyzed. In Fig. 39., examples of two different zones of the boundary (Fig.39a.) and bulk (Fig. 39b.) of an AlSi10Mg coating track are shown. From the bulk to the boundary regions, the surface appeared fully coated, which implies a successful deposition of the powders in a single track. Erosion of the substrate was not evident; this indicates that the particles' velocity was limited to the window of deposition. As known, this window is strictly dependent on the types of the powder and the substrate.[125] Unsurprisingly[126], powders' deformation was relatively low and the original spherical shape was maintained. In the bulk region (Fig. 39b.) the particle-particle interaction could be attained.

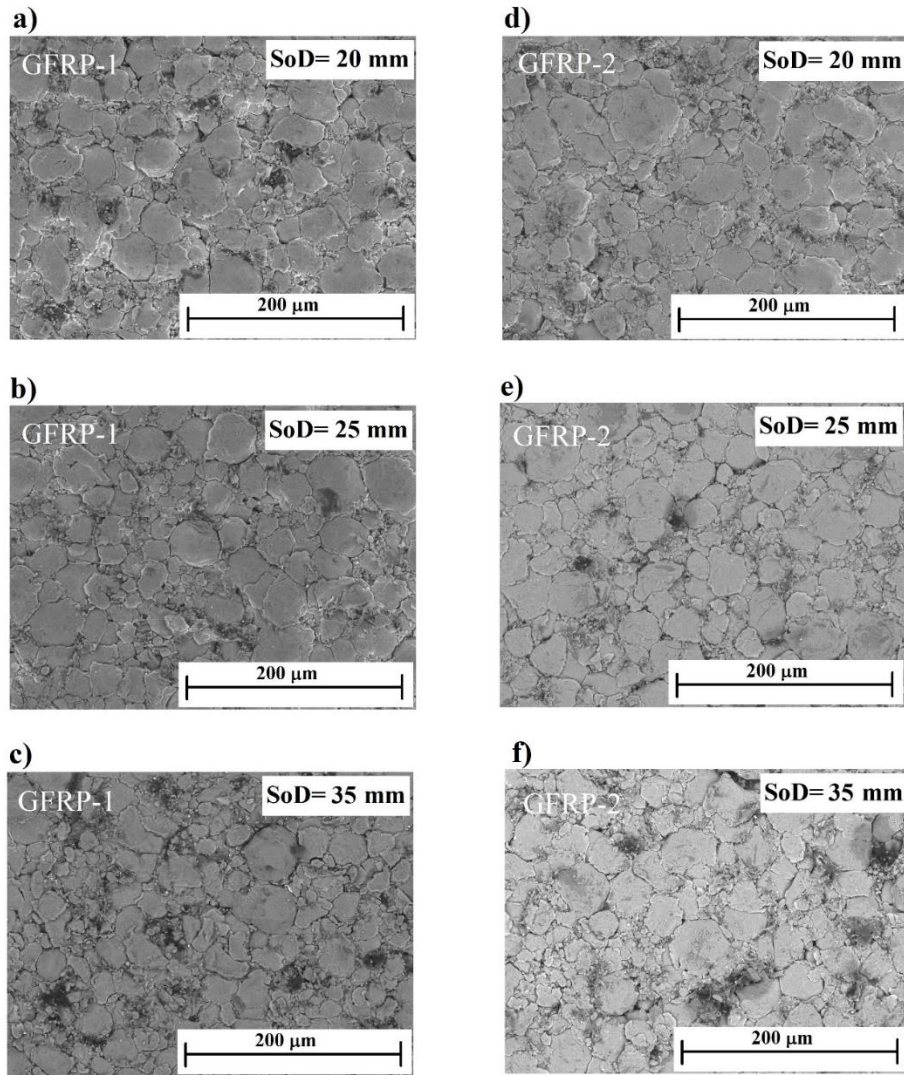


**Fig 37** - Top view acquisition of AlSi10Mg coatings sprayed with air on GFRP-1 laminate (a) (b) (c) and GFRP-2 laminate (d) (e) (f) at fixed pressure  $p = .5$  MPa.

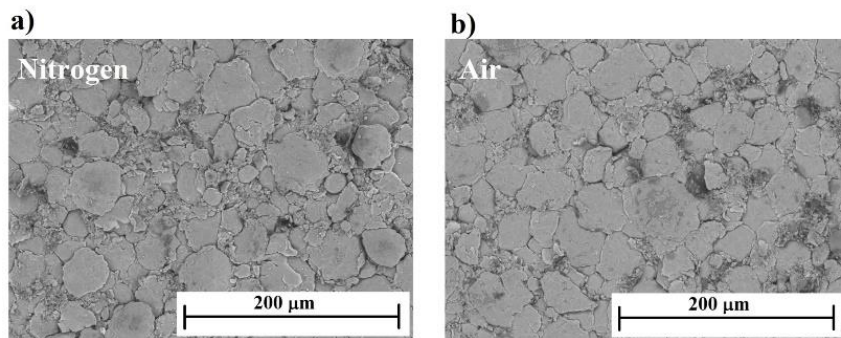


**Fig 38** - Top view acquisition of an AlSi10Mg coating sprayed with nitrogen (a) and air (b) at fixed pressure  $p = .6$  MPa and standoff SoD = 35 mm.

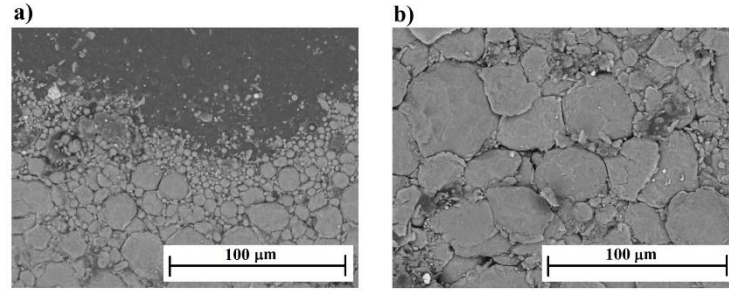


**Fig 39** - Top views of boundary (a) and bulk (b) region of a single sprayed track.

Anyway, boundaries between particles were distinct, this occurrence suggests that no metallurgical bonding has occurred and, consequently, low densification of the coating was expected. Given these observations, the amount of surface coverage for each sample was analyzed only for the bulk region. As evidenced in Fig. 40, the surface coverage values were extremely high and different trends can be observed.

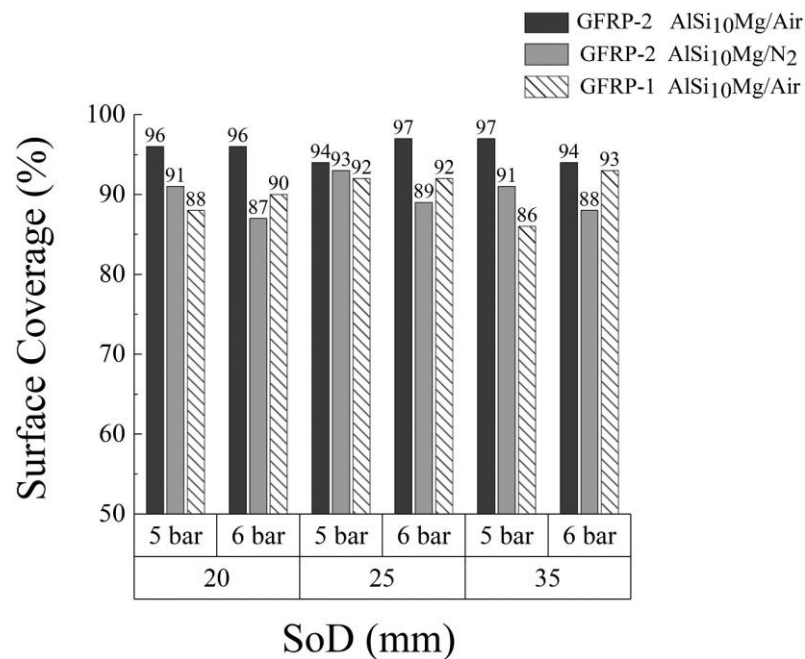


**Fig 40** - Surface coverage measurements.

The highest surface coverage occurred when spraying AlSi10Mg powders on a GFRP-2 panel by using air as a carrier gas, while the lowest average surface coverage occurred when spraying on the same panel by using nitrogen as a carrier gas. On the other hand, better coverage is obtained when the substrate layer is thicker, the powder embedment is refined, and better coverage is obtained. When substrate layer thickness is reduced, the particles' embedment is lower and consequently minor surface coverage is achieved. It can be noticed that all the different

investigated spraying conditions led to the achieving of reasonable values of the surface coverage, suggesting that the deposition correctly occurred.

The measure of the coating height highlights the deformation of the powder and how particles have adhered or penetrated in the substrate.[124] As mentioned above in section 2.3, coating height measurements were performed through the confocal microscope analysis of the coating surface and then with the optical microscope after the specimen preparation. Both measurements were summarized and compared in Fig. 41.

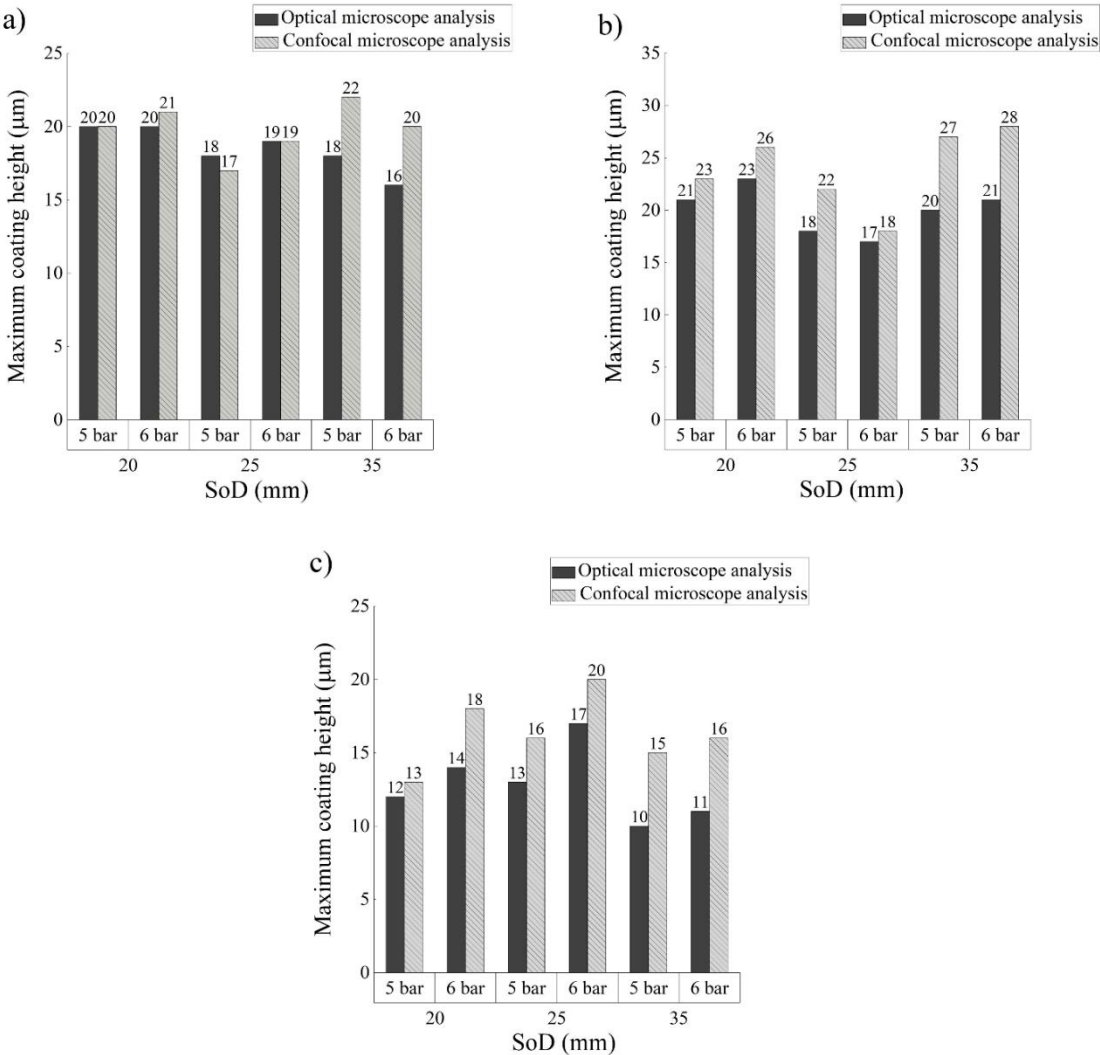


**Fig. 41** - Maximum coating height of AISi10Mg samples sprayed on GFRP-1 with air (a), GFRP-2 with air (b) and GFRP-2 with nitrogen (c).

The results were plot against, respectively, standoff distance and pressure. A general trend of the coating height is evident with the confocal analysis. The highest values of the coating height correspond to the highest SoD distance while the lowest value corresponds to the medium SoD distance. This behavior suggests that at higher SoD at 35 mm particles do not penetrate the substrate and the impact energy is not significant for the embedment; powder velocity is reduced

as the temperature. At lower SoD at 20 mm, particle velocity upon impact is higher, temperature rises and the powder embedment is heightened despite deformation. These statements need to be confirmed through cross-sections observations of the samples that will be shown in the next section. Besides, from these graphs, it is evident that aluminum coatings experienced height reduction after the samples' preparation phases. The preparation of the specimens, as reported above, consists of the cutting of the samples with a manual handsaw. As known, adiabatic shear instability and thus metallurgical bonding does not occur between metal powder and polymer surface[68]; the bonding is only mechanical and the low adhesion might make easier the mechanical removal of the particle. As a confirm of these reports, a clear tendency for the coating reduction can be distinguished for each sample. Coating reduction is not relevant by increasing SoD except at the highest SoD distance. When SoD is fixed at 35 mm, the coating height after the deposition is the highest while it is the lowest after the sample preparation. It can be supposed that particles are not accelerated enough to deform and to anchor onto the substrate. Lack of bonding, and consequently low adhesion, does not ensure a uniform coating at higher SoD. Considering the cross-section shown in Fig. 42., it is clear that only a small amount of particles have remained adhered on to the substrate and few voids in the coating can be spotted.

It is assessed that the coating thickness of the first sprayed layer mainly depends on the amount of powders' deformation.[42, 124] Fig. 43. shows coating thickness results for each substrate. The overall trend of coating thickness is similar: it decreased by increasing SoD distance from 20 mm to 25 mm and then increased from 25 mm to 35 mm.

The interaction with the substrate was affected by powders' velocity and gas pressure for different SoD parameters. When SoD was fixed at 20 mm, particle velocity was higher and the temperature of the thermoplastic substrate reached a superior value. The temperature increasing facilitated particle embedment into the surface without any considerable deformation. When SoD was at 35 mm, particle velocity was extremely reduced, impact energy did not ensure good deformation and penetration was not adequate for bonding. In this last case, lack of deformation and particle penetration resembled less adhesion. At medium SoD of 25mm, the smaller coating thickness occurred. A similar trend corresponds to the coating heights from Fig. 42.; it is evident that the smallest thickness corresponded to the smallest coating height. The results showed that when changing gas pressure, at each fixed SoD parameter, the coating thickness was altered. In particular, when increasing gas pressure from 0.5 MPa to 0.6 MPa coating thickness was increased probably due to the enhanced particle penetration into the substrate.

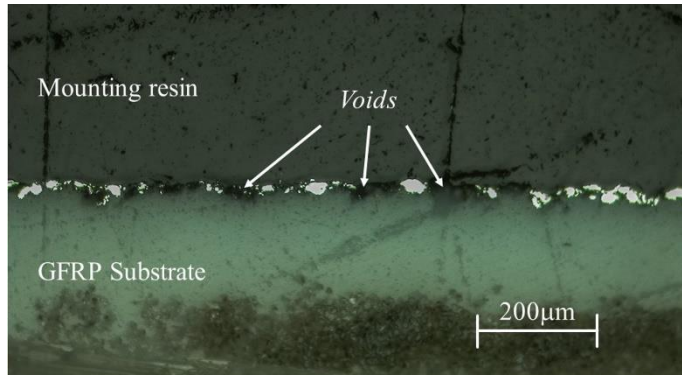


**Fig. 42** - Cross-section of AlSi10Mg coating on GFRP-2 sprayed with air at fixed pressure  $p=0.6$  MPa and SoD=35 mm.

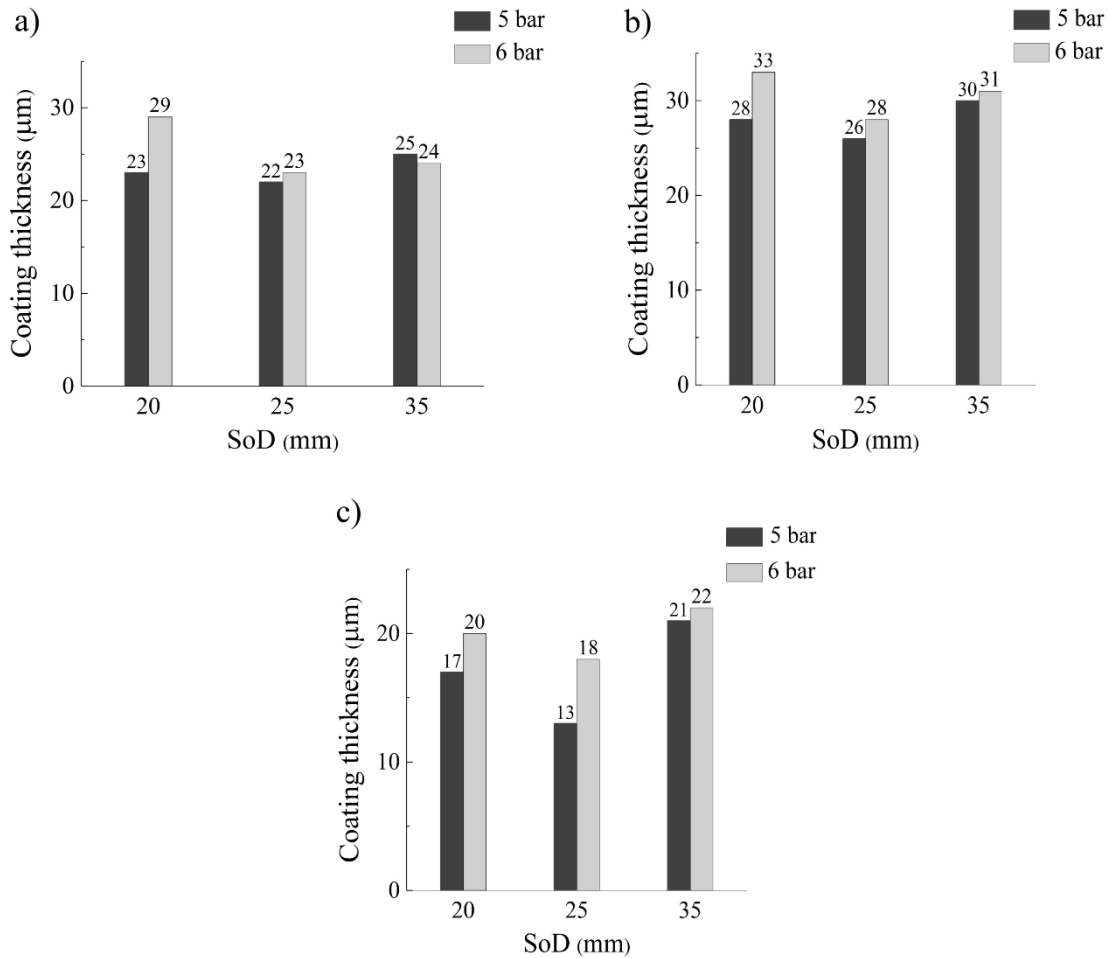


**Fig. 43** -Coating thickness of AlSi10Mg samples sprayed on GFRP-1 with air (a), GFRP-2 with air (b) and GFRP-2 with nitrogen (c).

Considering the carrier gas, the comparison of different samples highlighted that the coatings of the specimen realized with nitrogen as carrier gas were the smallest and more deformed, resulting in a compact and denser coating, while coatings realized with air as carrier gas were thicker, ensuing less homogeneity.

To understand the interactions between particles and substrate, cross-sectional observations are required. SEM analysis of cross-sections confirmed a suitable adhesion: particles had penetrated the substrate throughout the coating length. The SEM micrographs of coated GFRP are presented in Fig. 44. A dense and uniform cross-section of the Al powder coatings is presented. The coating thickness of the first sprayed layer is related to both the powder and the substrate deformation; the deformation of the PP and the AlSi10Mg powders embedment ensured an adequate bonding between the coating and the substrate.

As known, particle velocity depends on the particle dimensions: particles with higher dimensions are more accelerated and accordingly they can reach the critical value for deposition. Then, for smaller particles, the possibility of deformation is reduced. With appropriate velocity, sprayed powders embed onto the substrate while the polymeric material is squeezed out. The polymer flow surrounds the aluminum particles and allows mechanical anchoring. As expected, the deposition of light materials such as aluminum is easier to achieve and no interlayer is needed.

With close examination of the coating/substrate interface, severe deformation and some interfacial defects such as cracks were observed. A successful mechanical interlocking of the deposited Al particles could be facilitated by a thermal softening of the thermoplastic substrate. In the case of thermoplastic polymers, cold spraying at a temperature higher than  $T_g$  (glass transition temperature) of polymer materials can lead to deep particle penetration into the substrate and good interlocking between particles and substrate.[127] A good penetration does not happen at a temperature below  $T_g$ , whereas the particles' anchorage may be insufficient. Considering the low melting temperature of PP, thermal softening is a sizable phenomenon. As shown in Fig. 45., interfacial mixing could be observed at the interface between particle and substrate. Thermal softening of the polymer can promote the bonding between cold-sprayed powder and substrate, the interface between the two elements was not clearly distinct and both materials looked mixed.

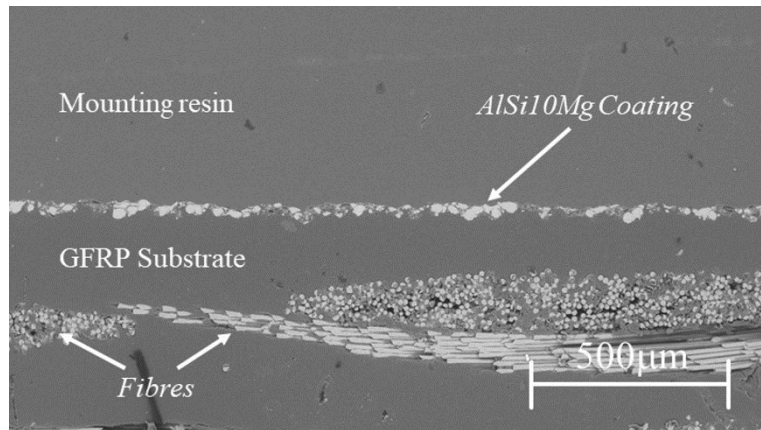


**Fig. 44** -Cross-section of AlSi10Mg coating on GFRP-1 sprayed with air at fixed pressure  $p=0.5$  MPa and  $SoD=25$  mm.

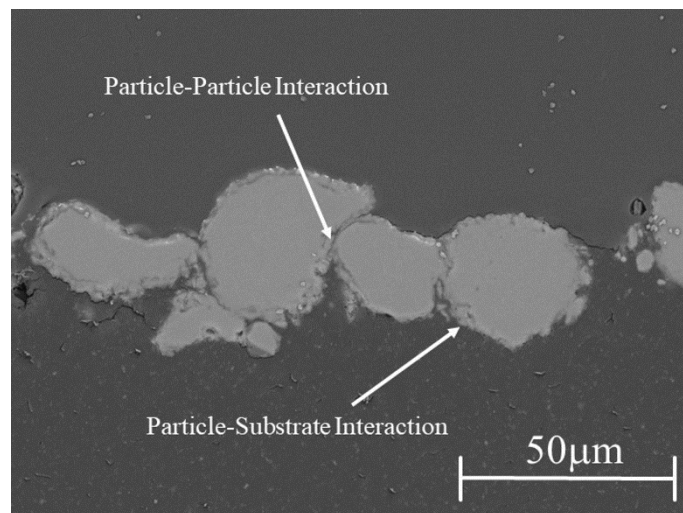


**Fig. 45** - SEM acquisition of AlSi10Mg coating.

The above-described behavior was attributed to a combination of the chosen Cold Spray parameters and substrate properties, such as hardness.

### *3.1.2 Influence of substrate manufacturing and process parameters*

#### *3.1.2.1 Effect of substrate layer thickness*

When spraying on FRPs the erosion of the fibers is one of the main issues and, for this reason, several authors stated that a superficial matrix layer is needed to facilitate the build-up of the metal coating.[125] The influence of the thickness of this layer is still unclear.[42, 128] To highlight the influence of the thickness of the superficial layer the data presented in the previous section are rearranged and showed in Fig. 46. and Fig. 47.

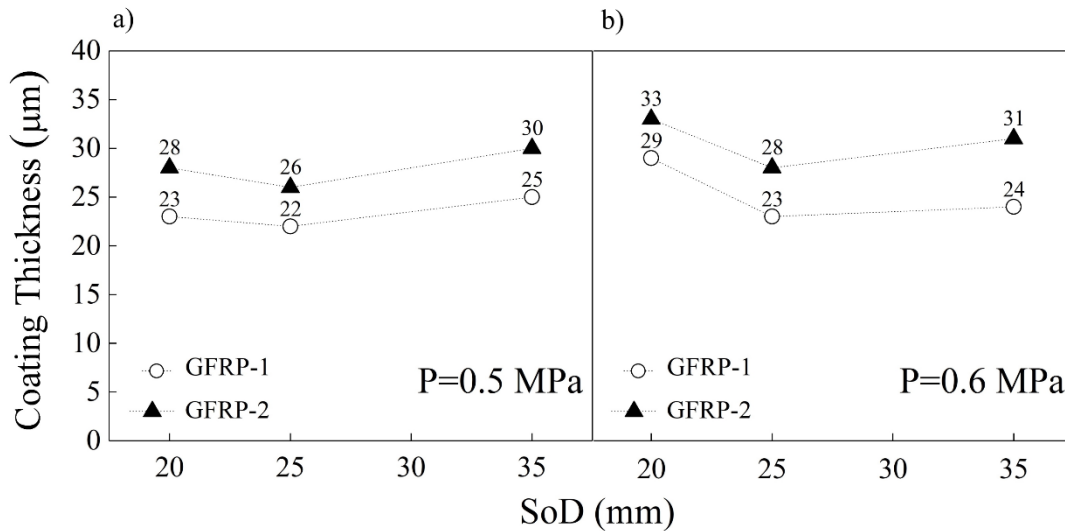


**Fig. 46** - Influence of SoD on coating thickness at 0.5 MPa (a) and 0.6 MPa (b).

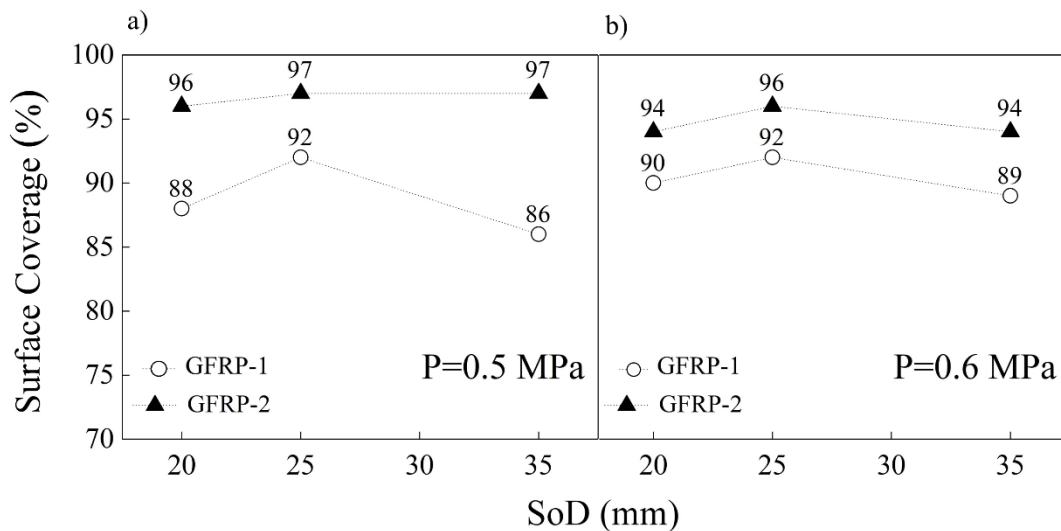


**Fig. 47** - Influence of SoD on surface coverage at 0.5 MPa (a) and 0.6 MPa (b).

Concerning the coating thickness, a lower value corresponds to higher particle deformation[124], which usually leads to better performances of the coating[51]. On the other hand, better surface coverage was observed by increasing the thickness of the polymeric surface layer. This is a complex result, but an explanation is exposed. The deformation of the particles, i.e. the coating thickness, is mainly influenced by the stiffness of the substrate: for a certain particle with given impact energy, the higher the stiffness of the substrate, the higher the deformation experienced by the particle.[124, 129] Moreover, if the substrate is thick enough, only the upper part of the substrate contributes to the cold spray deposition[72]. This behavior is not difficult to understand. For example, if we use as a substrate an aluminum sheet placed on a steel fixture of course only the properties of aluminum will influence the deposition process. Anyway, it is widely accepted

that for FRPs the stiffness of the whole structure is ruled by the fibers[130]. What is happening in our experimentation is that, by increasing the thickness of the polymeric superficial layer, the effect of the fibers on the stiffness is reduced. It can be assessed that if this superficial layer is thick enough, the effect of the fibers can be neglected and the FRP, concerning the cold spray deposition, behaves as a polymer. On this purpose, Gillet et al.[42] analyzed the influence of a single and a double PEEK layer on the FRP surface. They proved that the coating characteristics were similar for both composites but single PEEK samples showed irregular coating-substrate interface that rooted to a higher peeling effect compared to double PEEK samples. Accordingly, under a certain value of substrate thickness, the samples exhibited a not homogeneous and well compacted coating-substrate interface. That behavior can be addressed to a lower contribution of the elastic modulus and elastoplastic behavior when spraying on a single PEEK substrate, which is opposite when spraying on a double PEEK substrate. In this last case, higher resistance to the incoming particle of the subsequent layers is expected. Taking into account the experimental outcomes showed in this paper, it can be assumed that when spraying on a thicker substrate the elastic behavior of the PP substrate is more pronounced and particles experienced a lower deformation upon the impact. Lower deformation denoted less homogeneity and less continuity of the coating.[65] This could be attributed to an enhanced squeezing out the effect of the polymer due to the viscosity of the thermoplastic polymer, leaving few voids between the particles. Furthermore, for greater thicknesses, the effect of the overall stiffening of the panel caused by the fibers is completely lost and the substrate can be assimilated to a polymer substrate without reinforcement. If the substrate layer is too low, the deposition could be less effective as the fibers would cause the panel to be too stiff, not allowing the polymer to deform enough in order to embed the sprayed powder. Bringing together the cited literature and the results discussed in this paragraph, it is possible to theorize that there is a certain value of “t” below which the presence of the fibers can effectively influence the deposition.

Another important consideration is that samples with a higher “t” value showed a better surface coverage. Probably, when the substrate is “softer”, the particles can be more embedded into the substrate, even for lower values of the impact energy, resulting in higher deposition efficiency and higher surface coverage. This statement is supported by the fact that the deposition is easier on polymers without reinforcement, as reported in the available literature.[131]

### 3.1.2.2 Effect of process parameters

As already discussed for metal/metal deposition[132, 133], the influence of the standoff distance is a relevant parameter for the powder deposition. The choice of the standoff value should be set in order to guarantee both high deposition efficiency and low oxidation of coating for temperature-sensitive materials such as thermoplastic polymers.[134] Besides, when spraying on thermoplastic polymers, deposition becomes even more difficult because the standoff distance rules two different phenomena: the impact velocity of the particles and the temperature of the substrate (these influences can easily be neglected when spraying on metals). Decreasing the standoff distance results in an increase of the impact velocity and temperature of the substrate, the latter will consequently lead to a softening of the polymer[126]; as discussed in the previous section, the amount of deformation experienced by the particles depends on the stiffness of the substrate and the impact velocity. It is possible to predict a complex effect of the standoff on the deposition: a decrease of the standoff will lead to higher impact velocity with unclear influence on the particle deformation and adhesion. Looking at the results shown in the previous section, it is possible to observe that the coating thickness decreases when the SoD increases from 20 mm to 25 mm and then increases when SoD increases from 25mm to 35 mm. When SoD is fixed at 20 mm, substrate temperature and particle velocity are the highest; powder penetration is facilitated by both higher viscoelastic flow of the polymer, due to the temperature rising, and to the higher particles' velocity, which causes more erosion. Besides, for the maximum SoD at 35 mm, a worse surface coverage is achieved. From Fig. 46., coating height is shown to be the highest, which means that particles are not sufficiently deformed, they are not embedded into the surface and mechanical interlocked. In fact, as seen in Fig. 46., it is transparent that particle adhesion onto the substrate is too low and that the coating reduction is more prominent with spraying at SoD of 35 mm. The low adhesion could be attributed to less plastic deformation of the particles, to weaker mechanical interlocking with the deformed substrate and the evident absence of material jetting. Substantially, the coating obtained for a fixed SoD at 25 mm exhibits the lowest thickness. This SoD value is found to be a compromise between highest surface coverage and lowest coating height and can guarantee greater adhesion between the coating and the substrate, namely, a greater deposition efficiency of the CS process. As a preliminary conclusion, regarding the influence of the standoff distance, it can be assessed that an optimal value of the standoff should be find out for each substrate/powder system and considering the spraying conditions. Regarding the materials, more emphasis should be put on the plastic behavior of the material of the particles and on the properties of the thermoplastic matrix.

The influence of the carrier gas inlet pressure on the coating realization was analyzed by considering constant other parameters (SoD and matrix layer thickness). Even if results were quite

similar, for higher pressure (0.6 MPa), more particles can penetrate the substrate and consequently coating thickness is increased. At the same time, the particle's velocity increases by increasing the gas pressure and the coverage of the substrate are slightly enhanced as observed in Fig. 45. Such a result was observed also by Giraud et al.[126] who stated that by increasing the carrier gas pressure the particle penetration into the polymer increases. Anyway, at higher pressure, the deformation of the particle does still not occur while the substrate could be easily deformed or even cracked. Nevertheless, deposition also depends on the viscoelastic flow properties of the polymer which could cause varying degrees of penetration for particles. Gillet et al.[124] found out that the higher coating thickness corresponds to the lowest adhesion, which can be related to both the lower deformation of the powder and the inhomogeneity of the coating. Accordingly, higher deformation of the powders and homogeneity of the coating at lower pressure can guarantee a better adhesion of the first sprayed layer.

The nature of the carrier gas is relevant for the cold spray deposition and the growth of the coating.[135] Raelison et al. compared cold spray deposition of metal powder on a metal substrate by using air and nitrogen as the carrier gas.[136] Any substantial discrepancies are shown; the DE resulted almost identical in both cases for fixed process parameters and powder size. Substantial improvement could be achieved only when using helium as the carrier gas, but this gas' using conspicuously increases the cost. Anyway, the amount of powder deformation and the flattening ratio depends on different factors, including the oxide layer film. Li et al.[137] proposed that the oxide layer around the particles is supposed to breakdown upon the impact onto a metal substrate and to be partially removed from the coating. Kang et al. [138] found out that the powder deformation depends on the oxide layer film; when the oxide film is thicker, part of the impact energy is used up to disrupt the oxide layer and consequently less energy is dissipated for the plastic deformation of the particle. Besides, Li et al. verified that lower oxide content (i.e. thinner oxide film) corresponds to lower critical velocity of the particles.[139] Both these findings can be useful to understand the results of the present experimental campaign, where the coating thickness is found to change when varying carrier gas. In particular, the particles' deformation results slightly enhanced when using N<sub>2</sub>; consequently, coating thickness is inferior. Such behavior could be attributed to lower oxidation of the particles when using nitrogen, due to the lower oxygen content. Consequently, it can be assumed that, when using nitrogen, the influence of the gas on both the growth of oxide thickness and critical velocity can enhance the flattening ratio of the deformed particles.

## **3.2 Steel 316L metallic coatings on GFRP with thermoplastic matrix**

### *3.2.1 Characteristics of Steel coating*

The deposition efficiency of the various samples of the experimental campaign has evidenced low values of less than 10%, which ties well with previous studies[42, 127]. Anyway, for each set of process parameters, similar deposition efficiencies values are given and the influence on the other process parameters is not relevant. For this study's purpose, to evaluate the feasibility of the process and the effectiveness of the deposition throughout the single track, two different zones of each steel 316L coating, indicated as boundary (the external part of the track) and bulk (center part of the track), have been separately observed from the top-view direction.

As shown in Fig.48, the bulk region (Fig. 48b) is characterized by a good amount of deposition, the surface appeared widely coated with the presence of few voids between the particles. Anyway, the absence of appreciable powder deformation limited the particle-particle interaction and as a consequence, the coating is not completely compacted and homogeneous, showing uncovered spaces in the deposit. On the other hand, at the boundary region (Fig. 48a) the number of deposited particles appeared to be extremely lower compared to the bulk region and a lot of "impact craters" can be spotted on the surface. This fact does not suggest that the deposition cannot occur in the boundary zone but that these craters may be caused by the low impact velocity of the steel particles: particles impact onto the surface, deform or crack the surface and then rebound without stacking into the substrate due to the poor adhesion.[75] This behavior could be attributed to the variation of the mean particle velocity profile[140] which sharply drops when retreating from the nozzle axis.

Even if no damages of the surface were detected, preliminary observations indicate that steel powders do not sufficiently deform in contact with the polymer surface, leading to a non-homogenous and non-compacted first sprayed layer. This behavior can also be attributed to the spherical shape of the powders; the particles just stuck into the substrate, similar to what was observed by King et al.[66] for copper particles: spherical powder, thanks to their shape, showed deeper penetration but cannot guarantee homogeneous and well-compacted coating, while irregularly shaped particles have more contact points with the substrate and, consequently, higher homogeneity can be reached. Without significant particle deformation, the bonding can only be achieved by the substrate deformation, but it must be to the right amount to limit polymer damage or erosion. It could be assumed that the particle energy does not reach the minimum critical value and, as evidenced by the sequence in Fig. 49, changing the SoD or the gas pressure parameters did not produce any notable improvement in the amount of the deposition in the boundary region.

Hence, it is obvious that the presence of the impact craters mainly depends on the properties of the chosen metal powder, such as density and size distribution, which directly affect the powders' velocity.

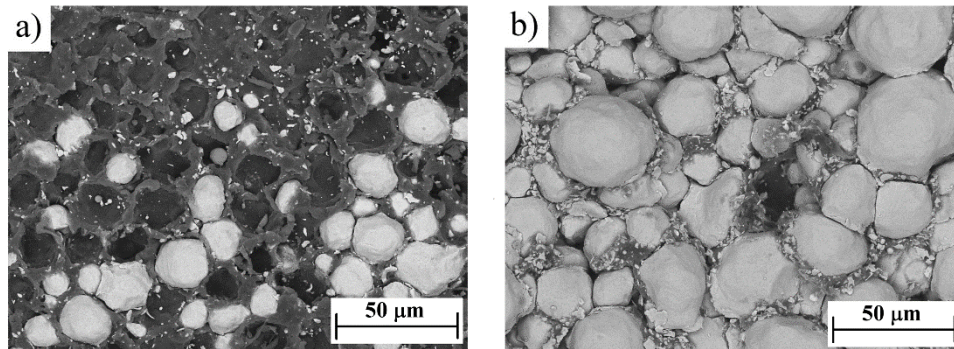


**Fig. 48** - SEM magnification of steel coating on GFRP-2 S.O.=25 mm p=5 bar a) boundary b) bulk.

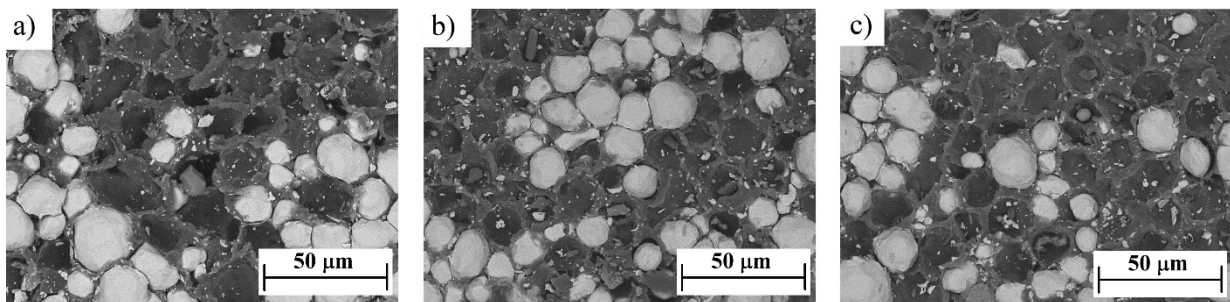


**Fig. 49** - SEM magnification of boundary zones of steel coatings on GFRP-2 at p=0.5 MPa and a) S.O.=20mm, b) S.O.=25mm, c) S.O.=35mm.

Considering all the above-mentioned observations, from bulk to boundary region the powder morphology and the deposition behavior appeared to be similar for each set of process parameters and each panel type. In all the cases, the particles retain their original shape, deformation of the powder has not occurred and the borders of the particles are distinct and defined. Anyway, it is critical to note that throughout the single track, the coating is obtained without evident damages or erosion of the substrate. Since the cold spray deposition is usually obtained with different overlapped spray passes and different strategies[141], only the bulk of the coating gains major interest. In the following outcomes, only the bulk sections were considered for the surface coverage characterization. All the results were summarized in Fig. 50 and graphed against SoD and pressure. As evidenced, surface coverage values in bulk sections are extremely high, leading from a minimum of 82% to a maximum of 93%. When increasing the substrate layer thickness, a clear trend of increasing surface coverage is evident. Another significant trend reveals that the surface coverage increases when increasing the gas pressure. Overall, these results indicate that when using a thicker polymer layer thickness and higher gas pressure, deposition is improved. On

the other side, no clear trend has been noticed when increasing the SoD distance. Therefore, it does not seem to be an obvious relation between surface coverage and SoD influence. To understand the quality of the mechanical anchorage and how it affected the powder embedment, an analysis of the coating height is necessary. Nevertheless, it was noticed that the measurements of the coating height significantly changed from different acquisitions taken before and after the metallographic preparation of the specimen. As reported in Fig. 51, coating height values were compared for both sets of results. What is obvious is that, when considering coating height after the deposition, values are higher while they tend to be reduced after the specimen preparation. The main consideration from these results is that the reduction of the height is characteristic for each sample and no clear trend can be observed when increasing the SoD distance on the gas inlet pressure.

This suggests that the coating removal can be attributed to the low anchoring force and the combination of both the process parameters and differences in substrate-particles hardness. Probably, the hardness and stiffness of the substrate were too low to cause deformation, or the particle velocity was well below critical velocity. The metallic particles are not able to deform so the bonding is only activated by the polymer deformation. The interface between the coating and the substrate resulted from a polymer flow that surrounded particles that led to mechanical anchoring of these particles into the substrate while their shape remained mostly unchanged. Anyway, besides the lack of particle deformation, the absence of inter-particle interaction can play a main role in the coating homogeneity. When particles penetrate the substrate, the deformation of the polymer substrate around them resulted in their capture and the formation of the polymer cavity may prevent particles to fall out and lead to greater mechanical interlocking.[66] Hence, the combination of hard steel 316L powder on a soft polymer substrate should be considered more auspicious for the deposition. Penetration depth measurements are graphed against the SoD and pressure in Fig.52. To understand the combined effect of pressure and SoD, experiments were carried out at 0.5 MPa and 6 MPa inlet pressure. By increasing inlet gas pressure, particle penetration is increased. However, in both cases, increasing standoff distance resulted in a lower embedment.

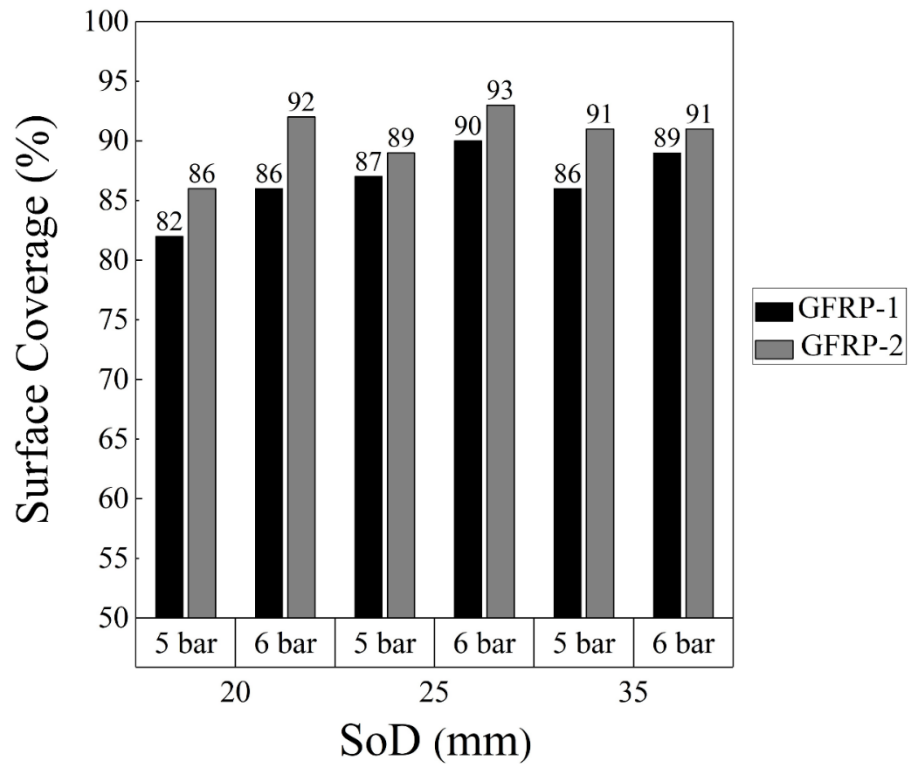


Fig. 50 - Surface Coverage measurements.

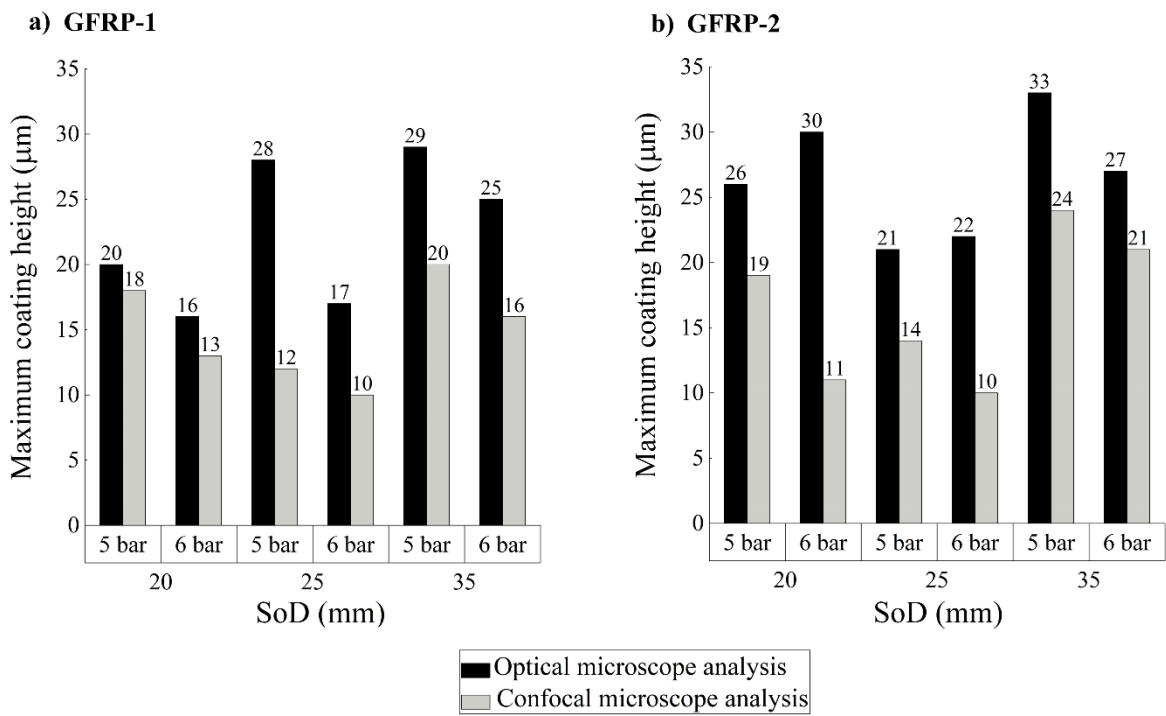
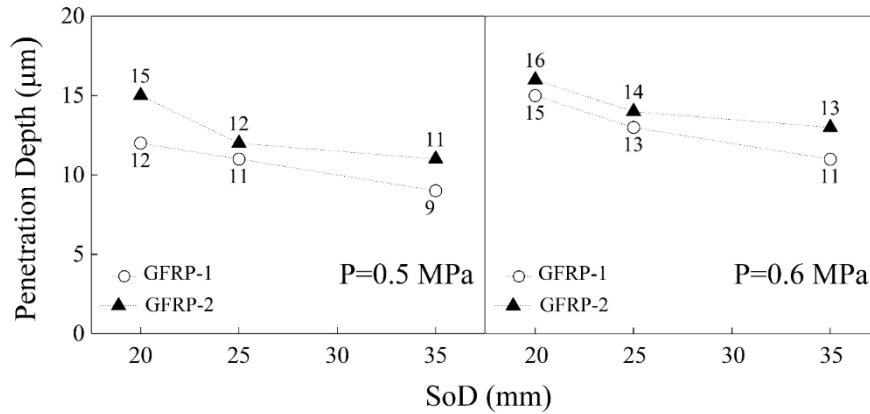
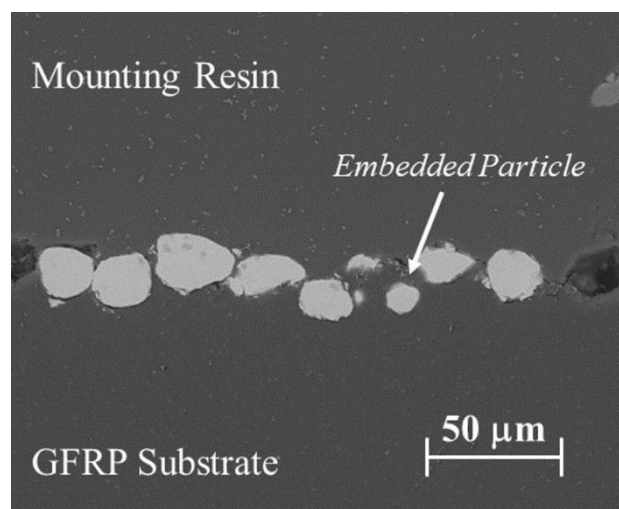


Fig. 51 - Coating Height measurements.



**Fig. 52** - Penetration Depth measurements.

On the other hand, few differences in the response of the two substrates can be noticed. A similar tendency against SoD and pressure could be observed on both the substrates, except the more pronounced depth of penetration on the GFRP-2 substrate as compared to the GFRP-1 substrate. Although there is a high difference between the properties of PP and the steel 316L, the particles are not driven deep into the substrate and rather, most of them, remain partially off the surface. Even if it is demonstrated that bigger particles can reach lower value critical velocity[100], in the present case it seems that only small particles can embed more into the substrate. As seen in Fig.53, smaller particles penetrate deeper into the substrate and get anchored, with an evident interaction with the polymer. This embedment is due to a combination of particle size and velocity. Contrarily, for larger particles, the interaction zone around them can barely be observed. Particles did not penetrate the substrate but instead they superficially attached, which implies the already discussed inadequate anchorage.



**Fig. 53** - Sem magnification of cross-section of steel coating.

### *3.2.2 Influence of process parameters*

#### 3.2.2.1 Deposition mechanism

In previous studies, Ganesan et al. found out that, when spraying denser powder with a higher yield stress, the realization of the coating is not easy to attain and, in some cases, an interlayer of softer powders, such as tin, is required[73], especially when using high-pressure cold spray equipment. Despite these considerations, this work showed that the deposition of steel powder can be achieved utilizing a low-pressure Cold Spray system. Even if no damages of the surface were detected, preliminary observations indicate that steel powders do not sufficiently deform in contact with the polymer surface, leading to a non-homogenous and non-compacted first sprayed layer. This behavior can also be attributed to the spherical shape of the powders; the particles just stuck into the substrate, similar to what was observed by King et al.[66] for copper particles: spherical powder, thanks to their shape, showed deeper penetration but cannot guarantee homogeneous and well-compacted coating, while irregularly shaped particles have more contact points with the substrate and, consequently, higher homogeneity can be reached. Without significant particle deformation, the bonding can only be achieved by the substrate deformation, but it must be to the right amount to limit polymer damage or erosion.

As observed in the “surface coverage” section, the major issue encountered with the deposition of steel powders is that a significant quantity of particles is lost at the boundary zones of the sprayed tracks. This attitude may be chargeable to the particle rebounds, as confirmed by the appreciable presence of the impact craters on the surface. A simple explanation can be detected in the differences in the particles’ profile of velocity. As known, the particle velocity is maximum at the central axis of the nozzle and then it decreased by withdrawing from it.[140] In these external zones, the particle velocity drops well below the critical velocity to cause the deformation[142] and to guarantee deeper powder penetration and an appropriate bonding. In fact, in Kromer et al. work[143], particle embedment was considered only if the particle penetrated in the polymer deeper than its radius. As already observed from top-view observations, these phenomena are enhanced in the boundary region of the single track but they are also present in the bulk region where a lot of impact craters can be spotted also in the cross-section.

In all the cases it can be assumed that the powder velocity is not high enough to reach the minimum critical velocity to successfully deposit the metal powders onto the polymer substrate.

Therefore, with the chosen powder size distribution, most of the impacted particles did not have any steady contact with the surface and hence they could peel off. It is also clear that the

phenomenon of the impact craters is shown for each panel type, suggesting that the effect of the powder velocity is more prominent than the effect of the substrate properties.

Consequently, deposition has to be considered in terms of powders properties, i.e. powder size. To overcome these issues and to reduce the presence of these craters, it could be useful to use powders with a smaller range of size distribution.

### 3.2.2.2 Effect of the laminate stratification

In the *Results* section, it is deduced that different stratification of the composite substrate produced specific results. Even though it was possible to achieve deposition on both panel types, GFRP-2 panels performed better than GFRP-1 in terms of penetration depth and surface coverage. The GFRP-1 has a specific substrate layer thickness value below which the effect of the fiber stiffening is more concentrated. From all the observations, it derives that, with a lower value of the substrate thickness, the particles will be less incorporated by the polymer flow and a higher percentage of voids in the coating is observed. These results are supported by the fact that when the matrix superficial layer is thicker, particles do not suffer from the fibers stiffening effect and the powder embedment is facilitated. Similar findings have been exposed by Gillet et al.[42] which stated that, when using two protective PEEK films on the fibers instead of one, the samples exhibited a more homogeneous and well compacted coating-substrate interface. That behavior can be addressed to a higher contribution of the elastic modulus and elastoplastic behavior when spraying on a double PEEK substrate, which is opposite when spraying on a one PEEK layer substrate. Anyway, differently from the above-cited works, these findings demonstrate that, in the case of steel powders, the mechanical properties of the substrate, i.e. stiffness, are not suitable to deform the powders and to give to the coating a certain homogeneity. Although there are differences in the mechanical properties of the two panels, the influence of the fibers is not predominant. In this condition, the interactions between the cold spray process parameters and the properties of the composite should be reconsidered to achieve a good coating.

### 3.2.2.3 Effect of process parameters

The carrier gas influence on the coating formation was analyzed by considering constant SoD and matrix layer thickness. Even if results were quite similar for both pressure conditions, for higher pressure at 0.6 MPa penetration depth of the powder and surface coverage of the substrate are increased.

It is well known that higher particles in-flight velocity are obtained for higher gas inlet pressure[144]. About this, Chen et al.[49] recently reported the effect of both pressure and velocity on the deposition of a single Cu particle on PEEK. It was found that when increasing gas pressure, the copper particles penetrated deeper into the polymer with the enhanced formation of wrinkles and jets. This phenomenon may be attributed to higher kinetic energy which causes both more mechanical penetration and more thermal softening due to kinetic energy dissipation. Such a result was observed also by Giraud et al.[126] who stated that by increasing the carrier gas pressure the particle penetration into the polymer increases with growth in powder velocity: the substrate softens when exposed to higher process gas pressure and higher impact velocity, causing enhanced polymer squeezing effect and, consequently, enhanced powder embedment. The particles are driven deeper into the substrate in contrast to the lower gas pressure.

Regarding the influence of the SoD, it has been observed that this parameter mainly affects the penetration depth of the powder, At SoD of 20 mm, the obtained penetration depth resulted to be at the maximum value: the particles could easily embed into the substrate rather than rebounding. When increasing the standoff distance, the penetration depth decrease. This is because the particles' impact velocity tends to rise for lower values of standoff distance. There is a range of SoD where the gas velocity is lower than the particle velocity and both particle velocity and particle impact velocity start to decrease. Consequently, when increasing the SoD distance, the drop in the impact velocity causes less penetration of the metallic powder. Additionally, at SoD of 35mm, the impact velocity is the lowest, the particles are not embedded into the substrate and rather remain on the surface.

Considering all the results, optimum conditions were determined to be 0.6 MPa for inlet gas pressure and 20 mm for SoD.

### **3.3 Thermosetting substrate**

#### *3.3.1 Cold sprayed coating on PLA thermosetting composites*

##### 3.3.1.1 Analysis of the substrate

The results of the cold spray depositions of aluminium particles on the basalt-epoxy thermosetting substrates with the CS coating protocol selected are reported in Fig. 54, which show the SEM cross-section images of both untreated (Fig. 54a) and PLA treated (Fig. 54b) coated surfaces.

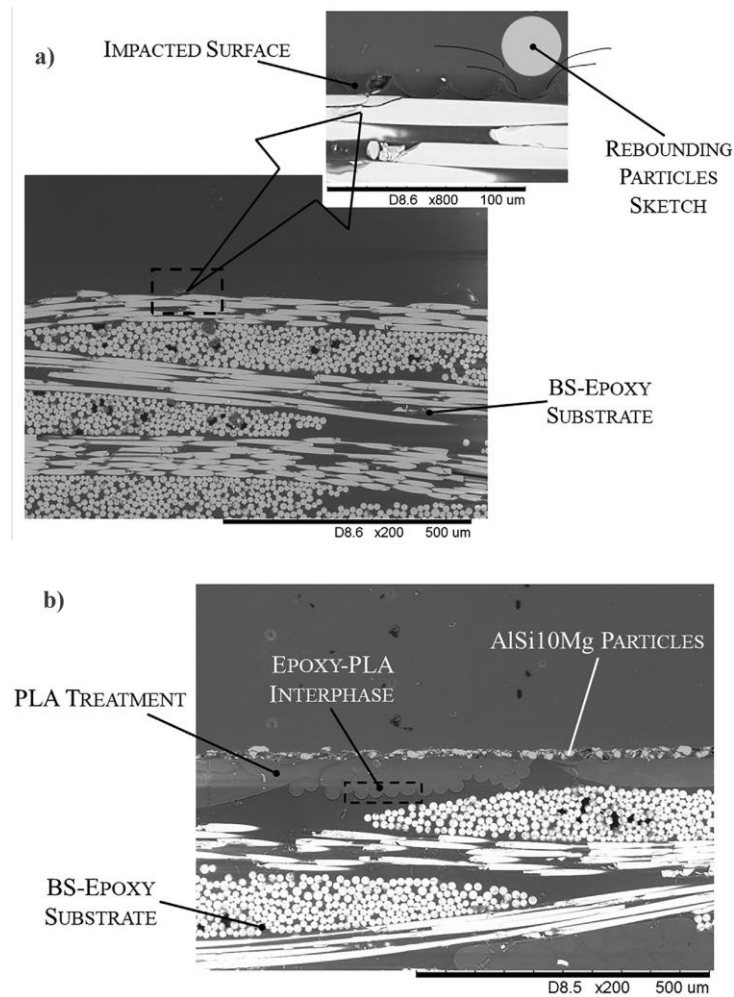


**Fig 54** - SEM cross-section images of untreated (a) and PLA treated (b) metallised BS-epoxy surfaces.

It can be seen from Fig. 54a that the metal coating formation on untreated BS-epoxy substrate is complicated, if not impossible, due to the fragile behaviour of the polymeric matrix. The result is the rebounding phenomenon of the particles that do not attach mechanically with the polymer-based substrate leaving traces and voids on the impacted surface, as shown in the insert of the Figure.

On the contrary, the PLA treatment seems to give a noticeable contribution to the deposition process of metallic particles impacting on a more plastic surface, promoting the coating formation and grow-up. It is due to PLA capability to ensure the best adhesion with the thermosetting substrate, as shown clearly by the like-waves phenomena taking place at the epoxy-PLA interphase in Fig. 54b. In fact, the thermoplastic nature of the top layer ensures the softening of the material and the resulting plastic deformation under the combined influence of pressured carrier gas and particle bombardment. The result is that the deformed ductile material embeds the sprayed particles that mechanically anchor with the surrounding polymer matrix. Therefore, the

effectiveness of PLA treatment on thermosetting substrates translates into more compact and denser cold sprayed coating. More in details, it can also be seen that the procedure, that combines two polymers of different nature here proposed, is capable of ensuring an effective anchoring between them. It happens without showing any sign of debonding during the particle deposition process, as clearly reported by the like-waves phenomena taking place at the epoxy-PLA interphase.

### 3.3.1.2 Indentation test results

Load-displacement curves at indentation using three impact energy levels ( $U = 10 \text{ J}$ ,  $20 \text{ J}$ ,  $30 \text{ J}$ ), which are smaller than the penetration energy values ( $U_p=100 \text{ J}$ ), are reported in Figs. 55 and 56, for both neat (without CS coating) and coated basalt composite systems, respectively.

The pictures clearly show that, for all the tested conditions, closed type curves are obtained: the samples are not penetrated/perforated by the impactor that rebounds from the impacted surface and the area enclosed in the loop of the loading/unloading part of each curve is the energy absorbed by the laminate to create damage or to bend. In particular, from the Figures above it can be seen that, for both neat and coated samples, with the increase of the impact energy,  $U$ , an increase of the maximum load,  $F_{max}$ , the maximum deflection,  $d_{max}$ , and the absorbed energy,  $U_a$ , occurs.

It is noticeable that the impact strength of the coated structure results higher than the neat substrate's one that absorbs a more significant amount of damage energy and shows a higher maximum deflection for all the impact energy levels used. Comparing the load-displacement curves for both the systems keeping the energy level constant (Figs 57), it is possible to notice a qualitative variation of the rigidity of the composite coated system that results higher for the latter. The stiffness is indicated by the slope of the first linear part of the curve, and it can be noted that the rigidity is positively affected by the cold spray deposition for all the impact energy values tested. It is very interesting the result obtained from the load-displacement comparison curves between coated and neat composites at  $U = 10 \text{ J}$  (Fig. 57s). It can be seen that for the metallised composite substrate, the curve seems to return on itself indicating a very low absorbed energy and a very low plastic deformation.

In the case of the coated materials, it is easy to observe that the first significant load drop occurs in correspondence of the maximum load, while, in the case of neat laminates, several load drops were observed on the increasing part of the curve, denoting delamination initiation and propagation, as well as matrix cracks and start fibre failures. Probably the metallic coating acts as a protection for the matrix and the matrix fibre interface, reducing the matrix breaks before the fibre failure.

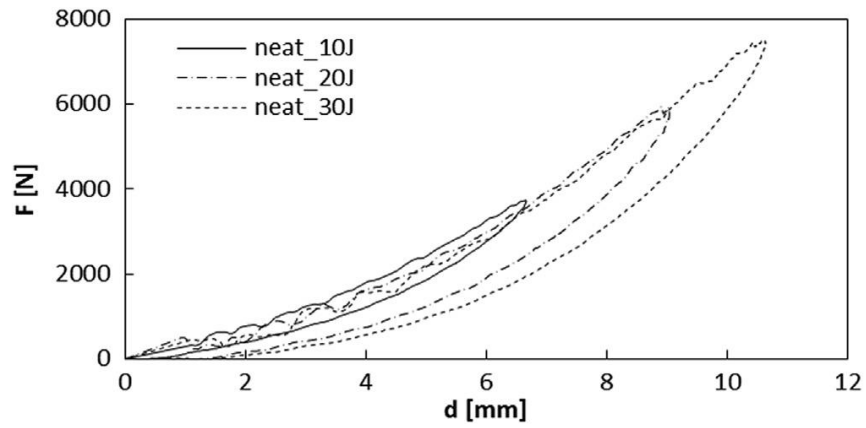


**Fig. 55-** Load-displacement curves comparison for three impact energy levels ( $U = 10 \text{ J}, 20 \text{ J}, 30 \text{ J}$ ) relative to neat composites systems (neat).

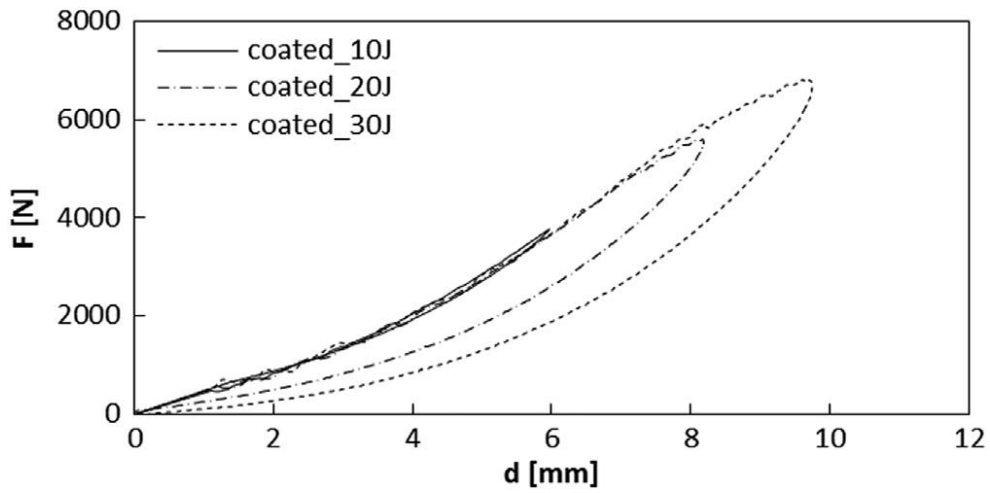


**Fig. 56 -** Load-displacement curves comparison for three impact energy levels ( $U = 10 \text{ J}, 20 \text{ J}, 30 \text{ J}$ ) relative to coated composites systems (coated).

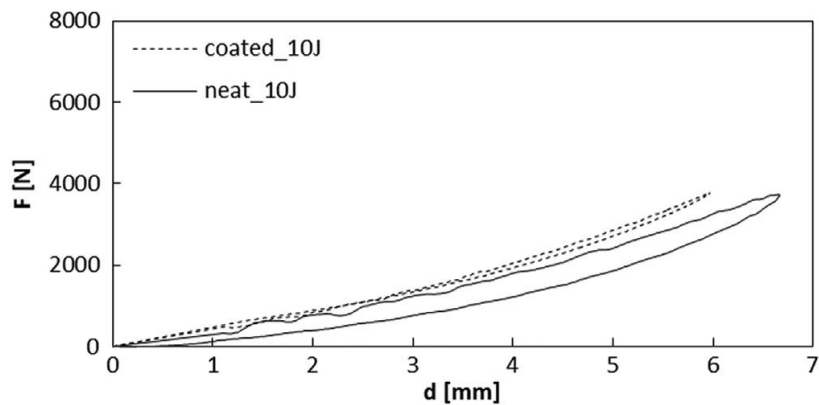


**Fig. 57 -** Load-displacement comparison between coated and neat composite at  $U = 10, 20, 30 \text{ J}$ .

What we read is predominantly the responsibility of the metal which, being anisotropic material, also reduces the presence of noise. In part, the impact energy is absorbed by the coating, reducing

the impact energy transmitted to the composite surface. That means that the aluminium coating influences the damage mechanisms by protecting the fibres. The percentage ratio between the absorbed energy, which is the energy used by the composite material to create the damage, and the impact one, is reported in Fig. 58 for the three tested conditions and for both neat and coated samples. As expected, the percentage of the absorbed energy grows as the impact energy increases for both the systems. However, the most interesting result from Fig. 58 is that lower values of the absorbed energy were recorded for the coated system indicating a higher propensity to damage of neat structure respect to the coated one. Moreover, the maximum percentage variation of the energy absorbed by the abovementioned systems occurs for the lowest value of the impact energy ( $U = 10 \text{ J}$ ); in fact, this variation tends to decrease with the increase of the impact energy levels, as shown in Fig. 59.

It can be seen that the beneficial effect of the metal coating tends to reduce with the increase of the impact energy as the neat and coated curves show the tendency to approach. The main reason is that the so thin aluminium coating can affect positively the behaviour of the polymer-based substrate for very low-impact energy levels (10 J in this case). For relatively higher impact energy values, the influence of the metal coating tends to vanish because of its thickness that seems not to be big enough to provide significant damage reduction.

Aiming to further investigate into these intriguing mechanisms, both the results from the confocal microscope for the indentation depth measurements and the C-scan acquisitions after the impact tests are reported in Figs. 60 and 61, respectively. Recall that the indentation depth,  $I$ , is the footprint left by the impactor on the impacted specimen surface. By looking at the former Figure, it can be observed that indentation tends to increase with the increase of the impact energy, for both neat and coated samples. That means the higher the impact energy, the higher the plastic deformation of the material tested. However, higher indentation depth values are recorded for neat samples respect to the coated ones, further proving the beneficial effects of metallization. At the same time, by observing Fig. 61, it can be noted that the damage shape in the coated systems appears more defined and the extension of the delamination seems to be concentrated under the impactor material contact point.

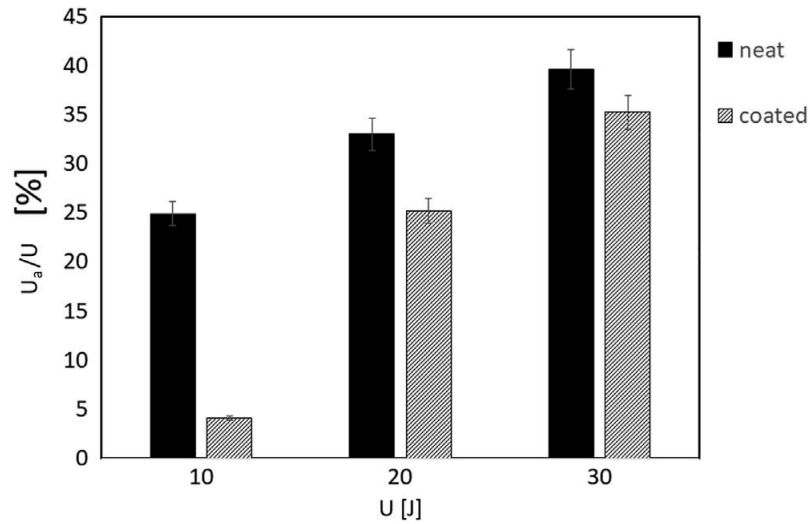


**Fig. 58** - Percentage ratio between the absorbed energy,  $U_a$ , and the impact energy,  $U$ , for the three tested conditions and for both neat and coated samples.

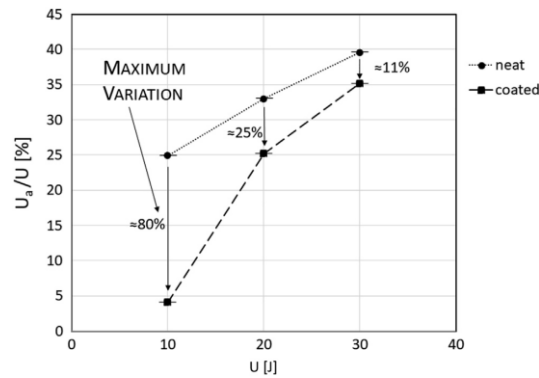


**Fig. 59** - Absorbed energy trend variation for the three tested conditions and for both neat and coated samples.

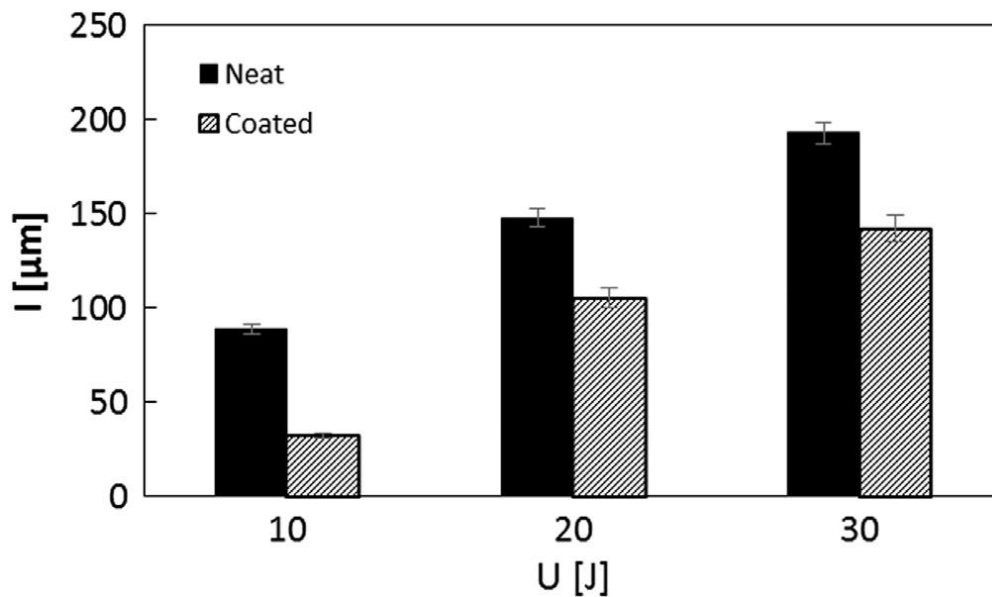


**Fig. 60** - Indentation depth. measurements for the three tested conditions and for both neat and coated samples.

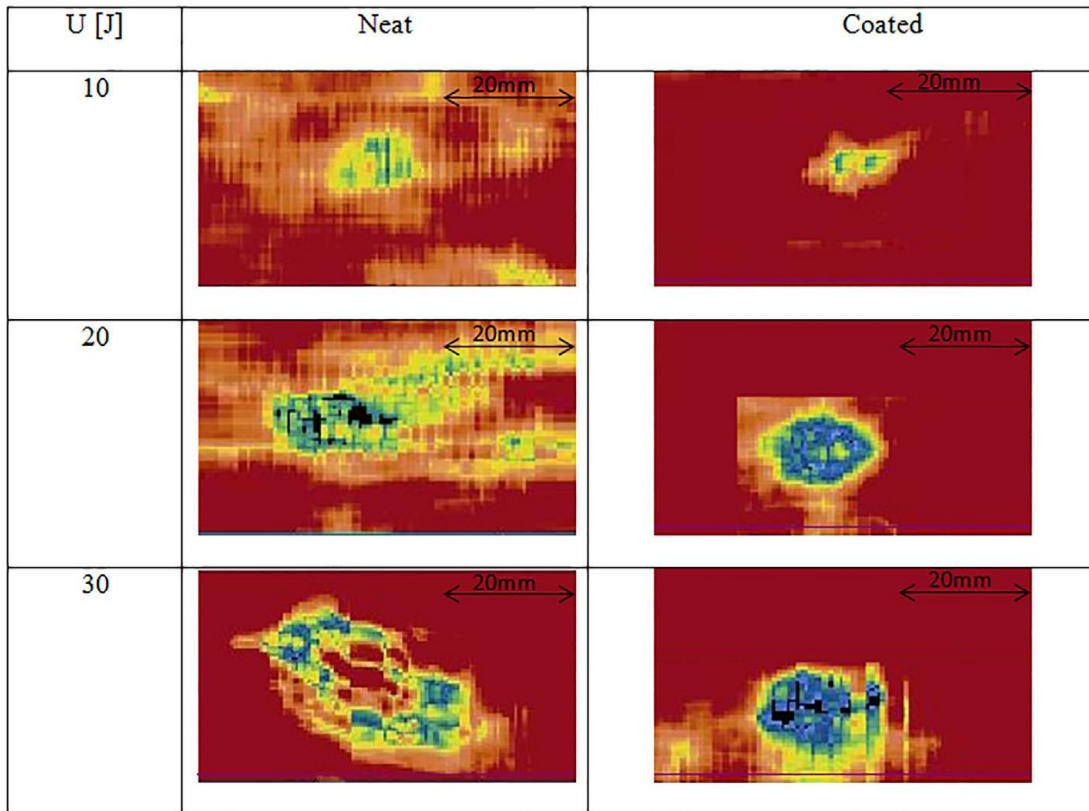


**Fig. 61** - C-scan acquisition for both neat and coated samples for the three tested conditions

In particular, the delaminated area increases as the impact energy increases for all the systems tested, as shown in Fig. 62. However, the delamination is higher for the neat composite system proving again that the metallization seems to reduce the damages and failures of polymer-based substrates.

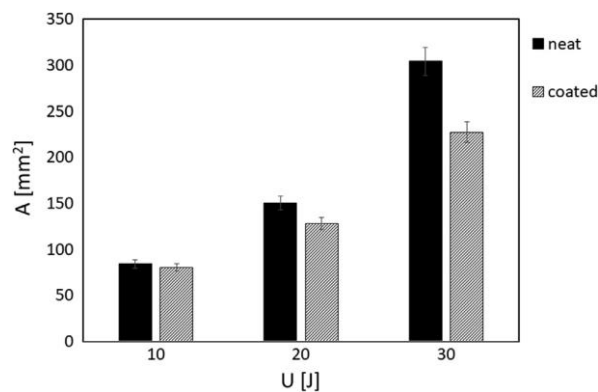


**Fig. 62** - Delamination area, A, for the three tested conditions and for both neat and coated samples.

On the base of the abovementioned results, it can be noted that at  $U = 10$  J, the very low coated substrate absorbed energy is due to the capacity of the metal coating to prevent the plastic deformation (a plastic deformation reduction of about 60% for the coated sample, as shown in Fig.

60). This result was not detected from the outcomes obtained at relatively higher impact energy values: in these cases, the coating seems not to be capable to strongly oppose the plastic deformation (smaller rates of plastic deformation reductions were evaluated, 28% and 25% for  $U=20$  J and  $U=30$  J, respectively) providing a positive contribution on the delamination (as shown in Fig. 62) rather than on indentation that starts to grow significantly. The result is that, moving from the neat to the coated system, the mechanism of the damage changes. In particular, at low-velocity impacts (10 J in this case), the coating seems to have a noticeable effect on the plastic deformation damage that strongly reduces due to the greater rigidity of the coated system. At relatively higher impact velocities, this effect tends to vanish pointing out the beneficial contribution of the metallization on delamination damage.

## CHAPTER 4 - Cold-sprayed metallic coating on 3D- Printed Onyx substrates

### 4.1 Aluminum coating on Onyx substrate (different reinforcement infill)

#### 4.1.1 Characteristics of the coatings

The powders have been cold-sprayed on the front face of each panel to benefit the effect of the texturing, as shown in Fig. 63.

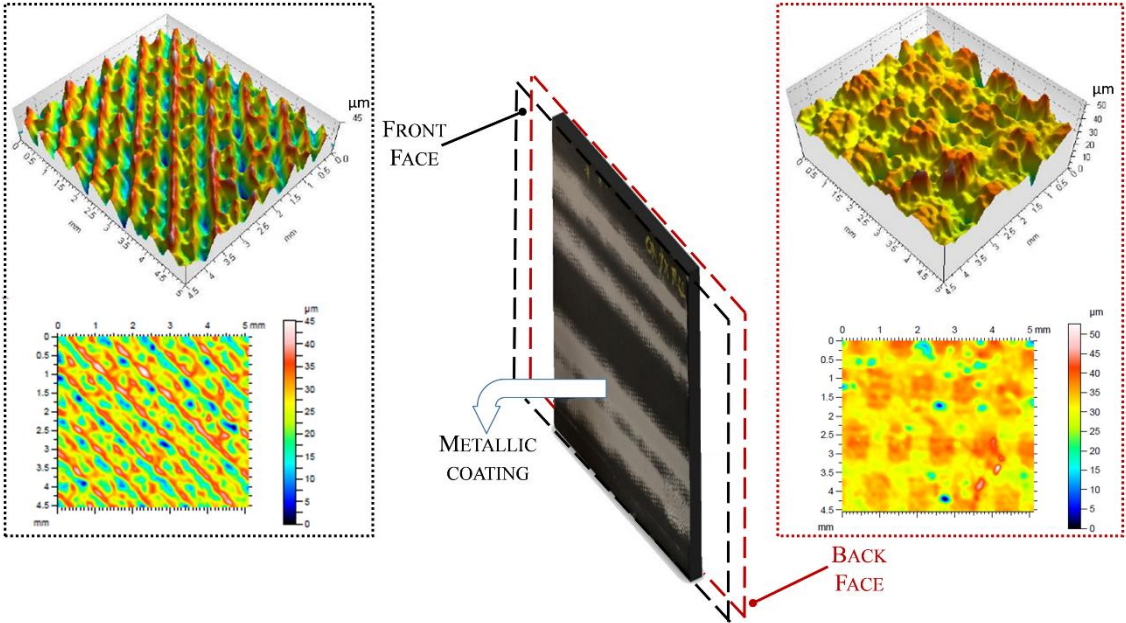


**Fig. 63** - Real picture of 3D-printed laminate (FO configuration) reporting the confocal microscope observations of both the front and the back faces of the panel.

The effect of the front face texturing of the polymer-based substrate on the cold spray deposition of metallic particles, such as aluminium powder, has been furtherly studied by SEM cross-section

observations. In particular, it is possible to note from Fig. 64 that the particles are entirely entangled within each valley tracked by two consecutive polymer tracks and this seems to guarantee an improved adhesion and a relatively high coating thickness and homogeneity. The polymer track valley was highlighted by the red dash-line in Fig. 64.

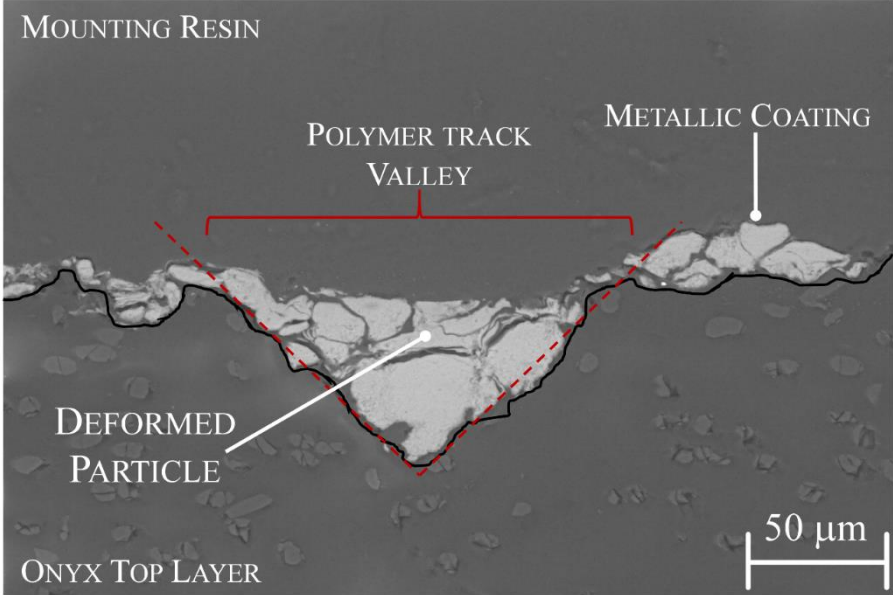


**Fig. 64** - Cross-section SEM image of a coated specimen. The particles are completely locked into the surface texture.

The macroscopical effects of these phenomena can also be pointed out by observing the top view images of the coated panels. In fact, it is possible to notice from Fig. 65 the presence of metallic bands, made of cold-sprayed aluminium particles, on the surface of the polymeric substrate; this is due to the capacity of the particles to deposit into the portions between two contiguous polymer-based filaments, evidencing the beneficial effect of the surface texturing.

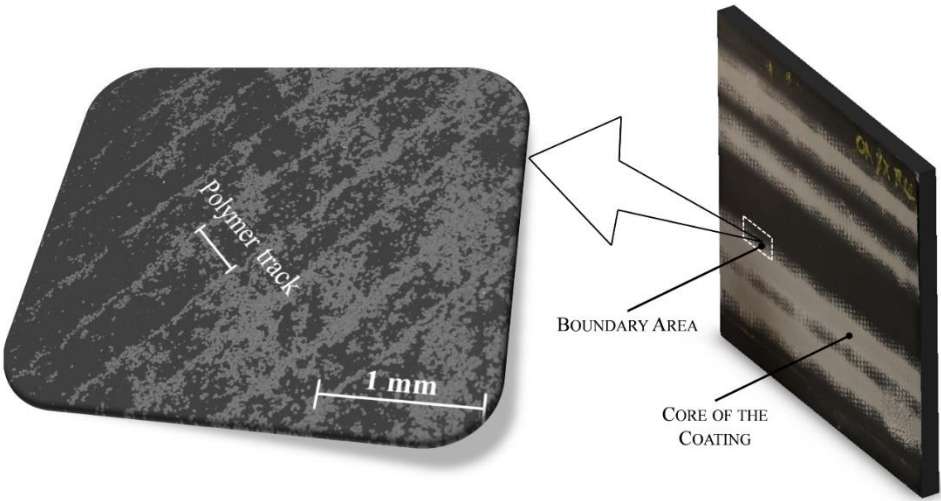


**Fig. 65** - Optical observations of the boundary portion of a coated specimen. The surface texturing is evident with the particles get entangled in the space between two contiguous polymer-based filaments.

After inspecting the impact of the surface texturing of the specimen on the deposition, namely on the bonding mechanisms involved, it was necessary to highlight the influence of the layup sequence and the strategy of panels' manufacturing. In order to do so, the first parameter the authors analyzed was the surface coverage, which is a good indicator of the number of particles effectively adhered to the substrate [60]. The results obtained for the three typologies of substrates, by varying the gas temperature of CS deposition, are shown in Fig. 66.

It is possible to notice that for all the layup sequences, a rise in the temperature leads to an increment of the surface coverage, reaching values also of about 90% in the coating core.

Regardless of the temperature values analyzed, it is also possible to notice from Fig. 66 that the best performances in terms of surface coverage are guaranteed by the LFC panels (with the layup sequence "matrix-matrix-reinforcement"). This result is also confirmed by SEM observations showing the surface coverage, made of aluminium particles, for each substrate typology (Fig. 67). It can be seen from Fig. 67b that for the LFC layup sequence, the coating appears denser and more compact than the others with excellent metallic coverage and few voids inside. However, with an increase in the gas temperature, the differences in terms of surface coverage among the three layup sequences tend to smooth out. In fact, it is possible to notice from Fig. 66 that the percentage increment of the surface coverage for LFC panels, for FO and HFC laminates, remains in the relatively small range of 2.5% when the temperature of the impinging gas is 400 °C, and it seems to be greater than 9% for lower values of the gas temperature, such as 250 °C. The main result is that the effects of the panels' manufacturing strategy tend to be less important with the increase in the gas temperature values. The coating height analysis furtherly confirms the results obtained for the surface coverage. In particular, it is possible to observe from Fig. 68 that for LFC and HFC panels, an increase in the gas temperature causes an increase in the coating thickness.

Regarding the FO panels, in contrast to what was observed for the other two configurations substrates, there is no appreciable trend of the coating height with the increase in the gas temperature. That means that for every gas temperature value under investigation, the adhesion mechanism involved for this configuration is not influenced more by the cold spray process parameters effectively (such as the gas temperature); the effects of the panel manufacturing process and layup seem to have a noticeable influence. In fact, for unreinforced FO panels, it was found that the coating profile follows the morphology of the composite panel surface, meaning that the particles penetrating within the substrate did not firmly anchor with the surrounding surface and did not promote the coating growth.

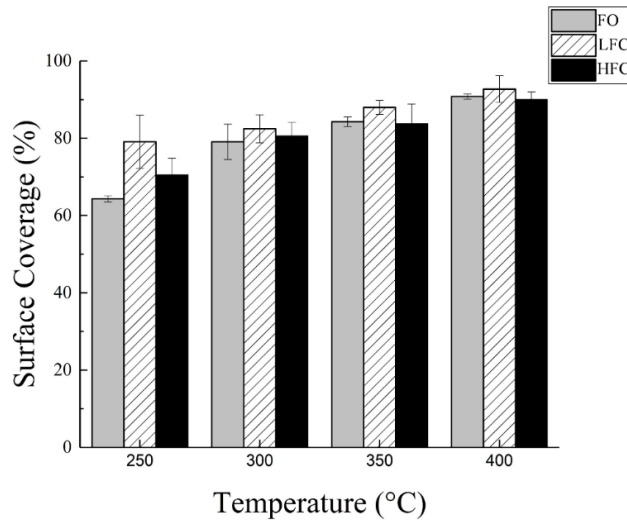


**Fig.66** - Surface coverage for different substrates and temperatures.

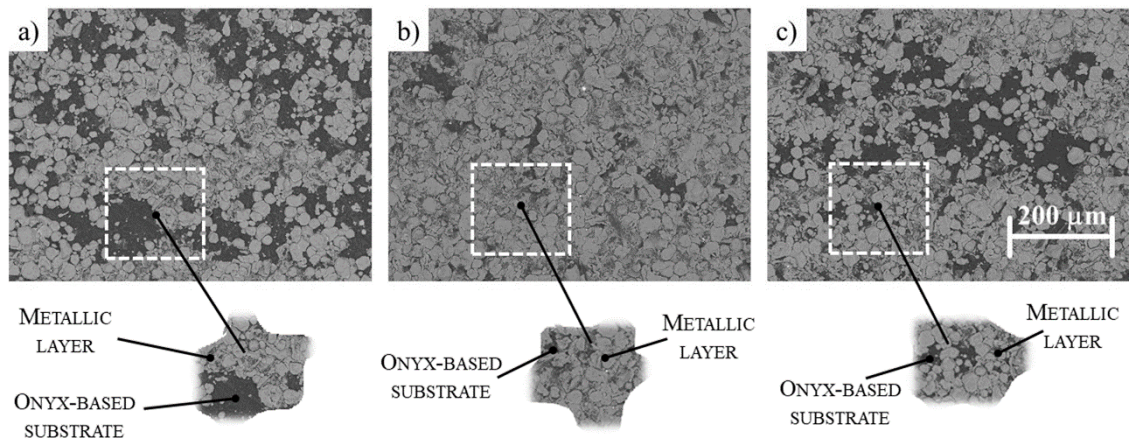


**Fig. 67** - SEM images of the surface of the coatings for the three layup sequences a) FO, b) LFC and c) HFC, respectively. The temperature was set at 250°C.

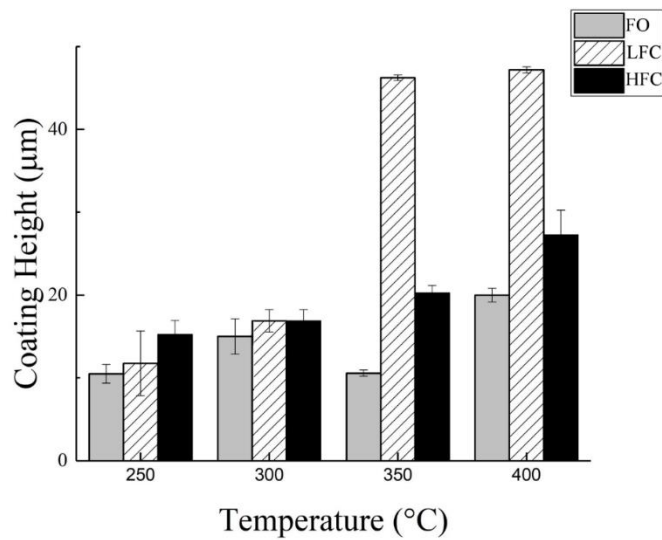


**Fig. 68** - Coating height evaluation for different deposition temperature values on different composite layup sequences.

### *4.1.2 Effects of panels characteristics and process parameters*

#### *4.1.2.1 Effects of the surface texturing*

The texturing of the substrate can have a noticeable influence on CS deposition and the face in contact with the construction plate during the 3D-printing process was proved to be characterized by a smoothed roughness that does not promote the sticking of the sprayed particles with the impacted surface. Such a result occurring because the powders that impact the space among the grid lines do not feel the presence of the grid itself. Therefore, it seems to be necessary that the valleys of the texturing had a comparable dimension to the feedstock powder diameter; this is a key factor for the particle interlocking between the substrate and the powders as the latter may impinge into the valleys becoming entangled. The superficial texturing characteristics are related to the deposition process of the contiguous Onyx filaments and can be changed by setting the 3D-printing process parameters. The front face texturing, in this case, promotes the bonding mechanisms and the interlocking phenomena between the first layer and the substrate with the particles that are well entangled within each valley. That means that is very difficult for the upcoming particles to remove them as they remain firmly anchored to the polymer surface, so as they can provide the right energy upon impact the metallic layer, deforming and flattening, so promoting the coating formation and grow-up.

#### *4.1.2.2 Effects of the panels' manufacturing strategy on CS deposition*

The results from Fig. 66 show an increase of the surface coverage values with the gas temperature, regardless of the panels' configuration. The reason is that a rise in gas temperature causes an increase in the mean velocity of the powders; that means that more particles can reach the right velocity to adhere to the substrate, regardless of the layup sequence of the panel. Moreover, an increase in the temperature of the carrier gas leads to the thermal softening of the powders that will deform more when impact the target surface leading to a wider contact area with the substrate and so to better deposition and coverage. Furthermore, the substrate will soften too due to the relatively hotter gas impinging on it: in particular, the softening effect favours the embedding of the particles that firmly anchor with the polymer-based surface. The best performances of the surface coverage were found for LFC panels, for each value of the investigated gas temperature. This beneficial characteristic may be explained as the LFC panel, compared to the FO panel, is charged with fibre layers, in agreement with the sequence "matrix-matrix-reinforcement"; as proved in literature [42], the presence of the fibres within the laminate causes the particles to deform more upon impact, as they collide on a more rigid substrate [125]. A more pronounced deformation of the particles leads to a wider contact area between the particle and the substrates

and better bonding. As a consequence, the upcoming particles do not cause erosion and detaching of the first particles deposited that are firmly anchored to the target surface. For this reason, it can be asserted that the deposition window of the fibre-reinforced polymers (like LFC panels) tends to be lower and narrower compared to the pure polymer (like FO panels made of Onyx matrix only): in fact, the particles colliding on a rigid substrate, due to the reinforcement inside, will tend to deform more causing adhesion even for relatively lower velocities. Hence, for a given impact velocity, more particles possess the right velocity to adhere to the substrate for the reinforced LFC panels, so resulting in greater surface coverage values.

As regards the HFC panels, characterized by a higher volume percentage of fibres, it is possible to observe an improvement in terms of surface coverage compared to the full Onyx panel (FO), for the same reasons highlighted above for LFC panels. However, it is possible to notice that the surface coverage of this typology of panels is lower than LFC panels, which are characterized by a lower volume percentage of fibres interspersed with portions of matrix material. The layup sequence of HFC panels causes them to be more rigid than LFC panels. For these reasons, the superficial portion of the matrix cannot deform adequately upon impact, as the fibres constrain its deformation. It is worth noting that four layers of matrix characterize each typology of 3D-printed panels only on the top surface. For LFC panels this constraining effect is partially eased by the presence of matrix material layers under every layer of reinforcement (remind the sequence “matrix-matrix-reinforcement”), supporting the deformation of the fibres and allowing for the surface matrix layer to deform more.

It is worth noting that the abovementioned considerations remain valid for each temperature value of the carrier gas. However, when the relatively hotter gas carrying the particles impinges the reinforced substrate, the thermal softening effects of the material become more important so that the constraining phenomena produced by the fibres are released without noticeable stiffening effects for the polymeric substrate. At relatively higher temperatures of the gas, the softened polymer matrix can flow more freely and deform upon impact [145]. The result is that the powders, under these gas conditions, impact a less rigid surface because the contribution of the fibres to the stiffening of the panels is less prominent and does not produce severe deformation of the particles resulting in a lower increment of the metallic coverage compared to the unreinforced panels.

As a result of these considerations, it can be asserted that the presence of the fibres has a beneficial effect on particle adhesion. However, a limit fibre content/fibre-layer thickness value exists, upon which the beneficial effect of the reinforcement is nullified and an overall lowering of the properties in terms of adhered particles is observed.

The results obtained from the surface coverage analyses were also confirmed by the coating height graphs (namely, with the increase of the gas temperature, more particles can reach the right velocity to adhere and the thermal softening effects become successfully for deposition [146]). However, the difference in trend observed for FO panels is related to the increased penetration of the particles within the unreinforced polymeric matrix that is more evident in the FO panels, being the substrate less rigid than the reinforced LFC and HFC panels. As proved by the relatively low values of the surface coverage from the analysis above discussed, for FO panels the particles seem to not fully adhere to the substrate and are carried off from the impinging particles hindering the coating growth. This phenomenon takes place also at relatively higher temperature values of the carrier gas as the particles further penetrate the softened target surface. That is the reason for which the coating height is the lowest for FO panels.

Moreover, for FO laminates, the relatively soft surface seems to not cause severe deformation of the impacting powders, so resulting in a poor adhered metallic layer tending to be removed from the upcoming particles [127]. It follows that, for this kind of sample, the coating grow-up is very difficult and the coating was proved to track the morphology of the panel surface with visible peaks and valleys of the coating profile. Hence, the coating height is strongly affected by the morphology of the substrate, which in turn depends on the manufacturing strategy adopted. In fact, it was proved that this phenomenon seems to be not so prominent for the reinforced panels (for both LFC and HFC laminates) that show an appreciable coating profile highlighting the ability of the particles to form a thicker metallic coating.

## **4.2 Onyx substrate (different matrix infill)**

### *4.2.1 Characteristics of the panel substrate*

#### 4.2.1.1 Substrate Morphology

As described in the previous paragraphs, one, two or three superficial matrix layers, with a 45 degrees pattern (100% fill Onyx filament), were produced on the outermost surfaces of the panels aiming to analyse the effects of the superficial layer thickness on CS deposition.

It is possible to observe from the confocal microscopies in Fig.69, which shows the surface morphology of the uncoated pure Onyx samples, that if a single layer of matrix with 45 degrees pattern is printed on the surface, the underlying triangle pattern is well visible. If more layers are printed on the surface, the triangle pattern tends to disappear, as shown in the Figure. It is possible to observe the same behaviour for the reinforced panels, not here portrayed for the sake of brevity. This would result in a different behaviour of the particles impacting the target surface, as the

particles impinge different surface morphologies, influencing the cold spray deposition. The particles deposition, in fact, would be affected by the layer thickness as well as the surface pattern.

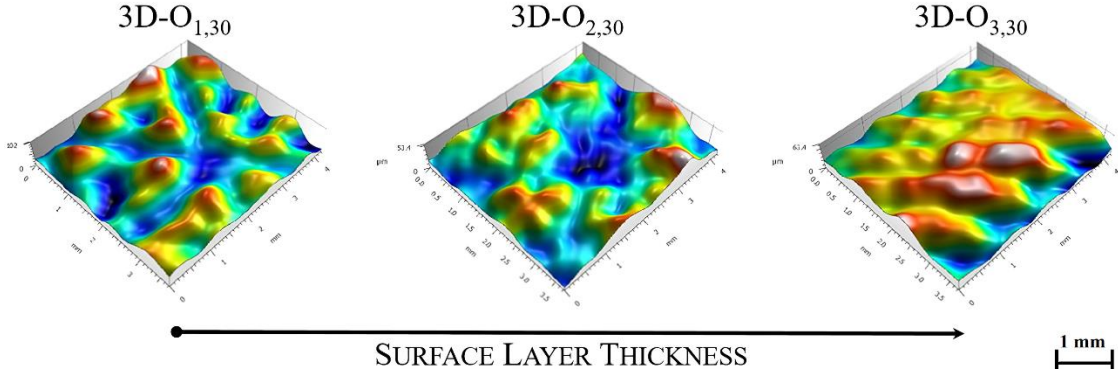


**Fig. 69** - Confocal acquisitions of the top-surface of the uncoated pure Onyx samples

For the sake of brevity, the surface morphology of pure Onyx panels with one layer of matrix only on the outermost surfaces, is shown in Fig. 70. From the Figure, it is evident the triangular pattern resulted from the manufacturing strategy of the panel. In particular, the coloured blue zones indicate the filling pattern with the Al particles that seem to be entirely impacted within each valley tracked by two consecutive polymer tracks, as also proved in literature [147]. It can be seen that the dimensions of the highlighted triangular structures tend to be smaller with the increase of the infill density (in particular moving from 30% to 50%), with a reduced space between two consecutive valleys.

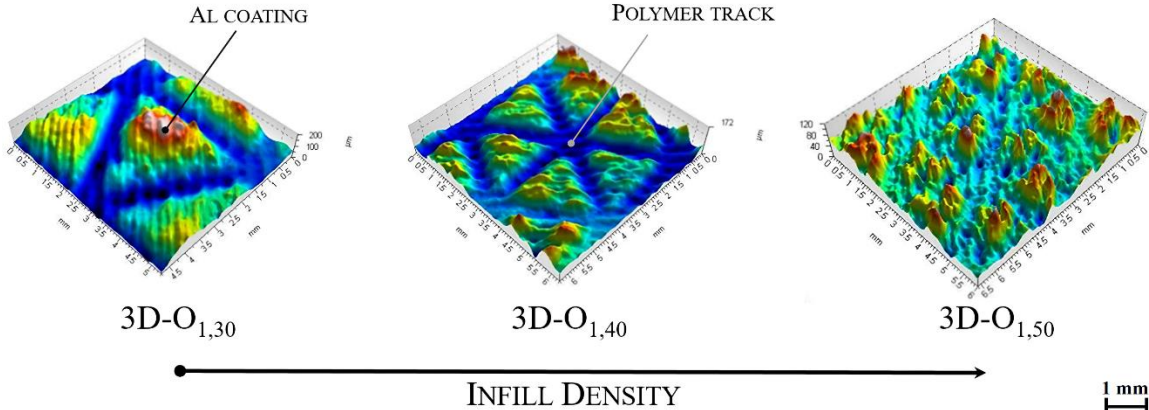


**Fig. 70** - Confocal acquisitions of the top surface of the coated pure Onyx samples highlighting the infill density

The height parameters were evaluated from the confocal analyses; the results obtained are reported in Fig. 71.

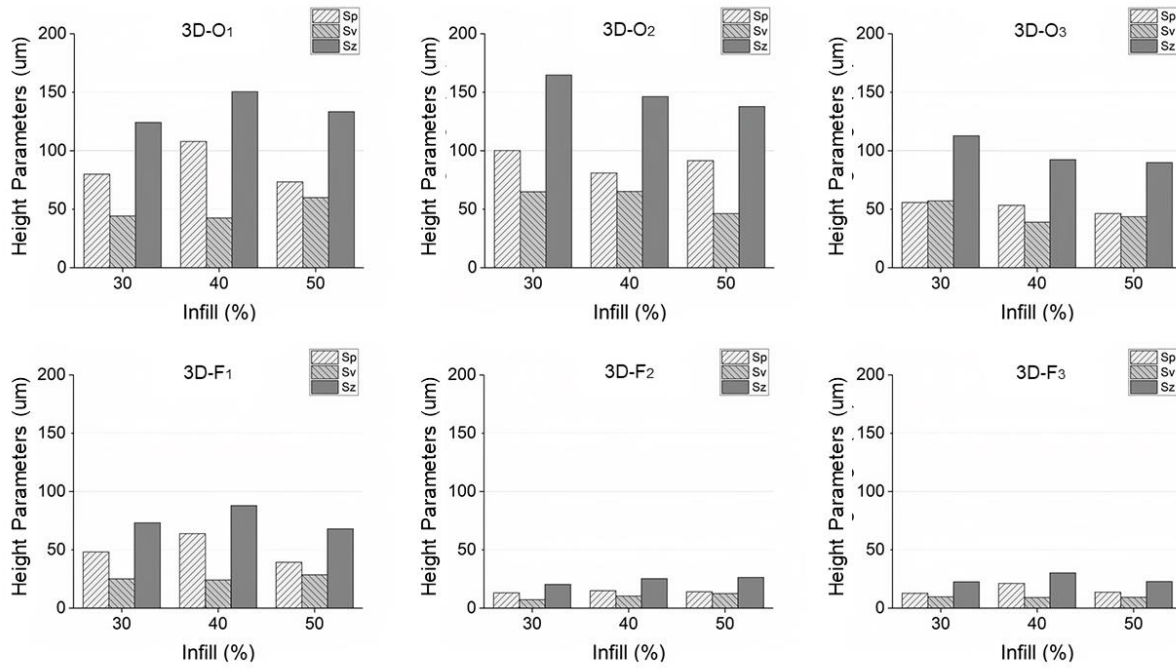
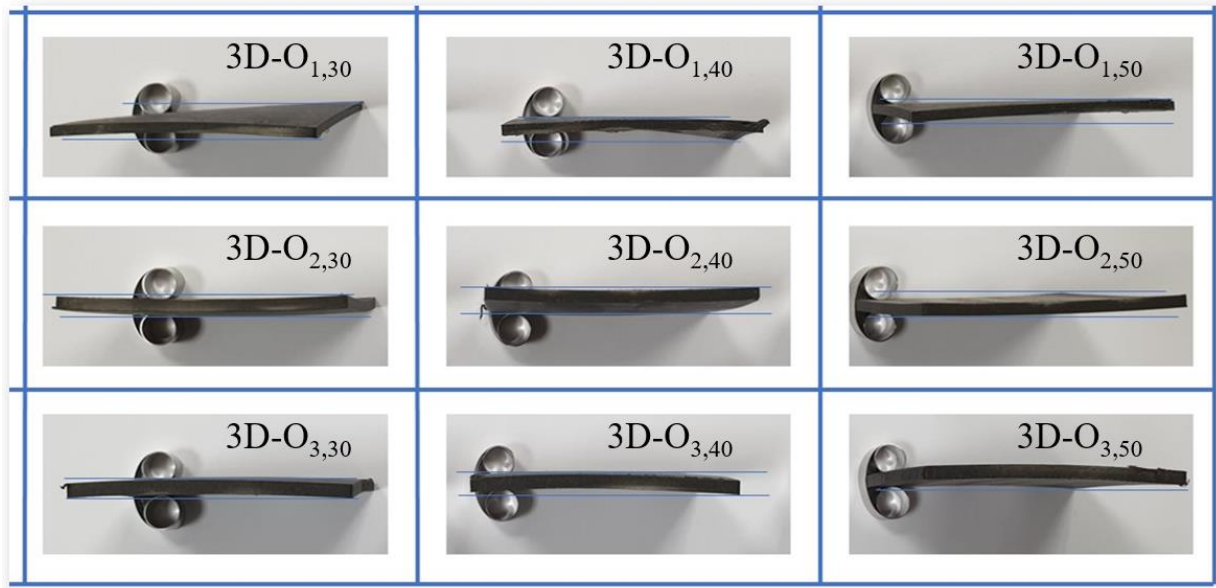


**Fig. 71** - Height parameters from confocal analyses

It can be observed from the Figure that the height parameters of the fibre reinforced panels are lower than those of pure Onyx samples, regardless of the infill density and the surface thickness considered. That means the coating height (i.e.  $S_z$ ) of the 3D-F panels is higher than that of 3D-O samples. These results suggest the higher deformation of the particles impacting the reinforced/stiffer substrates.

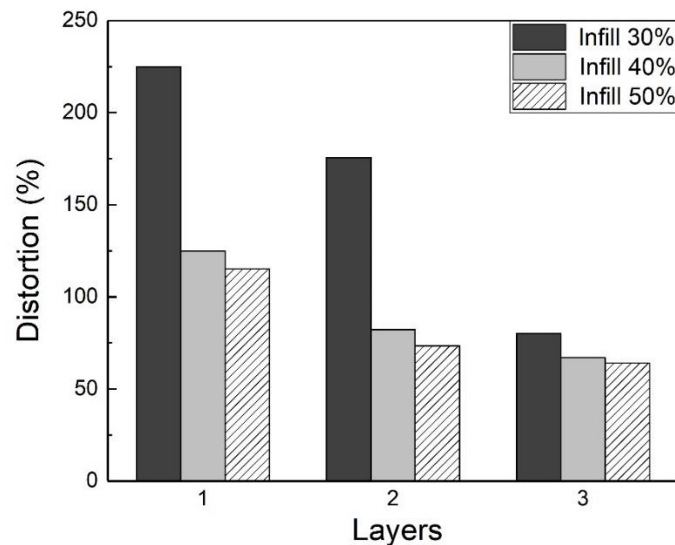
#### 4.2.1.2 Substrate distortion

Fig. 72 shows the pure Onyx panels profiles after the cold spray deposition of Al powder. All the samples exhibit both concave and convex distortion caused by cold sprayed deposits. This substrate distortion was not observed for carbon reinforced onyx panels and therefore these samples are not considered for this type of analysis. This mismatch between these two types of substrates may be attributed to the lower stiffening of the Onyx panels, which undergo higher thermal deflection upon the deposition.



**Fig. 72** - Pure Onyx panels profiles after the cold spray deposition of AlSi10Mg powder

The results of the substrate distortion calculated through Eq. 1 are reported in Fig. 73.



**Fig. 73** - Results of the substrate distortion of pure Onyx panels calculated through Eq. 1

Generally, the results vary with both the matrix infill and the external substrate layers. In detail, as the number of superficial layers increases from one to three, the distortion decreases from a maximum of 225% to a minimum of 65%. At the same time, as the matrix infill increases from 30% to 50%, a decrease in the substrate distortion is observed. Besides, it is evident that the substrate distortion is maximum (up to 225%) in the case of 30% infill and one superficial matrix layer and minimum in the case of 50% infill and three superficial matrix layers. Anyway, it is

interesting to note that the effect of the matrix infill percentage tends to flatten when increasing the number of external layers: substrates with one superficial matrix layer showed a wide range of distortion (115-225%) with respect to the different matrix infill, while substrates with three external layers showed a substrate distortion in the same range (60-70 %), with no significant dependence on matrix infill. From these results, it is possible to point out that the superficial matrix thickness plays a leading role in the substrate distortion (i.e. substrate stiffening) while the effect of the matrix infill tends to be reduced increasing the number of external layers.

#### *4.2.2 Characteristics of the coatings*

The SEM top-view micrographs of the coated surfaces are portrayed in Fig. 74 in order to appreciate the deformation of the particles and analyse the effects of the fibres reinforcing the polymer, the infill density and the superficial layer thickness on the surface coverage of the samples.

It can be observed an overall good coverage for all the specimens analysed, characterised by the presence of few voids among the particles. The coatings obtained on fibre reinforced specimens appear more homogeneous due to the increased deformation of the particles, caused by the stiffening effect of the fibres. This can be furtherly highlighted by analysing the particles splat size results, as shown in Fig. 75.

It can be noticed that the mean splat size is slightly higher for the fibre reinforced panels due to the higher stiffness of the reinforced panels that promote the deformation of the particles. This is also confirmed by the splat size distribution analysis. As an example, Fig. 76 shows a comparison between 3D-O<sub>2,30</sub> and 3D-F<sub>2,30</sub> panels: it is possible to observe that the size distribution is more homogeneous for the fibre reinforced panels as more particles are deformed and a higher percentage of bigger particles is present and cover the substrate surface.

The results of the adhesion strength tests are shown in Fig. 77. By observing these Figures, the cold sprayed coatings on pure Onyx samples show a greater adhesion strength (up to 5.8 MPa) compared to the ones on carbon reinforced Onyx (up to 4.2 MPa). These values are in the same range reported previously for metallic coatings/polymeric substrates [127].

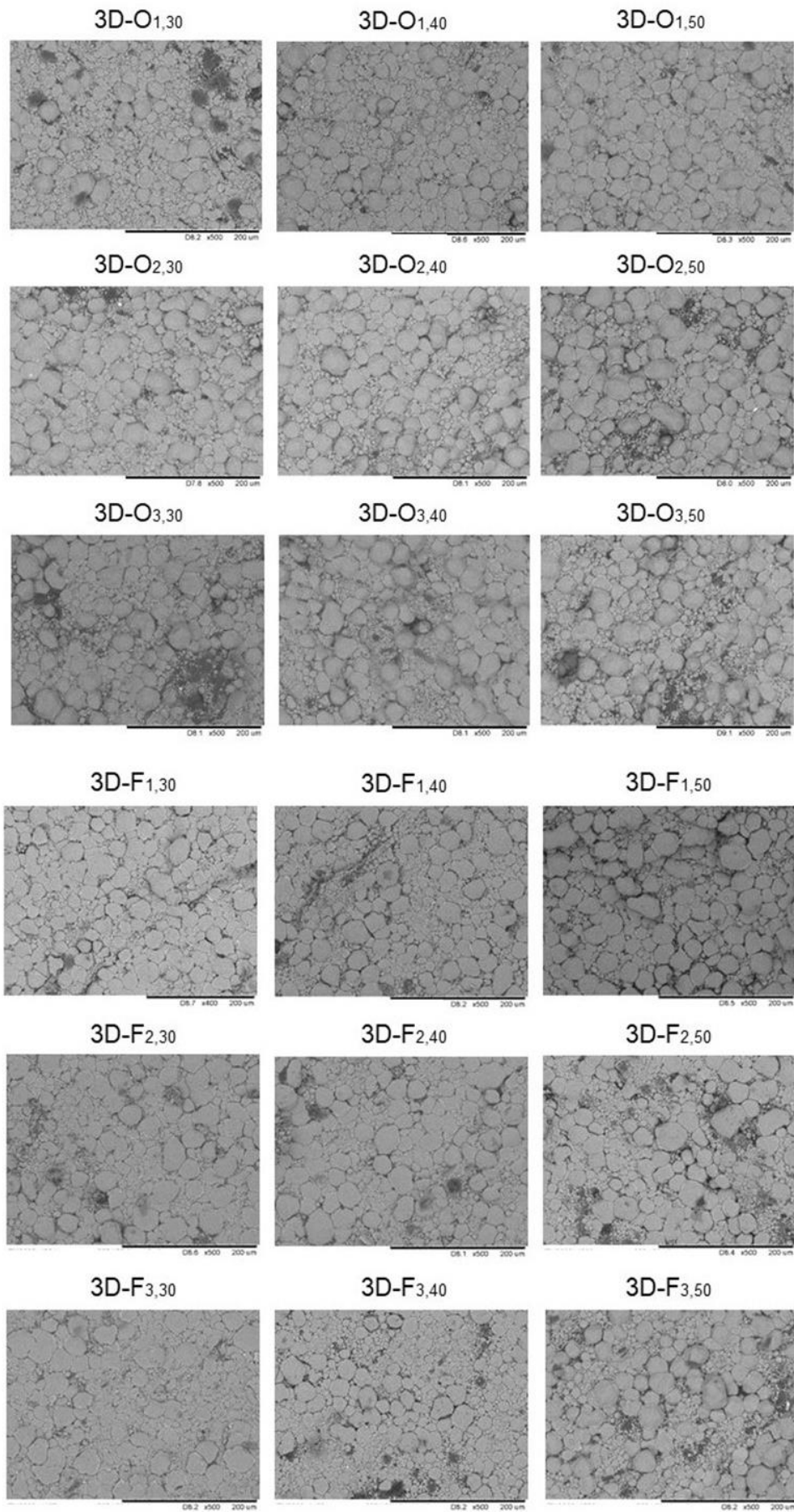


**Fig. 74** - SEM top-view micrographs of the coated surfaces

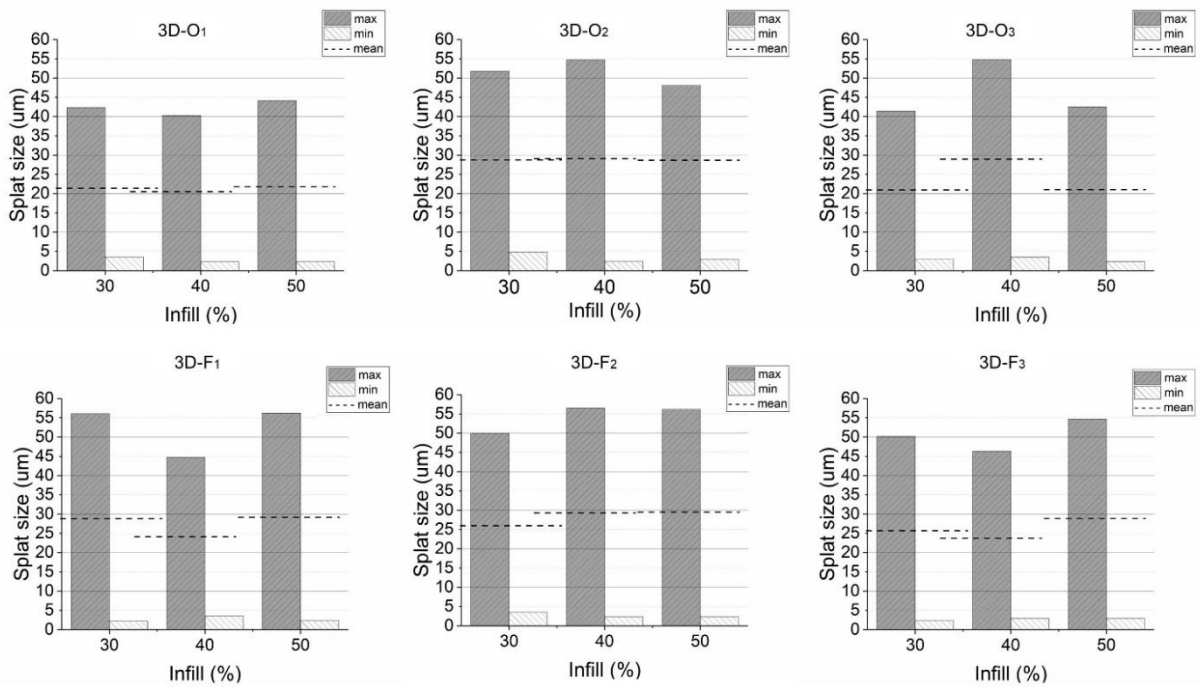


**Fig. 75** - Particles splot size from SEM images. The dotted lines evidence the mean splot size

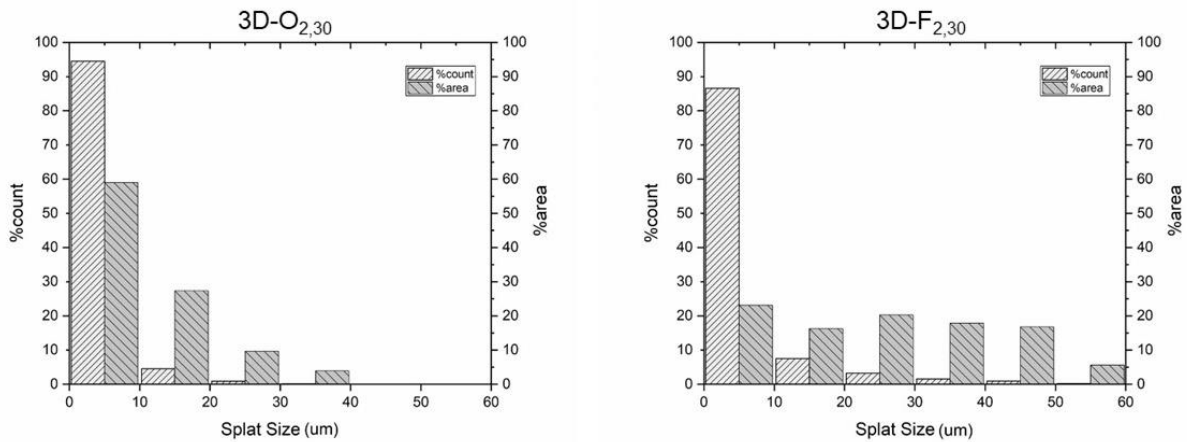


**Fig. 76** - Splot size distribution analysis for 3D-O<sub>2,30</sub> e 3D-F<sub>2,30</sub> samples

As seen in Fig. 77a, for coatings on pure Onyx panels, the adhesion strength varies from a minimum of 3 MPa to a maximum of 5.8 MPa. When increasing the matrix infill at a fixed number of superficial layers, the coating adhesion increases. However, as also observed for the substrate distortion, the scatter among the three panels (30%, 40% and 50%), in terms of adhesion strength values, tends to be reduced when increasing the number of the superficial matrix layers.

On the other hand, as seen in Fig. 77b, in the case of carbon reinforced onyx substrates, the variation of the adhesion strength is less pronounced and results in the range from 2.6 to 4.2 MPa.

Also in this case, at a fixed number of superficial layers, the adhesion generally increases when increasing the matrix infill.

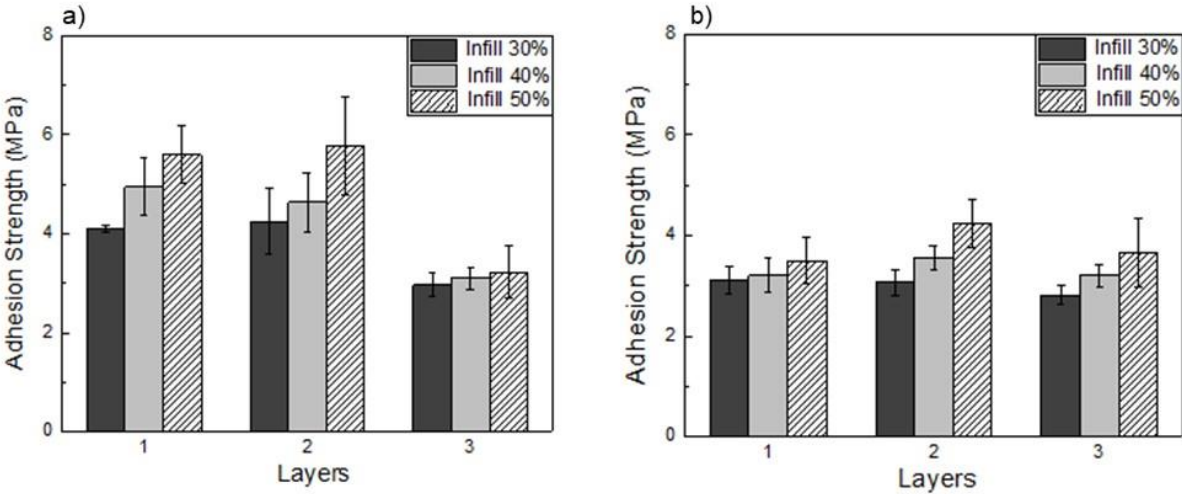


**Fig. 77** - Results of the adhesion strength tests for both pure Onyx (a) and reinforced (b) samples

To assess the effectiveness of the adhesion tests, residual coating particles adhered on the dolly surface have been investigated through optical analysis. In particular, three different morphologies of the fracture surface were found: (1) AlSi10Mg coating, (2) Onyx substrate and (3) glue or other impurities. The measure of the area fractions of the dolly that are interested by the coating, or the substrate or other impurities were calculated by SEM images. For the sake of brevity, only the results obtained for pure Onyx samples are reported in Fig. 78.

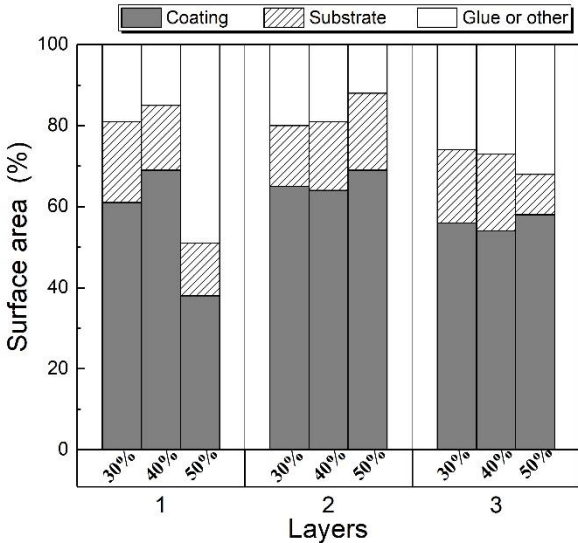


**Fig. 78** - Area fractions of the dolly surface for the pure Onyx samples

The results presented in Fig. 78 prove that the surfaces of the dollies after the test are covered for over 60% by Al coating. These results suggest that the bonding between Onyx substrate and Al coating is weaker than the bonding between the glue and the coating, thus the test was properly carried out.

### *4.2.3 Effects of panels characteristics and process parameters*

#### *4.2.3.1 Effect of fibres*

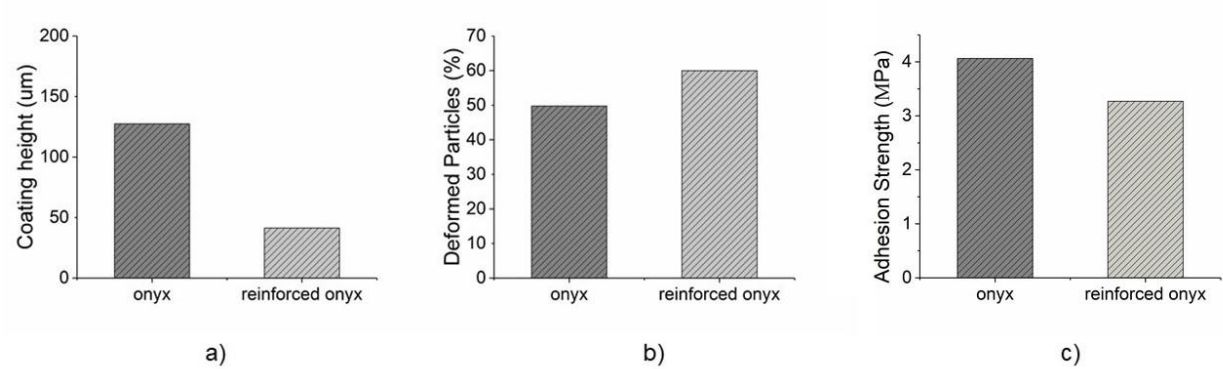
The results portrayed in the previous paragraphs have been processed in order to highlight and discuss the influence of fibres reinforcing the Onyx panels on the cold spray deposition process, as shown in Fig. 79. Fig. 79a illustrates the comparison, in terms of mean coating height, between the pure Onyx and reinforced panels. As shown in the Figure, the reinforced panels globally have a value of the coating height that is lower of about 70% compared to the unreinforced panels. The lowering of the coating height is usually due to two main phenomena occurring during the deposition: i) the deformation of the particles, ii) the penetration of the particles into the substrate [126].

Fig. 79b portrays the percentage of particle splats having a diameter higher than the mean diameter of the feedstock particles, so it represents the percentage of particles that experience deformation upon impact with the substrate. Looking at Fig. 79b, it is possible to notice that 60% of the particles sprayed on the reinforced substrate have undergone a severe deformation, while only 50% of the particles sprayed on the unreinforced substrates have reached a diameter higher than the mean diameter of the processing powders. Consequently, it is possible to assert that the coating produced on the reinforced panels is more deformed. As proved in literature [148], this is due to the stiffening effect of the reinforcement. Moreover, it is possible to observe from the cross-section micrographs of the specimens in Fig. 80 (where 3D-F<sub>3,40</sub> and 3D-O<sub>3,40</sub> panels are considered as examples) that the coatings produced on the reinforced panels have a lower penetration depth (about 13 μm) compared to the coatings obtained on the unreinforced panels (about 25 μm), due to constraining effect of the fibres.

This suggests that the prevailing phenomenon causing the lowering of the coating height on the reinforced panels is the plastic deformation of the particles caused by the stiffening effect of the fibres.

By looking at the results illustrated in Fig. 79c, it is possible to notice that the coating produced on the reinforced panels results less adhered with the substrate, compared to the coating produced on the unreinforced panels. This result highlights that the higher deformation of the coating

produced on the reinforced panels does not determine a higher adhesion, contrary to what was observed for metallic coatings on metallic substrates [149, 150]. For this reason, in order to obtain a higher adhesion, it would be necessary to promote a greater penetration of the particles into the substrates, while the deformation of the particles seems to be not so important for adhesion.



**Fig. 79** - Effect of the fibres on cold spray deposition. a) Mean coating height of pure Onyx and fibre reinforced panels; b) percentage of deformed particles due to deposition; c) adhesion strength values

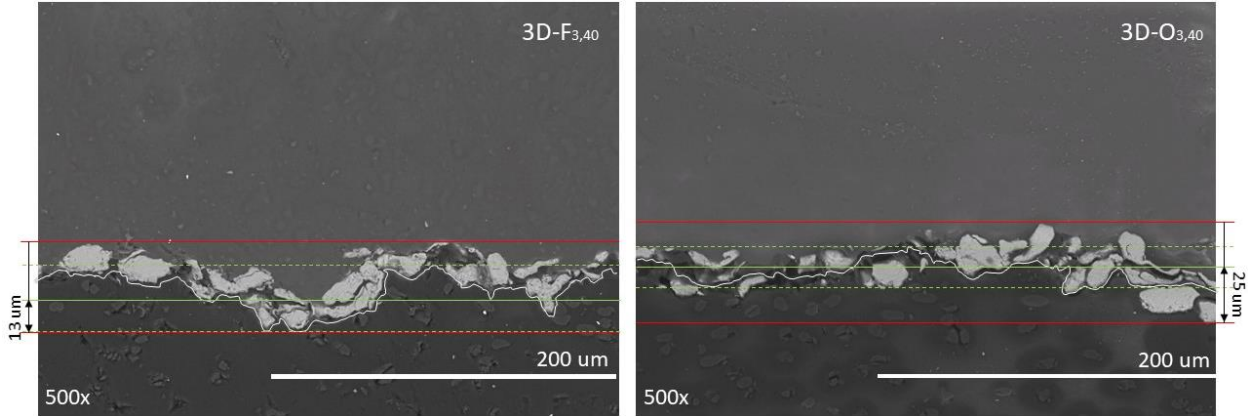


**Fig. 80** SEM images of 3D-F<sub>3,40</sub> and 3D-O<sub>3,40</sub> samples. The penetration depth is calculated as the distance of the deepest point reached by the coating from the substrate main plane

In conclusion, it is possible to assert that the presence of the fibres leads to more homogeneous coatings, but causes an overall worsening of the adhesion of the coating on the substrate.

4.2.3.2 Effect of the infill density

The influence of the infill density on the mechanisms ruling the adhesion of the metallic particles on the 3D-printed substrates is evidenced in the graphs in Fig. 81. From Fig. 81a it is possible to notice an overall lowering of the coating height when the infill percentage is increased moving from 30% to 50%. The lowering of the coating height can be ascribed to a higher deformation of the particles, as confirmed by Fig. 81b, where it is possible to notice that for an infill density of 30%, about 37% of the particles are deformed acquiring a diameter higher than the mean diameter of the feedstock particles, while for an infill density of the 50%, about the 65% of the particles are highly deformed. The higher deformation of the particles would seem to be determined by the stiffening of the panels when the infill density is increased. This is confirmed by the results obtained by measuring the substrate distortion presented in the previous paragraphs. In fact, the panels having an infill density of 30%, portray higher values of distortion than the panels that have infill densities of 40% and 50%, regardless of the number of onyx layers on the surface, evidencing an increasing stiffness of the panels when the infill density is increased. On the basis of the results obtained in the previous paragraph, it would be reasonable to expect that a better adhesion is obtained on the less stiff panels with the particles that should penetrate profoundly the substrate; however, looking at Fig. 81c it is possible to notice that increasing the infill density, the adhesion values increase as well. In fact, the stiffening effect caused by the increase of the infill density is not as relevant as the stiffening effect caused by the fibres, as proved by the fact the reinforced panels do not experience important distortion during the deposition process. The reason is that there is a further phenomenon that prevails over the stiffening effect in determining the adhesion values. As suggested by previous literature studies [147], the superficial texturing can have a remarkable influence on the adhesion mechanisms [143, 151]. Starting from a value of the infill density equal to 30% and moving toward 50%, there is a densification of the texturing that causes the entanglement of the particles between two consecutive polymer tracks.

For these reasons, the adhesion of the coating was proved to be stronger for the denser panels, as it is more difficult to remove the entangled particles from the substrate. The main result of this study is that by lowering the distance between the polymer tracks (namely increasing the infill density) it is possible to increase the adhesion between the metallic particles and the polymeric substrate: increasing the infill density from 30% to 50%, the adhesion strength increases up to 40%.

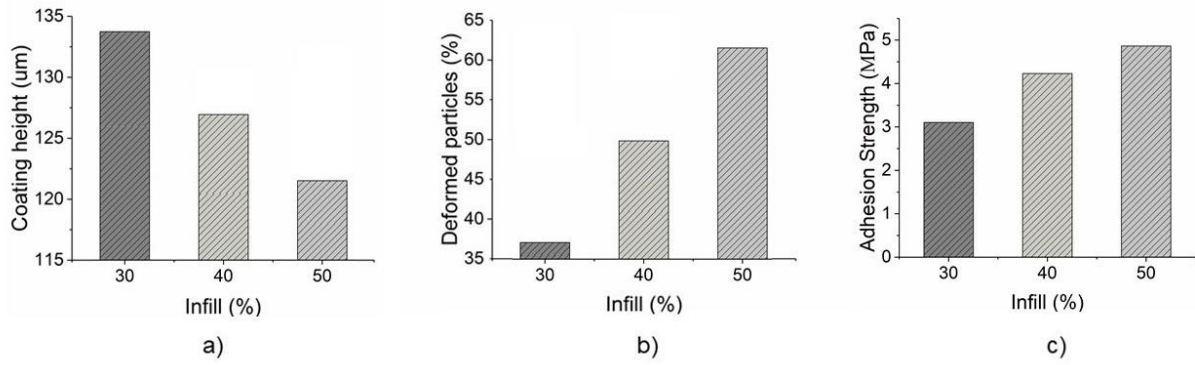


**Fig. 81** - Influence of the infill density on CS deposition. a) Mean coating height; b) percentage of deformed particles; c) adhesion strength values

#### 4.2.3.3 Effect of the superficial matrix layer thickness

It is possible to observe the influence of the superficial matrix layer thickness on the cold spray deposition process of metals-to-polymers, by looking at the results presented in Fig. 82.

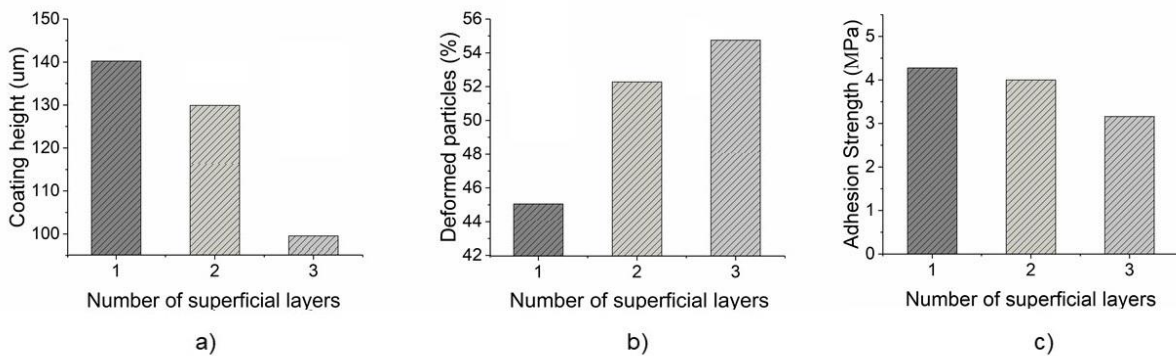


**Fig. 82** - Influence of the superficial matrix layer thickness. a) Mean coating height; b) percentage of deformed particles; c) adhesion strength values

Looking at Fig. 82a, it is possible to notice a decrease of the coating height when two layers of Onyx are deposited on the top surface of the panel; the same trend was observed when a further layer of matrix on the surface of the panel is added. This phenomenon is due to the deformation of the particles that tend to deform greatly with the increase of the number of the superficial layers, as shown in Fig. 82b. In fact, it is possible to observe that the percentage of deformed particles is about 45% for the panel with a single layer on the surface while, when two layers are deposited, 52% of the particles are deformed. Adding a third Onyx layer, the coating appears much more deformed as almost 55% of the splats have a higher diameter than the mean diameter of the processing powders. This behaviour is coherent with the trend of the coating height. The reason is

that the particles impact on a more rigid surface, as proved by the results above presented. In particular, it was found in the previous paragraphs that the superficial matrix thickness plays a leading role in the substrate distortion, i.e. in the substrate stiffening, as the panels with three external layers showed a reduced substrate distortion. As for adhesion strength values, by looking Fig. 82c, it can be seen that by adding two layers on the top surface of the panel, the adhesion reduces compared to the case when a single layer is deposited on the surface. Moreover, by adding a further layer on the surface, a further worsening of the adhesion behaviour can be observed. The reasons are to be found in the stiffness of the panels that tend to increase with the number of superficial layers. In fact, the particles that impact on a softer substrate (like the panels with a single layer of matrix on the surface) can penetrate greatly the polymer surface anchoring with the surrounding polymeric material [43, 93], so resulting in higher values of adhesion strength. In summary, increasing the superficial matrix layer thickness it is possible to produce more homogenous metallic coatings (made by more deformed particles) but characterised by a lower adhesion with the polymeric substrate: increasing the number of superficial layers from 1 to 3, the adhesion strength reduces up to 25%.

## **CHAPTER 5 – Model development**

### **5.1 Introduction to the model**

A cornerstone in developing the cold spray deposition has been to understand the adhesion mechanism between the powders and the substrate and between the first layer of particles and the subsequent impinging particles [152]. To reveal these mechanisms different theories were proposed in literature such as interfacial restructuring [153] or amorphization [154], mechanical interlocking [155, 156], oxide-layer break-up [157] and adiabatic shear instability [152, 158] and several numerical models were also developed aiming to explain and interpret these intriguing adhesion phenomena described in various works by Assadi et al., [152] and other research groups. Some points are still under debate, for instance, the adiabatic shear instability, which was the most accredited adhesion mechanism for CS, also confirmed by Champagne [159], with Lagrangian finite element simulations, was proved to be not essential for coating formation from the last activities carried out by Hassani-Gangaraj et al., [156]. The question “which is the most prevailing adhesion mechanism?” still stands to date and several research groups are proposing their lesson. This thesis also aims to provide an interpretation of the complex phenomena occurring when metallic particles are impinged onto polymer-based substrates through cold spray, trying to unveil the physical mechanisms ruling the adhesion of metal particles on polymers. To this aim, an

interpretative model for the impact of a single metallic particle on a polymeric substrate will be proposed and then validated with the experimental results. The basic idea is that adhesion mechanisms are not mutually exclusive and, therefore, more than one phenomenon may take place during particle/substrate interaction. It is also assumed that all the mechanisms involved must require a certain amount of energy to take place. Therefore, an energetic approach is proposed in this work based on the evidence that the kinetic energy, once the particle has adhered to the substrate, is completely converted into other energy forms. It is also evident that, after the impact, several phenomena take place and the energy required for the adhesion is, therefore, equal to the total energy required for those phenomena to occur. In conceiving this model, the authors identified some energy activated phenomena that are likely to occur in cold spray, so the model is conceived as an equilibrium equation between the available energy and the energy requested to activate the hypothesized phenomena. A representative scheme describing the energy conversions hypothesized to occur during the deposition is presented in Fig. 83. To summarize, the model has been conceived on the phenomena that it is believed to occur during the deposition and rule the deposition itself (as reported in Fig. 83). The energy was chosen as interpretation key on the assumption that the above-hypothesized phenomena are energy activated, and two main questions have been posed: i) how much energy is required to activate these phenomena? ii) where does the kinetic energy of the particles go after the adhesion occurs? In the authors' opinion, if we can answer these two questions, we are able to understand which are the involved phenomena. Moving one step ahead we could dare to suggest a theory: if the kinetic energy dissipated by the particles and the energy required to activate all the hypothesized phenomena are of the same order of magnitude, it is reasonable to be convicted that these are the ones responsible for the adhesion (adhesion that has been experimentally observed, let our recall). The proposed model was calibrated through a dedicated experimental campaign, by comparing the outcomes of the model with the experimental pieces of evidence, once again testing the hypothesis done on the benchmark of the real deposition. After that, some experimental outcomes reported in the literature were discussed in the light of the proposed model to assess its capability to describe the adhesion process. Summarizing it is aimed to answer several open issues: (i) which are the mechanisms/phenomena involved in the CS deposition on polymer-based materials; (ii) which is the role of the reinforcement when spraying on composites; (iii) which are the energy-related aspects in CS on composites.

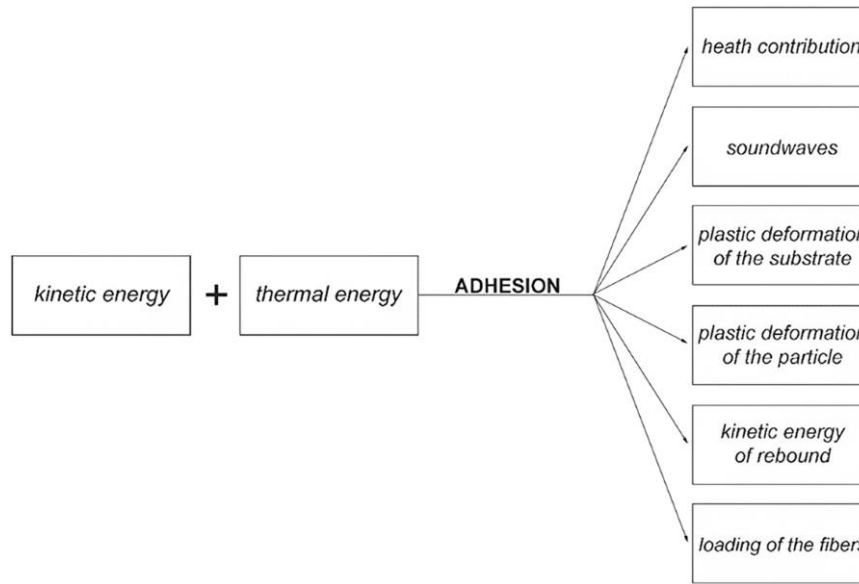


**Fig. 83** - Representative scheme describing the energy balance.

## 5.2 Model development

It is worth recalling that two different interactions can be observed in cold spraying: i) particle-to-particle interaction, which is responsible for the coating growth and ii) particle-to-substrate interaction which is responsible for the coating adhesion. In this thesis the attention will be focused on the latter interaction to shed light on the phenomena ruling the adhesion between the single particle and the target surface. Two different energies can be defined:

- $E_p$ , which is the amount of energy possessed by a single particle impacting the substrate and
- $E_a$ , which is the amount of energy required to activate the phenomena (as conjectured by the authors) leading to the adhesion of the particle.

### 5.2.1 Calculation of $E_p$

The amount of energy owned by a particle,  $E_p$ , can be summarized as in Equation (1).

$$E_p = E_k + E_g + E_i + E_T \quad (1)$$

It is possible to define the kinetic energy of the particle as (Equation (2)):

$$E_k = \frac{1}{2} m v^2 \quad (2)$$

Where “ $v$ ” is the velocity of the particle, one of the most relevant parameters in cold spray. The potential energy,  $E_g$  can be written as (Equation (3)):

$$E_g = mg(h - h_0) \quad (3)$$

$$E_p = \frac{1}{2} mv^2 + N \frac{f}{2} k_b T_p \quad (2)$$

The term “ $h-h_0$ ” in this case, corresponds to the stand-off distance which is usually low in cold spray [ref], so it can be assumed that the potential energy is negligible in the present study.

The internal energy,  $E_i$ , can also be neglected because can be considered a constant value before and after the adhesion of the particles onto the substrate, so as well as the potential energy does not contribute to the energy required for adhesion.

The average thermal energy,  $E_T$ , of a system composed of  $N$  molecules having  $f$  degrees of freedom is (Equation (4)) [160]:

$$E_T = N \frac{f}{2} k_b T_p \quad (4)$$

Therefore, Equation (1), neglecting the internal energy and the potential energy, can be written as in Equation (5).

$$E_p = \frac{1}{2} mv^2 + N \frac{f}{2} k_b T_p \quad (5)$$

### 5.2.2 Calculation of $E_a$

The main forms of energy in which the particle energy can be converted after the impact include: i) heat contribution; ii) soundwaves; iii) plastic deformation of the substrate; iv) plastic deformation of the particle; v) kinetic energy related to the rebound of the particle. Regarding composite materials, due to the presence of the fibres, a further contribution must be taken into account: vi) loading of the fibres. In the following sections, the abovementioned contributions are discussed individually.

#### (i) Heat transfer contribution

The particle transfers heat to the substrate by thermal conduction, by virtue of the temperature acquired during the process. It can be assumed that at the exit of the nozzle the particle reaches the same temperature of the carrier gas [161]. Once it has impacted the substrate, the particle exchanges the acquired heat with the substrate by thermal conduction. The thermal flow is given by law (Equation (6)):

$$q_c = H_C(T_p - T_s) \quad (6)$$

For a spherical particle exchanging heat with a lamina [161],  $H_C = \frac{4r}{\frac{1}{k_p} + \frac{1}{k_s}}$ .

The range of interest for the evaluation of the thermal exchange is the time the particle takes to adhere to the substrate, supposing to consider the particle adhered once it has reached its final position into the substrate, and therefore when its speed is zero. Neglecting the rebound effects, the time taken by the particle to adhere is  $t = \frac{2s}{v}$ . It was assumed that the motion of the particle through the substrate is uniformly decelerated since the space covered is so short that other types of dissipative effects can be neglected. Therefore, the heat exchanged in this time interval is portrayed in Equation (7).

$$E_t = \frac{H_C(T_p - T_s)2s}{v} \quad (7)$$

#### (ii) Soundwaves and elastic waves

During the elastic impact, if the velocity is small compared to elastic wave speeds, the quasi-static approach is justified, and the elastic waves can be neglected. As confirmed by KL Johnson, in Contact Mechanics [162], this is further validated when plastic deformation occurs. The plastic flow leads to the dissipation of part of the energy, as it diminishes the intensity of the contact pressure, hence reducing the energy converted into elastic wave motion.

#### (iii) Energy absorbed due to plastic deformation of the substrate

Up to moderate impact speeds (about  $500 \text{ m s}^{-1}$ ), the knowledge of inelastic impact under static condition, following Hertz's theories, was used to analyse the impact behaviour under a dynamic load. The decision to follow those theories is motivated by the energy absorption caused by the plastic flow. In order to analyse the energy absorbed in these conditions, the following assumptions have been made on the basis of the work of Johnson [162]: i) Yields are calculated with Tresca criterion for the sake of simplicity, as the results are not largely different compared to more complicated criteria ii) Work hardening has been neglected. This assumption is acceptable due to the material and the field of tension that arises: in fact, as the literature states, the resulting deformation of the particle has to be considered small, hence the material does not show an interesting amount of work hardening. iii) The impact of the particle is assumed to be normal to the substrate.

Under those conditions, assuming the fully plastic regime, the material does not pile-up or sink in along the edges of the impacting particle. Naming  $\delta_p$  and  $\delta_s$  respectively the displacement of the particle and displacement of the substrate along the direction of the normal to the substrate, and defining  $\delta = \delta_p + \delta_s$ , the penetration of the impacting particle can be written as  $\delta = a^2/2$ .

Being the deformation,  $d$ , small ( $d \ll a$ ), the strain is characterized by the ratio  $d/a$ , and its magnitude is proportional to the average contact pressure acting mutually on each solid, divided by the elastic modulus, as written in Equation (8).

$$\varepsilon_p + \varepsilon_s = \frac{p_m}{E_p} + \frac{p_m}{E_s} \propto \frac{d_p}{a} + \frac{d_s}{a} \quad (8)$$

The total deformation of the two bodies in the contact zone can be written as in Equation (9).

$$\frac{d_p}{a} + \frac{d_s}{a} = \frac{a}{2} \left( \frac{1}{R_p} + \frac{1}{R_s} \right) \quad (9)$$

Therefore, Equation (8) can be written as:

$$\frac{p_m}{E_p} + \frac{p_m}{E_s} \propto \frac{a}{2} \left( \frac{1}{R_p} + \frac{1}{R_s} \right) \Rightarrow p_m \propto \frac{a \left( \frac{1}{R_p} + \frac{1}{R_s} \right)}{\left( \frac{1}{E_p} + \frac{1}{E_s} \right)} \quad (10)$$

In the case of plastic deformation  $p_m = cY_s$ , where  $c$  is a parameter dependent on the indenter geometry (which is the particle in this case) and Johnson [162] estimates a value of about 3.0. When the pressure lies between  $Y_s$  and  $3Y_s$ , the plastic flow is contained by elastic material and it can only expand radially and thus this is called elastic-plastic regime.

The kinetic energy consumed for the elastic and plastic local deformation of the impacting bodies, up to the instant where the compression reaches its maximum value, can be written as in Equation (11).

$$\frac{1}{2} MV^2 = W = \int_0^{\delta^*} P d\delta \quad (11)$$

Where  $\frac{1}{M} = \frac{1}{m_s} + \frac{1}{m}$ .

In the case of a contact of a sphere with a substrate, the compressive load is  $P = \pi a^2 p_m$ .

Assuming that the impact between the bodies results in purely plastic deformation, the energy absorbed during deformation is portrayed in Equation (12).

$$E_{PLA(s)} = \frac{1}{2} MV^2 = \int_0^{a^*} \pi a^2 p_d \left(\frac{a}{R}\right) da = \pi a^{*4} p_d / 4R \quad (12)$$

It should be noticed that subscript  $d$  denotes the dynamic quantities. The quantity  $\pi a^{*4} / 4R$  is the apparent volume of material displaced by the particle. It can be assumed that  $p_d$  is approximately equal to  $p_m$  being in the fully plastic regime, and its value is then  $p_m = p_d = 3Y_s$

#### (iv) Kinetic energy related to the rebound of the particle

This quantity, which is not a material property but depends upon the severity of the impact, can be neglected as a significant amount of energy is dissipated in the form of plastic deformation such that as the speed at initial impact increases, the coefficient of restitution decreases [163]. Moreover, under the hypothesis of achieving adhesion between the particle and the substrate, the rebound can be considered absent.

#### (v) Energy absorption on account of the plastic deformation of the particle

The energy absorbed for the deformation of the particle was evaluated considering the ideal deformation firstly described by Dieter and Bacon [164]. Upon impact, the particle deforms, taking up an elliptical configuration, as shown in Fig. 84, due to the contact pressure. Assuming that the particle impact direction is perpendicular to the substrate, its radius in the impact direction contracts, becoming the semi-minor axis of the ellipse. The work required to deform the particle is expressed in Equation (13).

$$dL = \frac{3}{4} \left[ -Y_P V_s \frac{dr}{r} \right] \Leftrightarrow \quad (13)$$

$$\Leftrightarrow E_{PLA(p)} = -\frac{3}{4} \cdot Y_P \cdot V_s \cdot \ln \frac{r_1}{r} = \frac{3}{4} \cdot Y_P \cdot V_s \cdot \ln \frac{r}{r_1}$$

#### (vi) Loading of the fibres

A theoretical model to evaluate the energy absorbed by a polymer composite during ballistic impact was proposed by Morye et al. [165]. Given the velocities considered and the compatibility of the hypothesis, it was assumed in this research work that this model could be considered valid in the framework of cold spray. The following hypotheses have been made in the development of

the model: i) the impacting body is rigid and does not deform during the impact. The tests performed have demonstrated that the projectiles have preserved their mass and form upon impact; ii) The delamination causes a negligible absorption of energy; iii) The composite failure mechanism over the thickness is uniform. High-speed photography has subsequently confirmed this assumption; iv) The loss of energy spent to overcome the friction between the composite and the impacting body is insignificant and the subsequent heat production is negligible.

The model assumes that there are three main contributions to energy absorption: i) energy absorbed to promote the break of the strained fibres that have reached the tensile failure upon impact,  $E_{TF}$ . ii) Energy absorbed to deform the fibres that the impinging body have not impacted directly,  $E_{ED}$ . The propagation of transverse waves after the impact of the projectile, causes the yarns to deform and the formation of a cone in the rear surface of the composite. iii) The kinetic energy absorbed by the amount of the substrate that is put into motion by the projectile,  $E_{KE}$ . The total energy can be therefore written as in Equation (14).

$$E_{Total} = E_{TF} + E_{ED} + E_{KE} \quad (14)$$

In cold spray, particles inside the deposition window, should not break the fibres, either put into motion a portion of the composite, due to their small dimension compared to the substrate. Therefore, the contribution of  $E_{KE}$  and  $E_{TF}$  can be considered negligible.

As for  $E_{ED}$ , it can be seen from Fig.85 a schematic deformation of yarn upon the impact, where the radius of the abovementioned cone formed in the rear surface of the substrate is  $R_c$ .

The energy absorption during deformation can be evaluated by integrating the portion of the stress/strain curve of the composite at a given strain (namely,  $\varepsilon$ ). Being this curve approximately linear for a composite material, it is possible to assert that (Equation (15)):

$$E_{ED} = \frac{1}{2} E_s \varepsilon_s^2 \quad (15)$$

Depending on the impact point, not all the yarns deform in the same manner: the yarns closer to the impact point experience a strain close to their failure strain, while the farther ones possibly do not strain at all. It can be then asserted that the strain of the composite  $\varepsilon_s$  can vary from a value  $\varepsilon_0$ , equal to the failure strain of the composite, at the impact point, to a value of  $\varepsilon_s=0$  at the distance,  $R_c$ , where the yarn is undeformed. It is possible to express the variation of strain with Equation (16).

$$\varepsilon = \frac{2(R_c - r)}{2R_c - 2r} \varepsilon_0 \quad (16)$$

and thus, calculate the energy absorbed during deformation as Equation (17):

$$E_{ED} = \frac{1}{2} E \varepsilon^2 = T \int_{\frac{D}{2}}^R \frac{1}{2} E 2\pi r dr 4 \left( \frac{R_c - r}{2R_c - D} \right)^2 \varepsilon_0^2 \quad (17)$$

$$E_{ED} = E_{load} = \frac{\pi E_s \varepsilon_0^2 T}{(2R_c - 2r)^2} \left[ \frac{R_c^4}{3} - \frac{(2r)^2 R_c^2}{2} + \frac{r^3 R_c}{3} - \frac{r^4}{16} \right]$$

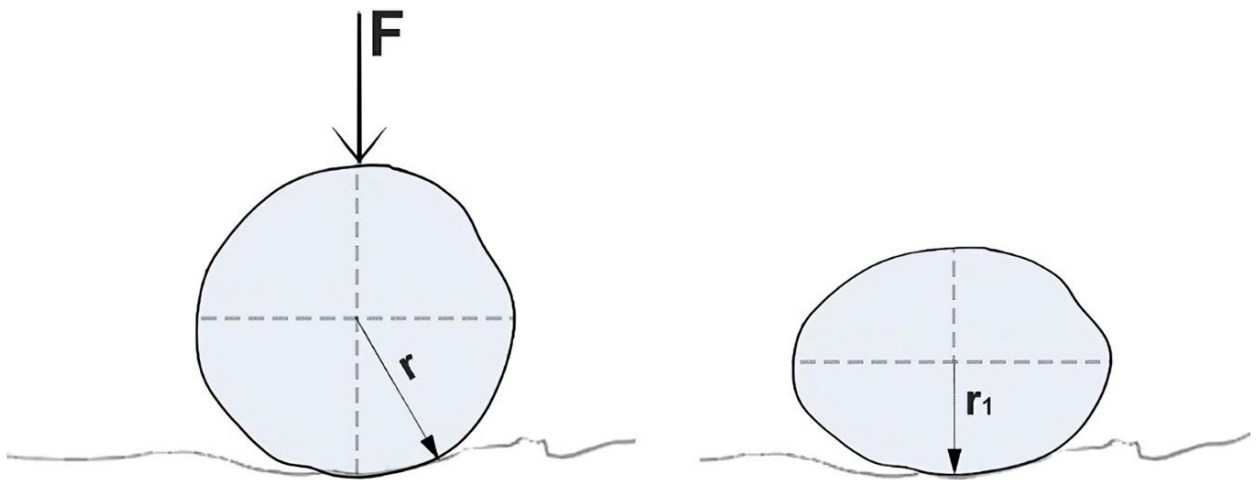


**Fig. 84** - Deformation of a single particle upon impact.  $F$  is the compressive force applied to the particle

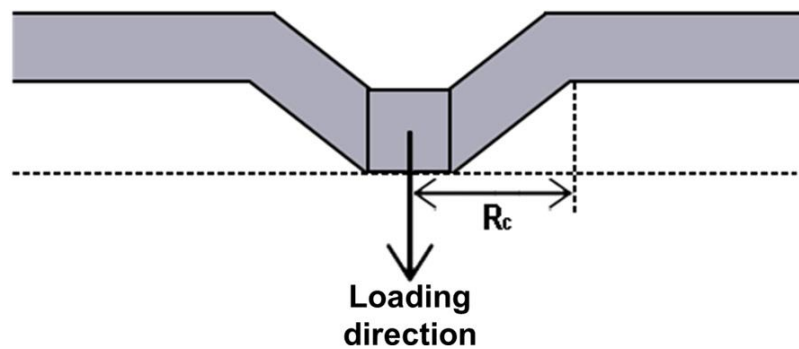


**Fig. 85** - Schematic side view of a fibre in a composite deformed during a ballistic impact

### 5.2.3 Model formulation

Neglecting soundwaves and elastic rebound, the main energy contributions, shown schematically in Fig. 86, are: i) Heat contribution; ii) Plastic deformation of the substrate; iii) Plastic deformation of the particle; iv) Loading of the fibres.

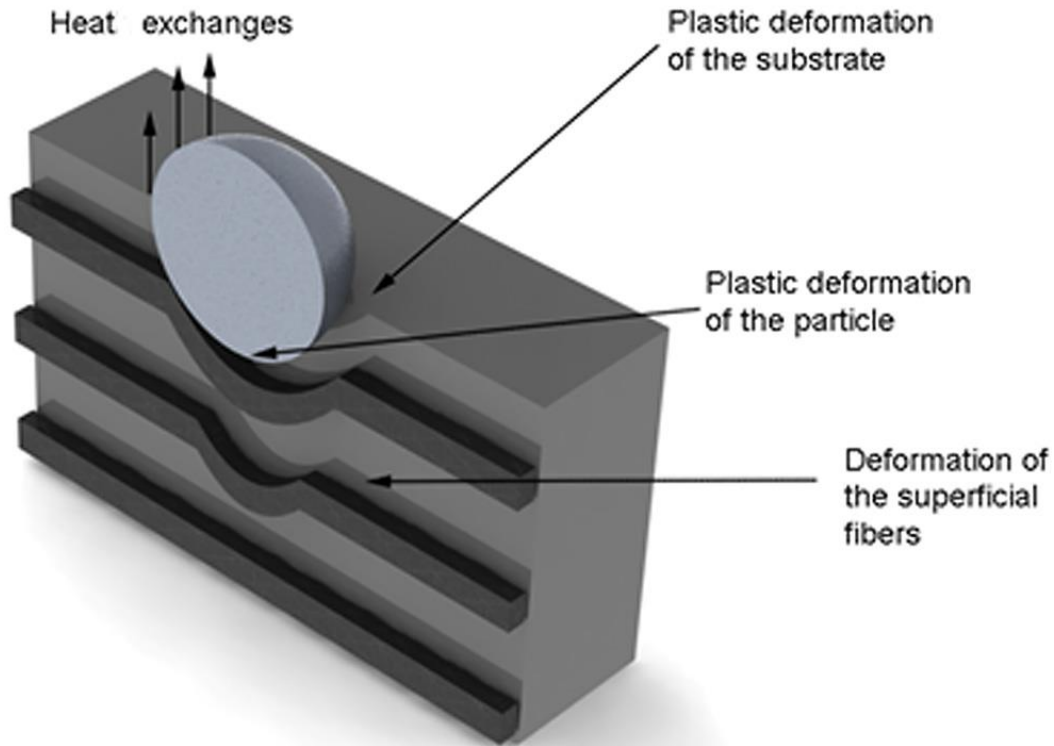


**Fig. 86** - Schematic description of the main energy contribution to the bonding in CS process

The assumptions on which this model is based can be here summarised:

- i) the energy spent to overcome the frictional force between the particle and the substrate is considered negligible;
- ii) the failure mechanism of the substrate is uniform along the thickness direction;
- iii) delamination causes a negligible absorption of energy;
- iv) a quasi-static approach has been chosen to describe the deformation of the surface;
- v) Yields calculated with Tresca criterion;
- vi) work hardening has been neglected.

At this point a first formulation of the model can be released in equation (18), which describes the transformation of kinetic and internal energy of the system to other energy contributions, is reported below:

$$\frac{1}{2}mv^2 + N\frac{f}{2}K_B T_p = \frac{H_c(T_p - T_s)2s}{v} + \left(\frac{\pi a^{*4}3Y_s}{4R}\right) + \left(\frac{3}{4} \cdot Y_P \cdot V_s \cdot \ln \frac{r_0}{r_1}\right) + \frac{\pi E_s \varepsilon_0^2 T}{(2R_C - r)^2} \left[ \frac{R_C^4}{3} - \frac{(2r)^2 R_C^2}{2} + \frac{r^3 R_C}{3} - \frac{r^4}{16} \right] \quad (18)$$

In this formulation an issue arises: the contributions of particle deformation, substrate deformation and fibre loading are overestimated (as they have a mutual influence) and a distribution of the available energy ( $E_p$ ) among these three contributions depending on the material properties is not considered. All of these three contributions have a mutual influence which is dependent on the materials under investigation. For example, if steel powders are sprayed on a soft polymer it can be argued that the particle deformation will be almost zero while the polymer will experience a high deformation [166], while if softer aluminium particles are sprayed on a high-performance polymer (PEEK for instance) a deformation of both particles and substrate is expected and observed [124]; being the  $E_p$  constant it can be assumed that higher is the deformation of the substrate lower must be the deformation of the particle. On these premises it is clear that a coefficient, accounting for the distribution of deformation between particle and substrate and depending on the material properties must be included. The coefficients  $A$ ,  $B$  and  $C$ , as defined in Equation (19), are therefore included in the model.

$$A + B + C = 1$$

$$\frac{A+C}{B} = \frac{E_{pow}}{E_s} \quad (19)$$

$$\frac{A}{C} = \frac{E_f}{E_m}$$

The final formulation of the model is as follows (Equation (20)):

$$\frac{1}{2}mv^2 + N\frac{f}{2}K_B T_p = \frac{H_c(T_p - T_s)2s}{v} + A\left(\frac{\pi a^{*4}p_d}{4R}\right) + B\left(\frac{3}{4} \cdot Y_P \cdot V_s \cdot \ln \frac{r_0}{r_1}\right) + C\frac{\pi E_s \varepsilon_0^2 T}{(2R_C - D)^2} \left[ \frac{R_C^4}{3} - \frac{D^2 R_C^2}{2} + \frac{D^3 R_C}{3} - \frac{D^4}{16} \right] \quad (20)$$

### 5.3 Materials and methods for experimental validation

The theoretical model proposed through the *Vi-Pe-R-A* equation has been validated considering two different experimental cases: i) deposition of aluminum particles on unreinforced polymeric substrates and ii) deposition of aluminum particles on fiber reinforced polymers (FRP). For this

purpose, sheets of polypropylene (PP) with a thickness of 0.25 mm were chosen for both the polymer-based substrates. Carbon fiber fabrics with an areal density of 220 g/m<sup>2</sup> were used as reinforcement for the composite material. The compression molding technique under a pressure of 1.1 MPa at 210 °C for 15 min was used for the manufacturing of both the panels' typologies. The curing temperature was set in accordance with the melting temperature of the polymer. The mold was cooled down in air, while the pressure was kept constant. The laminates so manufactured presented a thickness of approximately 2.5 mm. The choice of using these materials is due to the relatively high amount of material data available to the authors. Micron-sized AlSi10Mg aluminum powders, provided by LPW South Europe and with a particle mean diameter of 30 μm and a spherical shape, were cold sprayed through a low-pressure equipment (DYCOMET). Air was used as carrier gas. The inlet gas pressure and the SoD were set to 6 bar and 25 mm, respectively, and kept constant during all the depositions. Different tests were carried out by varying the gas inlet temperature, from 150 °C to 550 °C, to obtain different particles impact velocities, which increase as the gas temperature increases. A k-type thermocouple was used to measure the gas temperature at the exit of the nozzle with the probe aligned with the axis nozzle. This allowed for identifying three different deposition ranges: i) a range of low impact velocity for which the particles do not have enough energy to adhere, with the resulting rebounding phenomenon; ii) a range of higher impact velocity where some particles start to adhere, and the deposition efficiency starts to increase; iii) a range of a further higher impact velocity with the particles that are well anchored to the substrates to form the coating. The streamwise jet velocity for a given gas temperature was measured by means of an hot-wire anemometer (Dantec Dynamics, MiniCTA, Skovlunde, Denmark), equipped with a 5 μm diameter, 1.25 mm long wire probe, and placed at the exit of the nozzle. Its output signal was acquired by the same data-acquisition system used to generate the electric signal, with a sampling rate of 10 kHz, for 2000 operating cycles. An estimation of the experimental uncertainty of the hot-wire data has been made following Yavuzkurt's work [46]. The uncertainty in the phase-averaged streamwise velocity is found to be <3 % for all the measured values. It is worth noting that for these measurements, the particles were not injected into the nozzle so avoiding that the powders would cause damages to the anemometer probe. In one-dimensional numerical models about particle acceleration by the high-speed gas, the particle velocity can be calculated by a drag force on a single particle in a fluid flow. In particular, Alkhimov et al. [47] obtained an empirical equation which includes the particle velocity, the gas velocity and the gas pressure. That means once the gas velocity was characterized, the resulting particle velocity at the exit of the nozzle can be calculated through the equation suggested in the literature [48] and reported in Eq. (21). Here,  $v$  is the particle velocity,  $P0$  is the

air supply pressure at the entrance of the nozzle,  $\rho p$  is the particle density,  $r$  is the particle radius and  $x$  is the axial position of the particle within the nozzle. The reliability of the proposed equation to make an effective prediction of particle velocity at the nozzle outlet under the investigated CS conditions was proved in the literature [47].

$$v = \frac{v_g}{1 + 0.85 \sqrt{\frac{2r}{g}} \sqrt{\frac{\rho p v_g^2}{P_0}}} \quad (21)$$

The adhesive strength of the particles after cold spray deposition was measured following the ASTM D4541 standard and by using a PosiTest ATM. Aluminum dolly with a 10 mm diameter was bonded on the top surface of the cold sprayed deposits using cyanoacrylate glue, as shown in Fig. 87. Any excess adhesive or coating surrounding the dolly was removed with a drill bit. Based on both the visual inspections and the results from the adhesive tests, three average values of the particles impact velocity for each deposition range above discussed were identified. The mean adhesion values, measured from 3 specimens coated employing the same deposition parameters, are illustrated in Fig.88. It is possible to observe that no adhesion occurred for the lowest impact velocities (100 m/s and 225 m/s for unreinforced and reinforced panels, respectively); moreover, the adhesion values measured on reinforced panels are slightly lower than the values obtained for the unreinforced specimens considering the same experimental conditions, in agreement with the literature results [49,50]. In summary, the experimental validation of the model was carried out following this procedure: firstly, the particle velocity value calculated from Eq. (21) was implemented into the *Vi-Pe-R-A* equation, then, the difference between the first member of the equation, representing the energy possessed by the particle before the impact, and the second one, which is the energy that the particle requires to adhere to the substrate, was calculated. Three possible cases were found: i) the difference is negative meaning that no adhesion should occur; ii) the first member equals the second one or it is a little above meaning that adhesion is expected; iii) the difference is positive meaning that the particle should have the proper energy to anchor with the substrate. Nevertheless, it is important to notice that the model relies on simplifying hypotheses and several dissipation phenomena are neglected; for this reason, the energy required for adhesion should be slightly higher than the quantity defined through  $E_a$  in the *Vi-Pe-R-A* equation. We will consider the model validated if it will be able to produce sufficiently converged results compared with the experimental deposition outcomes. The main parameters required for the implementation of the model have been collected from the data sheets of the materials employed in the experimental tests and from literature, where necessary. It is worth to notice that several parameters required some experimental measurements and calculations based on

commonly known material mechanics theories or isentropic flow models, which are not shown here for the sake of brevity.

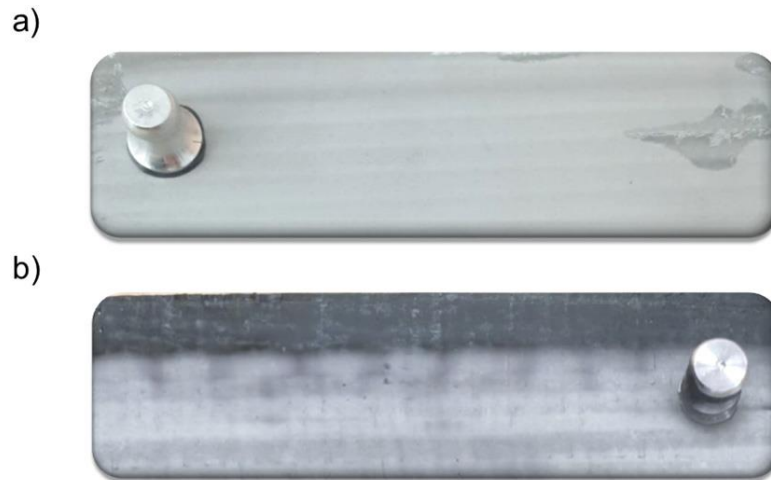


**Fig. 87** - Positioning of aluminum dolly for adhesion test on a) unreinforced substrate b) reinforced substrate.

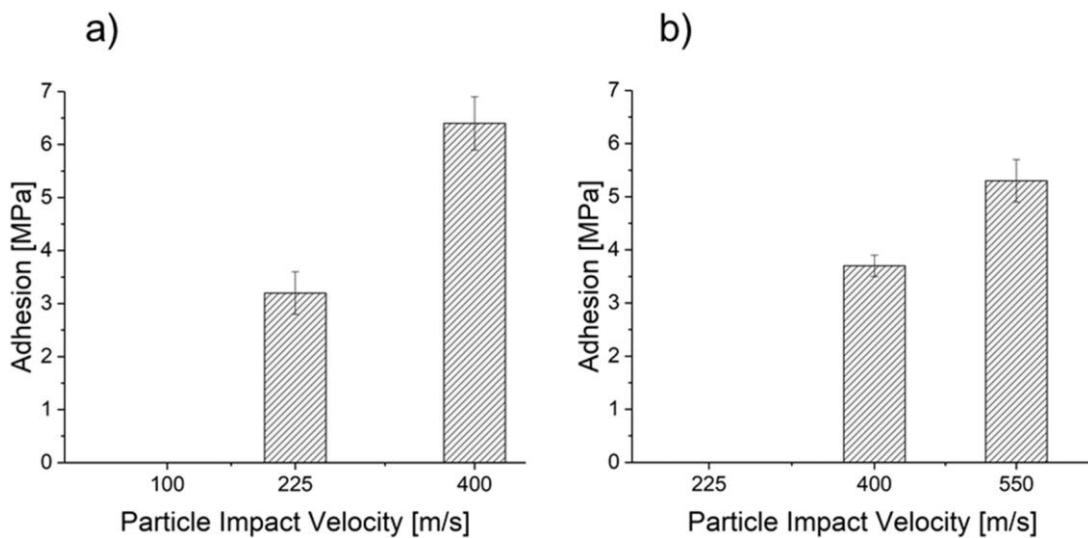


**Fig. 88** - Adhesion tests results for a) unreinforced substrates b) reinforced substrates.

It was also assumed that: i) the substrate is at room temperature due to the relatively short time of deposition and ii) the particle reaches the same temperature of the carrier gas at the exit of the nozzle [51,52], so its properties have been evaluated at the gas temperature. All the involved parameters are reported in Table 6.

**Table 6** - Main parameters required for the implementation of the model.

Material parameters for polymer	Polypropylene	
Melting temperature ( $T_f$ ) [°C]	180	
Elastic modulus at 20 °C ( $E_s$ ) [GPa]	1.63	
Yield strength at 20 °C ( $Y_s$ ) [MPa]	30	
Thermal conductivity ( $K_m$ ) [W/mK]	0.11	
<i>Composite fiber main parameters</i>	Carbon Fiber	
Elastic modulus ( $E_f$ ) [GPa]	200	
Yield strength ( $Y_f$ ) at 20 °C [MPa]	900	
Volume fraction in the composite [%]	50	
Thermal conductivity ( $K_f$ ) [W/mK]	40	
<i>Composite panel main characteristics</i>	FRP	
Number of layers	15	
Matrix surface thickness [mm]	0.25	
Radius of the contact surface between the substrate and the particle (experimentally)	Polymer	FRP
$a$ [mm]	0.025 ±	0.020 ±
	0.01	0.01
Aluminum powder's main parameters		
Density, $\rho_p$ [kg/m <sup>3</sup> ]	2700	–
Elastic modulus ( $E_{pow}$ ) [GPa]	70	–
Yield strength ( $Y_p$ ) at 20 °C [MPa]	290	–
Particle mass, $m$ [Kg]	$3.8 \cdot 10^{-11}$	–
Particle mean radius, $r$ [μm]	15	–
Particle semi-minor axis (after impact), $r_l$ [μm]	10	6
Thermal conductivity ( $K_p$ ) [W/mK]	273	–

## 5.4 Results

### 5.4.1 Model validation

The results given from the model proposed in the *Vi-Pe-R-A* equation for the pure polymeric substrates are reported in Table 7, in terms of difference between  $Ep$  (which is the amount of energy possessed by a single particle impacting the substrate) and  $Ea$  (which is the amount of energy required to activate the phenomena leading to the adhesion of the particle).

**Table 7** - Experimental vs. theoretical results for cold spray deposition of aluminum particles on unreinforced polymeric substrates.

Particle impact velocity [m/s]	Overall behaviour	Adhesion [MPa]	$E_p$ [J]	$E_a$ [J]	$\Delta E$ [J]
$v_1=100$	No deposition	n.a	$4.5741 \cdot 10^{-7}$	$6.5511 \cdot 10^{-7}$	$-6.5511 \cdot 10^{-6}$
$v_2=225$	Poor deposition	3.2	$7.1200 \cdot 10^{-7}$	$6.5507 \cdot 10^{-7}$	$5,6932 \cdot 10^{-8}$
$v_3=400$	Effective deposition	6.4	$3.0564 \cdot 10^{-6}$	$6.5488 \cdot 10^{-7}$	$6.5893 \cdot 10^{-6}$

It is worth to notice that the term accounting for the loading of the fibers has not been considered in this case. It can be seen from Table 7 that when the particle impact velocity is low ( $v_1 = 100$  m/s in this case), no deposition occurs, and the particles rebound from the substrate. By applying the *Vi-Pe-R-A* equation, the difference between the two members, e.g.,  $E_p$  and  $E_a$ , respectively, is negative and equal to  $\Delta E(v_1) = 1.9771 \cdot 10^{-6}$  J: the available energy is lower than the energy required to activate the phenomena supposed to be the ones ruling adhesion. That should mean the particle does not possess the right energy values to activate the adhesion mechanisms, as confirmed experimentally. With the increase of the impact velocity ( $v_2 = 225$  m/s in this case), the particles seem to adhere to the substrate; however, the relatively low values from adhesion tests confirm the poor deposition overall behavior observed, meaning that this velocity is not capable of ensuring a good anchoring of the particles with the substrate. The experimental evidence is reported in Fig. 89a.

By applying the *Vi-Pe-R-A* equation, it results that  $E_p$  is slightly higher than  $E_a$ , as their difference  $\Delta E(v_2) = 5.6932 \cdot 10^{-8}$  J is relatively low. Note that not all particles impact perfectly perpendicular to the substrate and that some dissipative causes (such as collisions between the particles that can slow down their path or other dissipative phenomena) were not considered by the model. That means  $\Delta E(v_2)$  should be furtherly smaller, so resulting in very poor values of deposition efficiency and adhesion values. If the particle impact velocity increases furtherly ( $v_3 = 400$  m/s), an effective deposition of the particles was observed with the adhesion values equal to 6.4 MPa, in agreement with the literature [49]. In this case, an effective coverage was obtained, as confirmed by the picture shown in Fig. 89b. Under this condition, the model shows that  $E_p$  is noticeably higher than  $E_a$ , as proved by the difference  $\Delta E(v_3) = 2.4015 \cdot 10^{-6}$  J. This means that the energy possessed by the particles is high enough to offset the dissipative phenomena occurring during the impact. It is evident that the model proposed in the *Vi-Pe-R-A* equation is able to predict the experimental behavior of the particles during the deposition on a polymeric substrate with a reasonable level of

accuracy. As regards the reinforced specimens, the results given from the model that takes accounting also for the loading of the fibers, are reported in Table 8. It can be seen from Table 8 that no deposition was obtained when the particle impact velocity is 225 m/s. In this case, in agreement with the experimental outcomes, the difference between  $E_p$  and  $E_a$  in the  $Vi-Pe-R-A$  equation is negative and equal to  $\Delta E(v_1) = 1.3742 \cdot 10^{-6}$  J: the energy required for adhesion is greater than the energy possessed by the particle. In this case, contrary to what was observed for unreinforced polymeric substrates, the relatively higher value of impact velocity ( $v_1 = 225$  m/s) is not so great enough to promote adhesion; this behavior is due to the presence of the fibers that modify the mechanical properties of the substrate [53]. By increasing the impact velocity ( $v_2 = 400$  m/s), the particles seem to adhere to the reinforced substrate.

**Table 8** - Experimental vs. theoretical results for cold spray deposition of aluminum particles on fiber-reinforced polymer substrates.

Particle impact velocity [m/s]	Overall behaviour	Adhesion [MPa]	$E_p$ [J]	$E_a$ [J]	$\Delta E$ [J]
$v_1=225$	No deposition	n.a	$7.1200 \cdot 10^{-7}$	$2.0862 \cdot 10^{-6}$	$-1,3742 \cdot 10^{-6}$
$v_2=400$	Poor deposition	3.8	$3.0564 \cdot 10^{-6}$	$1.5263 \cdot 10^{-6}$	$1,5300 \cdot 10^{-6}$
$v_3=550$	Effective deposition	5.3	$5.7765 \cdot 10^{-6}$	$1.5260 \cdot 10^{-6}$	$4,25013 \cdot 10^{-6}$

Moreover, the results from the  $Vi-Pe-R-A$  equation showed that  $E_p$  is higher than  $E_a$ , as confirmed by the positive difference  $\Delta E(v_2) = 1.5300 \cdot 10^{-6}$  J. However, a poor deposition was observed experimentally, as proved by the relatively low values from the adhesion tests. That means the impact velocity is not so great to ensure a good anchoring of the particle with the substrate. The reason is that the reinforcing fibers make the polymer stiffer and more resistant compared to unreinforced polymeric substrates and higher impact energies are required to activate the adhesion mechanism promoting the coating formation [54]. If the impact velocity increases and reaches 550 m/s, the deposition occurs as the particles achieved the right velocity to adhere with the substrate. Also, the results from the model confirm this behavior, as proved by the greater positive difference between the two members of the  $Vi-Pe-R-A$  equation. However, under this condition, the experimental outcomes showed that degradation and erosion of the substrate took place due to the relatively high temperature values of the gas impinging onto the surface (as shown in Fig. 90).

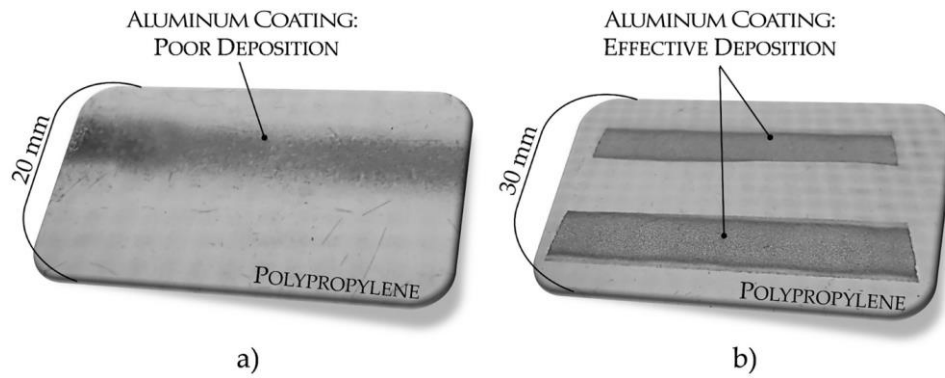


**Fig. 89** - Cold spray deposition of aluminum particles on unreinforced polymeric substrates varying the impact velocity: a)  $v_2 = 225$  m/s (Poor deposition); b)  $v_3 = 400$  m/s (effective deposition).

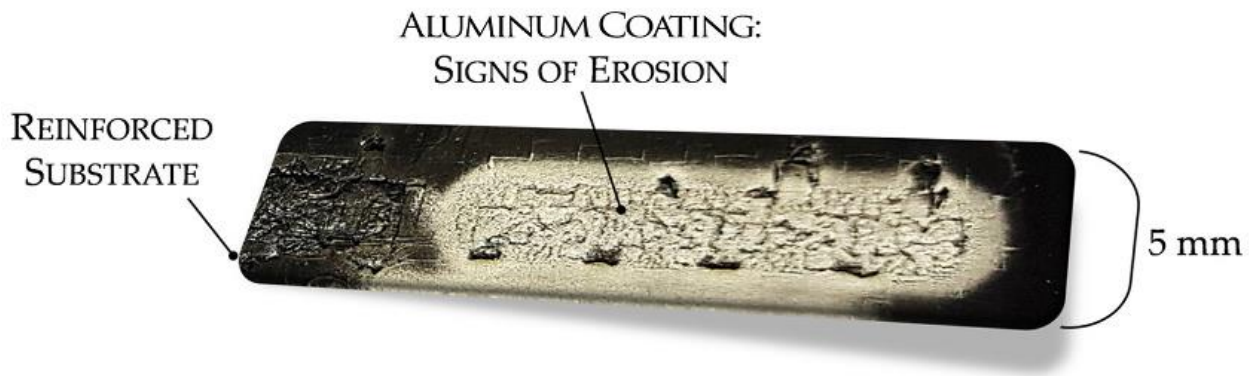


**Fig. 90** - Macrograph of CS deposition on fiber-reinforced composite substrates at  $v_3 = 550$  m/s showing erosion of the substrate.

Note that this phenomenon was not taken into account by the *Vi-Pe-R-A* equation for which the substrate was considered at room temperature. Based on these results, it is possible to assess that higher velocities are required to obtain adhesion on reinforced substrates, due to the higher properties of the composites, compared to pure polymeric substrates. However, due to the relatively high gas temperature involved to reach the right velocities, the polymeric material used to produce the composite should be carefully chosen aiming to prevent the erosion of the substrate during the deposition: high performance polymers (such as PEEK, for example) could represent a better choice to obtain good cold spray depositions. Anyhow, in all the considered cases-study, the model seems to be able to predict the behavior of a particle during the impact, taking into account the presence of the fibers, hindering the penetration of the particle and the higher rigidity of the substrate. Therefore, based on these results, the model can be effectively applied to literature cases to assess its capability to describe the adhesion process.

### 5.4.2 Application of the model to literature cases

The model has been applied to three different cases, taken from literature, and the results are here reported. In choosing the cases it was decided to represent the following conditions: i) the deposition on a pure soft polymer; ii) the deposition on a pure high-performance polymer; iii) the deposition on a fiber-reinforced polymer. To this end, the comprehensive work of Che et al. [25] dealing with the deposition of copper on ABS and PEEK substrates under different processing conditions and the paper by Gillet et al. [31], dealing with the deposition on carbon fiber reinforced PEEK (CFRP), have been used. The depositions on pure ABS and PEEK substrates coated with copper powder were firstly considered under the two different impact velocities reported in literature: i)  $v1 = 225$  m/s; ii)  $v2 = 500$  m/s; the relative deposition efficiencies ( $DE$ ) have been measured and reported by the authors [25]. The results given from model as well as the deposition efficiency measured are summarized in Table 9.

**Table 9** - Results from the literature cases: deposition of copper on ABS and PEEK substrates under different processing conditions.

Substrate	Particle impact velocity [m/s]	Overall behaviour	DE [%]	$E_p$ [J]	$E_a$ [J]	$\Delta E$ [J]
ABS	$v1=225$	Effective deposition	30	$3.2039 \cdot 10^{-6}$	$1.8698 \cdot 10^{-7}$	$3.0219 \cdot 10^{-6}$
	$v2=500$	Erosion	n.a	$1.5837 \cdot 10^{-5}$	$1.8695 \cdot 10^{-7}$	$1.5650 \cdot 10^{-5}$
PEEK	$v1=225$	Poor deposition	5	$3.2089 \cdot 10^{-6}$	$2.0229 \cdot 10^{-7}$	$2.0226 \cdot 10^{-6}$
	$v2=500$	Effective deposition	60	$1.5837 \cdot 10^{-5}$	$2.0226 \cdot 10^{-7}$	$1.5605 \cdot 10^{-5}$

The first interesting result is that the model predicts lower energy required to achieve adhesion for ABS compared to the PEEK, which is coherent with the lower mechanical properties of ABS. For the lower velocity ( $v1 = 225$  m/s), the energy possessed by the particle is higher than the one required for adhesion for both the substrates, as proved by the positive difference between  $E_p$  and  $E_a$ . However, it was observed an adequate deposition efficiency for ABS ( $>30$  %) while a very poor one was observed for PEEK ( $<5$  %). This experimental result can be better understood by looking at the outcomes from the model and considering that the available energy is in the proportion of about 20:1 with the energy required for adhesion for ABS, while it is about 10:1 for PEEK. Moreover, this is in agreement with the higher mechanical properties of PEEK, so more energy is required to activate the phenomena leading to adhesion. For the higher velocity ( $v2 = 500$  m/s), the particle energy value exceeds two orders of magnitude the energy required for bonding with  $\Delta E(v2) = 1.5650 \cdot 10^{-5}$  J for ABS and  $\Delta E(v2) = 1.5605 \cdot 10^{-5}$  J for PEEK; in this case, completely different results were observed for the two materials. For PEEK, a good deposition was observed with a high deposition efficiency ( $>60$  %), while severe erosion was

observed for ABS. In this case, in contrast to what was found for PEEK, the energy possessed by the particles is too high at the impact with the ABS substrate (greater >80 times compared to the energy required for adhesion), which is characterized by relatively low mechanical properties and, therefore, it damages. Moreover, the deterioration of the polymer and the consequent erosion can be ascribed to the lower glass transition temperature of the ABS compared to the PEEK substrate, as the latter retains good mechanical properties at relatively high temperatures. Note that this was not taken into account by the model. The *Vi-Pe-R-A* equation was also applied to study the deposition on a fiber-reinforced polymer. The work of Gillet et al. [31] studied the deposition of copper powders with different dimensions and the deposition efficiency versus the particle diameter was evaluated experimentally. The mean impact velocity for the three cases considered is 400 m/s. The particle mean diameters are: i)  $d1 = 10 \mu\text{m}$ ; ii)  $d2 = 23 \mu\text{m}$ ; iii)  $d3 = 38 \mu\text{m}$ . The results given by the model as well as the deposition efficiency measured by the authors [31] are summarized in Table 10.

**Table 10** - Results from the literature cases: deposition of powders with different dimensions on a fiber-reinforced polymer.

Substrate	Particle mean diameter [ $\mu\text{m}$ ]	Overall behaviour	DE [%]	$E_p$ [J]	$E_a$ [J]	$\Delta E$ [J]
CFRP	d1=10	Effective deposition	28	$5.8655 \cdot 10^{-7}$	$9.9845 \cdot 10^{-8}$	$4.8671 \cdot 10^{-7}$
	d2=23	Poor deposition	8	$6.2456 \cdot 10^{-6}$	$8.8443 \cdot 10^{-7}$	$5.3612 \cdot 10^{-6}$
	d3=38	Fiber Damage	<5	$2.7366 \cdot 10^{-5}$	$3.8911 \cdot 10^{-6}$	$2.3475 \cdot 10^{-5}$

If the particles mean diameter is  $10 \mu\text{m}$ , the energy required for the adhesion is moderately lower than the energy possessed by the particle. However, the available energy is greater >5 times compared to the energy required for bonding and the experimental analyses confirm the adhesion of the particles ( $DE = 28 \%$ ). This can be attributed to the higher deformation of the particles, which spread on the target surface promoted by the greater rigidity of the substrate. This result is very interesting in terms of the beneficial effects of the fibers reinforcing the polymeric substrate on CS deposition. A small increase in the particle diameter produces an increase of both  $E_p$  and  $E_a$  values with the balance energy equal to  $\Delta E(d2) = 5.3612 \cdot 10^{-6} \text{ J}$ . In this case, the available energy of the particle is in a proportion of 6:1 with the energy required for adhesion, which is about equal to the value reported for the previous condition ( $d1 = 10 \mu\text{m}$ ). However, the experimental results showed lower deposition efficiency values under higher penetration when impacting the composite substrate. This experimental-observed condition is related to the damage of the fibers that was not taken into account by the model. For the biggest diameter ( $d3 = 38 \mu\text{m}$ ), it can be seen again that the available energy is >6 times compared to the energy required for

adhesion, meaning that an effective deposition can occur, as shown for the first case ( $dI = 10 \mu\text{m}$ ). However, under this condition, the damage of the fibers was found experimentally with the coating that is carried away by the impinging particles that possess a high amount of kinetic energy.

## 5.5 Discussion

### 5.5.1. Adhesion mechanism

The first point interesting to discuss is that the model seems to well describe the literature experimental outcomes, the observed results in terms of deposition efficiency can be explained on the basis of the difference between the  $Ep$  and  $Ea$ , as defined by the model. When  $\Delta E$  was relatively low, the experiments in the literature showed a very low value of the deposition efficiency; it can be argued that in this case, only the particles with an impact angle close to  $90^\circ$  have enough energy to activate the conjectured phenomena, leading to the low value observed of the deposition efficiency. This can be asserted because the model does not consider some dissipative events like impacts among the particles and angles of impact different from  $90^\circ$ , so it can be assumed that the effective  $Ep$  was lower than  $Ea$  and then there is not enough energy to achieve adhesion. An increase of the deposition efficiency was observed when  $\Delta E$  increases until this difference becomes too high and the erosion of the substrate is observed. This suggests that for a higher value of  $Ep$  the particle has energy enough to activate phenomena such as damage of the fibers, breaking of the polymer that leads to global erosion behavior. Different results, in terms of  $\Delta E$  thresholds, were obtained for reinforced polymers and simple polymers, these results highlighted the role paid by the fibers and corroborated the choice to introduce fibers related terms in our model. It seems that the presence of the fibers strengthens the substrate causing the particles plastically deform more. Such a result is also well described by the model (cfr.  $A$  and  $B$  coefficients). Considering the results, it is possible to suggest that the prevailing mechanism is the mechanical interlocking between the particle and the substrate: no chemical reaction between the powder and the substrate occurs and, as confirmed by previous literature works [47], the thermal softening is not necessary for the onset of jetting. This phenomenon occurs mainly due to the plastic deformation of the substrate. If the substrate is stiff enough, and the powder is a soft metal, plastic deformation of the particle can be also expected. When both the substrate and the particle contribute to the plastic deformation, a better deposition efficiency is observed. It is also interesting to discuss the contribution of the conjectured phenomena under the light of the energy required which is portrayed in Table 11. Observing the values of the different contributions presented in Table 11, it is evident that the presence of the fibers strongly influences the deposition. In fact, due to the fibers stiffening effect, the reinforced substrate requires more energy to be deformed of the same

quantity (as evidenced by comparing the values of the energy required to plastically deform the substrate for the composite substrate and the pure polymeric substrate,  $EPLA(s)$ ). It is possible to assess that the substrate characteristics have a crucial role in the deposition and have to be carefully considered. The role of the fibers in the deposition will be furtherly investigated in the next paragraph.

**Table 11** - Single energy contribution to particle adhesion for an aluminum particle on composite and pure polymeric substrate ( $v = 400$  m/s), where  $EPLA(s)$  and  $EPLA(p)$  are the energy values required to plastically deform the substrate and the particle, respectively;  $Eload$  is the energy required for the loading of the fibers and  $ET$  is the thermal energy.

	$E_{PLA(S)}$ [J]	$E_{PLA(P)}$ [J]	$E_{PLA(P)}$ [J]	$E_t$ [J]
FRP	$3.40 \cdot 10^{-6}$	$9.22 \cdot 10^{-7}$	$1.24 \cdot 10^{-5}$	$1.70 \cdot 10^{-10}$
Pure Polymer	$4.62 \cdot 10^{-8}$	$4.07 \cdot 10^{-7}$	0	$1.70 \cdot 10^{-10}$

### 5.5.2. Role of the fibers

The fibers have a complex influence on the adhesion: on one hand, the particle energy is partially absorbed by the loading of the fibers, on the other hand, the presence of the fibers promotes the deformation of the particle by strengthening the matrix. Plus, the physical presence of the fibers limits the plunging depth that the particle can achieve because at a certain point the particle touches and damages the fiber. Both these evidences can be explained by considering the sketch reported in Fig. 91. The first row is representative of the low velocity impact. In the case of pure polymer, the particle impacts on a relatively soft material characterized by a reduced stiffness; the result is that the particle does not experience plastic deformation, so the surplus of energy is used to produce the rebounding phenomenon, hampering the adhesion. On the other hand, as shown in the second row of Fig. 91a, when the surplus of energy becomes very high, the particle can penetrate the polymeric matrix that plastically deforms and tends to embed the particle, so promoting the interlocking mechanism. In FRPs, the fibers reinforcement stiffens the polymeric substrate and promotes the particle deformation and adhesion, as shown in Fig. 91b (top). However, with the increasing of the impact velocity, the particle could have enough energy to penetrate within the matrix, impacting with the fibers reinforcement that can fail and break, as schematically shown in Fig. 91b (bottom). Moreover, as confirmed by literature [31,55], the influence of the fibers and the consequent lowering of the deposition window is strongly dependent on the surface matrix thickness of the fiber-reinforced substrate. In fact, as a thicker layer of polymer is present on the

surface, the impact behavior of the composite tends to draw nearer to the pure polymeric substrate behavior. Therefore, the composite substrate needs to be accurately designed in order to guarantee the best performances when spraying metal powders. This crucial aspect should be carefully considered in further developments of this model.

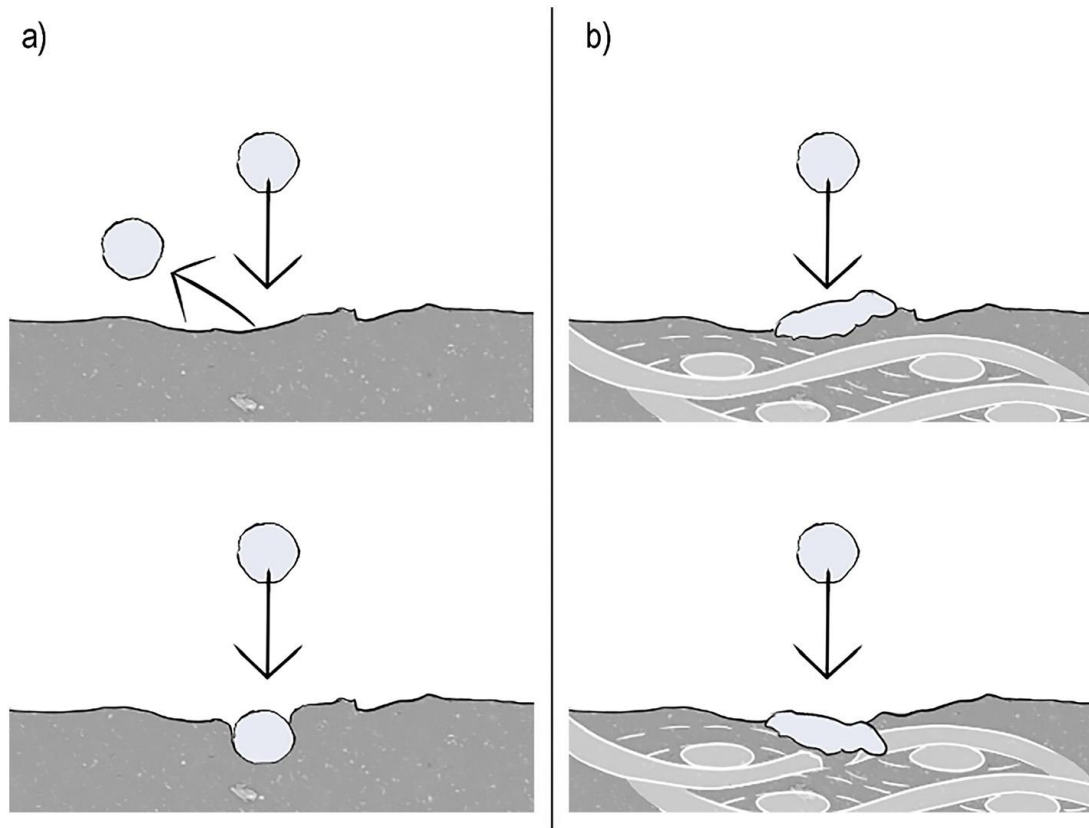


**Fig. 91** - Sketches of the impacts for increasing  $\Delta E$  values (a given  $\Delta E$  for each raw in the figure) with different substrates: a) impact of a particle on a pure polymeric substrate, b) impact of a particle on a composite substrate.

### 5.5.3 Predictive simulations through *Vi-Pe-R-A* equation

The *Vi-Pe-R-A* equation can be used as a valid tool to perform qualitative analyses to predict the outcomes of the process, varying the feedstock properties and process conditions of cold spray depositions on polymer-based materials. In this section, the influence of some peculiar parameters on CS deposition will be assessed, and the *Vi-Pe-Ra* equation will be employed aiming to provide further insights into the cold spray process. The parameters influencing the deposition of metallic particles on polymer-based substrates were classified here into three main categories, for the clarity of the discussion: the powder parameters, the process parameters and the substrates parameters. A single parameter was chosen for each category and its effect on CS deposition was analyzed. In

particular, the influence of i) the particle size, ii) the particle impact velocity and iii) the fiber volume percentage within the composite substrate was examined through the *Vi-Pe-R-A* equation.

**5.3.1. Influence of the particle size** Aiming to assess the influence of the particle size when cold spraying on polymers, the energy possessed by the particle and the energy required to obtain adhesion (namely  $E_p$  and  $E_a$ , respectively) have been plotted with respect to the mean radius of the powders, keeping constant all the remaining parameters that do not involve the particle radius in the *Vi-Pe-R-A* equation. In agreement with the materials used for the experimental validation of the theoretical model a sheet of polypropylene was considered as substrate and AlSi10Mg aluminum powders were chosen as impacting particles. For this scope, three different values of impact velocity were considered, chosen accordingly to the experiments presented in the previous section:  $v_1 = 100$  m/s,  $v_2 = 225$  m/s and  $v_3 = 400$  m/s.. It is worth noticing that  $E_a$  is scarcely influenced by the impact velocity, as expected through the *Vi-Pe-R-A* equation. In fact, the curves obtained for the three values of impact velocity appear to overlap in the figure. This is furtherly highlighted by observing the magnification in Fig. 92. It is possible to note that by increasing the particle size, the energy possessed by the particle increases. However, regardless of the particle radius chosen, when the particles are sprayed with the lowest impact velocity ( $v_1$ ), the adhesion never occurs, as confirmed by experimental data obtained for the 30  $\mu\text{m}$  diameter. On the other hand, for higher impact velocities ( $v_2$  and  $v_3$ ) the adhesion occurs for every value of the radius of the powder considered. It is crucial to observe that for relatively small diameter values, the energy surplus possessed by the particle could not be great enough to obtain good adhesion as some dissipative phenomena have not been considered within the model. In fact, for very small values of the particle radius (lower than 15  $\mu\text{m}$ ), the  $E_p$  and  $E_a$  curves tend to overlap. For this reason, spraying relatively bigger particles could lead to better-adhered coatings regardless of impact velocity.

**5.3.2. Influence of the particle impact velocity** The particle impact velocity is the most important cold spray process parameter that influences the bonding phenomena. It is the result of the process parameters chosen for the deposition, such as the gas temperature, the gas pressure and the stand-off distance, which have to be properly set for the coating formation and grow-up. Both the  $E_p$  and  $E_a$  energy curves were plotted by varying the particle impact velocity for three different powder materials (Fig. 93). In particular, the *Vi-Pe-R-A* equation was particularized for aluminum, steel and copper materials in order to assess the capability of the model to predict the behavior of a wide range of materials characterized by different densities and mechanical characteristics. The particle diameter was kept equal to 30  $\mu\text{m}$ . The unreinforced polypropylene was chosen for this analysis. The model was proved to be able of predicting the critical velocity,  $v_{crit}$  (namely, the

threshold velocity above which the adhesion occurs) for all the powder materials considered, as evident in Fig. 93.

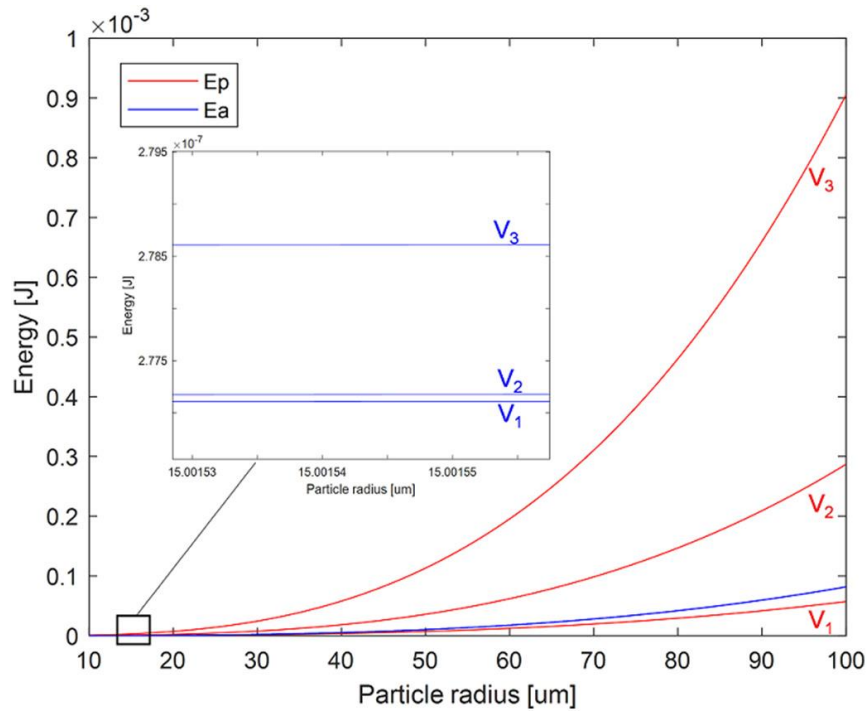


**Fig. 92** - Predictive simulations through *Vi-Pe-R-A* equation showing the trend of  $E_p$  and  $E_a$  with the particle size for three different impact velocities:  $v_1 = 100$  m/s,  $v_2 = 225$  m/s and  $v_3 = 400$  m/s.

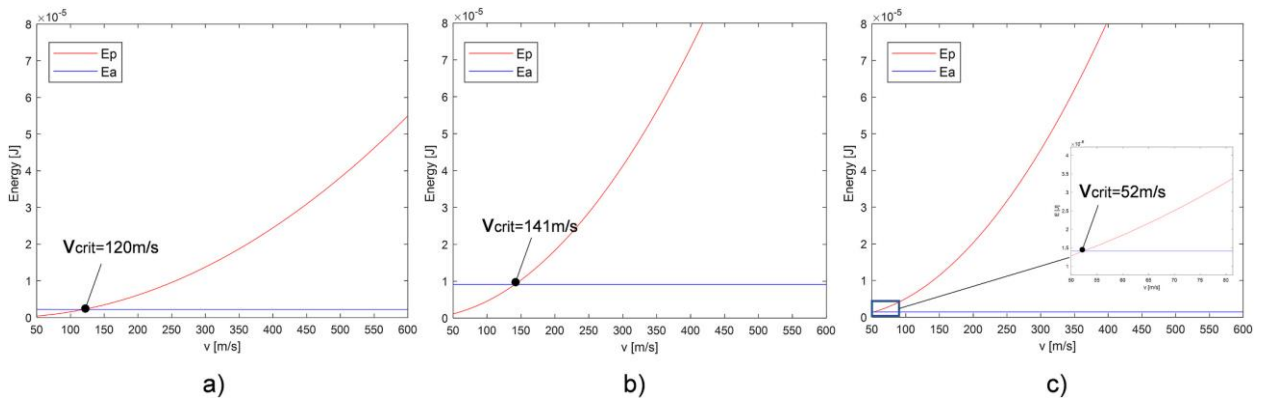


**Fig. 93** - Plot of  $E_p$  and  $E_a$  by varying the particle impact velocity for three different powder materials: a) aluminum b) steel c) copper.

In fact, the critical velocity can be found at the intersection point between  $E_p$  and  $E_a$  curves, as it is the minimum value of velocity required to obtain adhesion. The steel and copper curves showing the energy possessed by the particle ( $E_p$  in Fig. 93b and c) are characterized by a greater slope compared to aluminum (Fig. 92a): in fact, those particles possess higher energy when sprayed with the same process parameters due to the relatively greater mass density. However, the mechanical properties of aluminum are lower than those of steel; in particular, the particle made of aluminum

is characterized by a lower yield strength (290 MPa), so resulting in a more ductile and deformable material when sprayed onto the substrate. The result is that it is easier to deposit aluminum particles compared to steel, characterized by a yield strength of 350 MPa. It is also possible to observe from Fig. 93c that copper, which is the material characterized by the lowest value of yield strength (33 MPa) and highest value of density among the three materials under examination, has the lowest value of critical velocity (52 m/s), resulting to be the easiest material to deposit compared to steel and aluminum. It is known from literature that when cold spraying on metallic substrates, it is possible to define an erosion velocity as the upper limit of the particle impact velocity above which the erosive effects, due to hydrodynamic penetration of the substrate by the particles, occur. This phenomenon is known from large-scale impact dynamics and can also be applied to cold spray [56]. When cold spraying on polymers, it is crucial to underline that the concept of erosion of a polymeric substrate impacted by metal particles is not clearly defined in the literature. In fact, the phenomena occurring when the particles impact the substrate with a velocity higher than the critical one without obtaining adhesion, are yet to be understood. For this reason, in this work, the erosion velocity has been assessed experimentally for a single case study, as the *Vi-Pe-R-A* equation does not take into account these phenomena. The deposition window for the aluminum case study is shown in Fig. 94. It can be noticed that the critical velocity (120 m/s) was determined at the intersection point between *Ep* and *Ea* curves, while the erosion velocity (for the PP substrate) was found from experimental tests to be equal to 600 m/s.

#### 5.5.4 Influence of the fiber volume percentage within the composite substrate

The *Vi-Pe-R-A* equation can represent an effective tool to evaluate the effects of the fiber volume percentage within the composite substrate on CS deposition. In this section, AlSi10Mg aluminum powders (30  $\mu\text{m}$  as mean diameter) were chosen as impacting particles and sheets of polypropylene reinforced with carbon fibers were considered as substrates for the analyses. Both the *Ep* and *Ea* energy curves were plotted by varying the fiber volume percentage for two different impact velocities,  $v1 = 225$  m/s and  $v2 = 304$  m/s; the results are shown in Fig. 95. It can be seen from the figure that the energy required for adhesion (*Ea*) tends to increase with the increase of the fiber volume percentage due to the stiffening effects of the fibers. If the particle impact velocity is set to 225 m/s and the composite substrate is characterized by a fiber volume percentage equal to 50 % (which are the conditions tested experimentally), the particles cannot adhere to the target surface, as the energy required for adhesion is greater than the energy possessed by the particle. This is the reason for which no bonding was observed experimentally under these conditions.

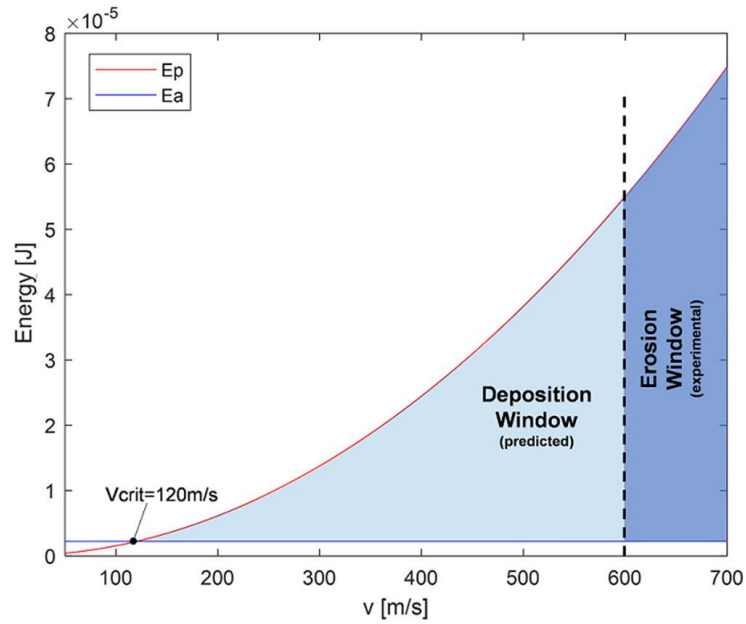


**Fig. 94** - Deposition window when cold spraying aluminum particles ( $30 \mu\text{m}$ ) on PP substrate.

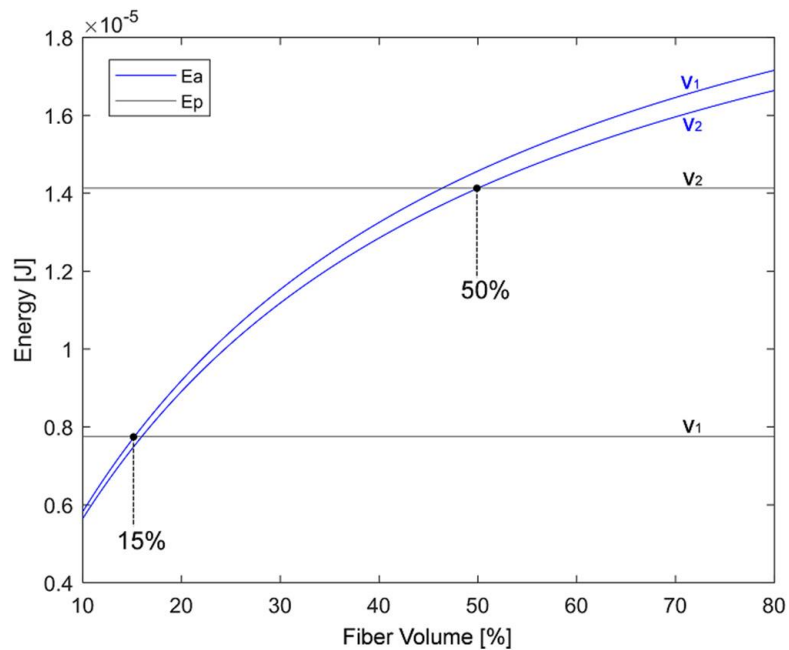


**Fig 95** - Plot of  $E_p$  and  $E_a$  by varying the fiber volume percentage for two different impact velocities,  $v_1 = 225$  m/s and  $v_2 = 304$  m/s. Aluminum particles on reinforced PP substrate.

However, observing the figure, it is possible to assess that there is an upper limit of fiber volume percentage above which the considered impact velocity would not be sufficient to obtain adhesion. In this case, for a composite characterized by a fiber volume percentage lower than 15 %, the adhesion could occur as the substrate would be less stiff and would easily deform for the anchorage of the particle. The minimum particle velocity required for adhesion when the polymeric PP substrate is reinforced with a carbon fiber volume percentage of 50 % (which are the tested

conditions reported in Table 4) is 304 m/s, as also shown in Fig. 95. That means that if the aluminum particle is sprayed with those parameters, it would be possible to obtain the deposition on a composite substrate with a fiber volume percentage equal or lower than 50 %. The model could also be useful to properly assess the best lay-up strategy of the substrate and predict the best process parameters to employ to spray on composite characterized by different volume percentages.

## **Conclusion**

The aim of this work was to comprehend the phenomena occurring during cold spray deposition on polymer and composite substrate and exploit the full potential of this technology. By analysing different substrate/powder couplings and testing the resulting properties interesting steps forward into the understanding of the principles regulating the adhesion have been made. Despite the characteristics of the coated substrates are not yet optimal and the coating produced still results inhomogeneous, the road to fully develop the potential of this technology on polymeric and composite substrates looks now shorter. Compared to literature shown in the introduction section of this work, many steps forward have been made on the understanding and development of cold spray technology on polymer-based materials.

The experimental campaigns carried out on thermoplastic matrix composites were conducted by varying all the process parameters in an orderly manner, clarifying the influence of each of these. Furthermore, for the first time in the literature, the influence of polymer stratification on deposition was highlighted: by varying the surface layer of polymer it was possible to understand the influence of the presence of fibres on deposition as well as define an optimal stratification for deposition. Moreover, the influence of the ductility of the powders deposited on the same typology of substrates was highlighted: rather than simply using the easier powders to deposit, as happened in the literature, the deposition of less ductile powders, such as steel ones, was attempted. This not only opened new possibilities for the technology but also gave important insights into the deposition mechanisms: in fact, it was shown that the deformation of the particles is not essential for cold spray deposition.

Furthermore, since the difficulty of adhesion of metal particles on thermosetting polymers had already been highlighted in the literature, instead of focusing on the most suitable process parameters to overcome this problem, innovative solutions have been proposed to circumvent the issue: surface treatments based on PLA or of metal powders have been screened, opening new avenues for expanding the field of use of cold spray technology. The deposition campaigns on thermosetting substrates have made it clear that, by using suitable measures and changing the stratification and composition of the surface layer of composite, it is possible to obtain cold spray depositions, although still not comparable to that obtained on thermoplastics in terms of quality.

Among all the works present in literature, a new idea of customizing the substrate to facilitate the cold spray deposition has been analyzed and it was proposed a hybrid approach between the 3D printing of thermoplastic-based composite materials and cold spray. In this way, the substrates produced are optimized for deposition, while enhancing all the mechanical characteristics required. The Fused Filament Fabrication technology has proved to be suitable for producing

composite material panels that are perfect for accommodating the powders deposited by cold spray. It is, therefore, possible to produce customised substrates for different applications, and perfectly suited to receive metal powders coating and enhance the characteristics of every material involved. This knowledge opens the doors for even greater integration between these two technologies which would lead to a streamlining of production time and greater automation than it would allow anyone to quickly obtain their product with the characteristics of lightness and versatility of the composite and the exceptional surface qualities of metal. It will therefore be necessary to continue to follow this trend in order to produce the best possible substrates for deposition with the most suitable characteristics for their use in different sectors. It will be important to analyse how to improve the printing process, how to better integrate the printing process with the cold spray deposition process and how to further functionalize the substrates.

The development of the theoretical model has helped to understand the phenomena prevailing during adhesion thus giving ideas on how to emphasize them and maximize the quantity of adhered particles. From the model emerged that mechanical interlocking mechanisms might be the prevailing phenomena ruling adhesion on composite and polymeric substrates. Moreover, the different behaviour between polymeric substrates and composite substrates was analysed, revealing the effect of the fibres in the lowering of the deposition window. The model proved to also be a valid instrument to understand how to change the process parameters depending on the type of powder or substrate used.

All these preliminary studies and the development of an energy-based theoretical model, that allowed to further improve the understanding of the bonding mechanisms and facilitate the choice of process parameters for each particle/substrate coupling, led to the understanding that the best way to obtain manufactures that fully meet the requirements of use and optimize compatibility with metal powders was to produce totally customized substrates.

## References

1. Brighenti R, Cosma MP, Marsavina L, et al (2021) Laser-based additively manufactured polymers: a review on processes and mechanical models. *J. Mater. Sci.*

2. Jeandin M, Delloro F, Léger PE, et al (2018) Cold spray under the banner of thermal spray in the whirlwind of additive manufacturing. *Surf Eng.* <https://doi.org/10.1080/02670844.2018.1471188>
3. Kelkar M, Heberlein J (2002) Wire-Arc Spray Modeling. *Plasma Chem Plasma Process.* <https://doi.org/10.1023/A:1012924714157>
4. Wu B, Pan Z, Ding D, et al (2018) A review of the wire arc additive manufacturing of metals: properties, defects and quality improvement. *J. Manuf. Process.*
5. Gapsari F, Hidayati NA, Setyarini PH, et al (2021) Hydroxyapatite coating on stainless steel 316l using flame spray technique. *Int J Eng Trans B Appl.* <https://doi.org/10.5829/IJE.2021.34.02B.22>
6. Stoltenhoff T, Kreye H, Richter HJ (2002) An analysis of the cold spray process and its coatings. *J Therm Spray Technol.* <https://doi.org/10.1361/105996302770348682>
7. Raelison RN, Xie Y, Sapanathan T, et al (2018) Cold gas dynamic spray technology: A comprehensive review of processing conditions for various technological developments till to date. *Addit. Manuf.*
8. Schmidt T, Gärtner F, Assadi H, Kreye H (2006) Development of a generalized parameter window for cold spray deposition. *Acta Mater.* <https://doi.org/10.1016/j.actamat.2005.10.005>
9. Palodhi L, Singh H (2020) On the Dependence of Critical Velocity on the Material Properties During Cold Spray Process. *J Therm Spray Technol.* <https://doi.org/10.1007/s11666-020-01105-7>
10. Guo H, Zhao X, An Y, et al (2021) Fabrication and effect of heat treatment on the microstructure and tribology properties of HVOF-sprayed CoMoCrSi coating. *J Mater Sci.* <https://doi.org/10.1007/s10853-021-05986-z>
11. Viscusi A, Astarita A, Gatta R Della, Rubino F (2019) A perspective review on the bonding mechanisms in cold gas dynamic spray. *Surf. Eng.*
12. Hassani-Gangaraj M, Veysset D, Champagne VK, et al (2018) Adiabatic shear instability is not necessary for adhesion in cold spray. *Acta Mater.* <https://doi.org/10.1016/j.actamat.2018.07.065>
13. Dong G, Tang Y, Li D, Zhao YF (2020) Design and optimization of solid lattice hybrid structures fabricated by additive manufacturing. *Addit Manuf.* <https://doi.org/10.1016/j.addma.2020.101116>
14. Zeng G, Zahiri SH, Gulizia S, et al (2021) Hybrid additive manufacturing of biocompatible Ti–Ta composite structures for biomedical applications. *J Mater Res.* <https://doi.org/10.1557/s43578-021-00190-w>
15. Blindheim J, Grong Ø, Welo T, Steinert M (2020) On the mechanical integrity of AA6082 3D structures deposited by hybrid metal extrusion & bonding additive manufacturing. *J Mater Process Technol.* <https://doi.org/10.1016/j.jmatprotec.2020.116684>
16. Li F, Chen S, Shi J, et al (2017) Evaluation and optimization of a hybrid manufacturing process combining wire arc additive manufacturing with milling for the fabrication of stiffened panels. *Appl Sci.* <https://doi.org/10.3390/app7121233>
17. Viscusi A, Perna AS, Astarita A, et al (2019) Experimental study of cold sprayed metallic coatings on thermoplastic matrix composites. In: *Key Engineering Materials*
18. Astarita A, Boccarusso L, Durante M, et al (2018) Study of the Production of a Metallic Coating on Natural Fiber Composite Through the Cold Spray Technique. *J Mater Eng Perform.* <https://doi.org/10.1007/s11665-018-3147-7>
19. Bortolussi V, Borit F, Chesnaud A, et al (2016) Cold spray of metal-polymer composite coatings onto Carbon Fiber-Reinforced Polymer (CFRP). In: *Proceedings of the International Thermal Spray Conference*
20. Joshi, Nylen (2019) Advanced Coatings by Thermal Spray Processes. *Technologies.* <https://doi.org/10.3390/technologies7040079>
21. Campbell JP, Astarita A, Viscusi A, Saha GC (2020) Investigation of strain-hardening characteristics of cold-sprayed Al–Al<sub>2</sub>O<sub>3</sub> coatings: a combined nanoindentation and expanding cavity models approach. *Surf Eng.* <https://doi.org/10.1080/02670844.2019.1620438>
22. Viscusi A, Ammendola P, Astarita A, et al (2016) Aluminum foam made via a new method based on cold gas dynamic sprayed powders mixed through sound assisted fluidization technique. *J Mater Process Technol.* <https://doi.org/10.1016/j.jmatprotec.2015.12.030>

23. Bhatnagar A (2016) *Lightweight Ballistic Composites: Military and Law-Enforcement Applications: Second Edition*
24. Hueber C, Fischer G, Schwingshandl N, Schledjewski R (2019) Production planning optimisation for composite aerospace manufacturing. *Int J Prod Res.* <https://doi.org/10.1080/00207543.2018.1554918>
25. Zhang H, Huang T, Jiang Q, et al (2021) Recent progress of 3D printed continuous fiber reinforced polymer composites based on fused deposition modeling: a review. *J. Mater. Sci.*
26. Verma P, Bansala T, Chauhan SS, et al (2021) Electromagnetic interference shielding performance of carbon nanostructure reinforced, 3D printed polymer composites. *J Mater Sci.* <https://doi.org/10.1007/s10853-021-05985-0>
27. Yao Y, Jin S, Zou H, et al (2021) Polymer-based lightweight materials for electromagnetic interference shielding: a review. *J. Mater. Sci.*
28. Lin T, Yu H, Wang L, et al (2021) A review of recent advances in the preparation of polyaniline-based composites and their electromagnetic absorption properties. *J. Mater. Sci.*
29. Senis EC, Golosnoy IO, Dulieu-Barton JM, Thomsen OT (2019) Enhancement of the electrical and thermal properties of unidirectional carbon fibre/epoxy laminates through the addition of graphene oxide. *J Mater Sci.* <https://doi.org/10.1007/s10853-019-03522-8>
30. Chen X, Smorgonskiy A, Li J, et al (2019) Nonlinear electrical conductivity through the thickness of multidirectional carbon fiber composites. *J Mater Sci.* <https://doi.org/10.1007/s10853-018-3127-1>
31. Jin Z, Shen YA, Huo F, et al (2021) Electromigration behavior of silver thin film fabricated by electron-beam physical vapor deposition. *J Mater Sci.* <https://doi.org/10.1007/s10853-021-05862-w>
32. Cihanoğlu G, Ebil Ö (2021) Robust fluorinated siloxane copolymers via initiated chemical vapor deposition for corrosion protection. *J Mater Sci.* <https://doi.org/10.1007/s10853-021-06060-4>
33. Miquelot A, Youssef L, Villeneuve-Faure C, et al (2021) In- and out-plane transport properties of chemical vapor deposited TiO<sub>2</sub> anatase films. *J Mater Sci.* <https://doi.org/10.1007/s10853-021-05955-6>
34. Olivera S, Muralidhara HB, Venkatesh K, et al (2016) Plating on acrylonitrile–butadiene–styrene (ABS) plastic: a review. *J. Mater. Sci.*
35. Corni I, Chater RJ, Boccaccini AR, Ryan MP (2012) Electro co-deposition of Ni-Al<sub>2</sub>O<sub>3</sub> composite coatings. *J Mater Sci.* <https://doi.org/10.1007/s10853-012-6381-7>
36. Vergason G (2019) Advances in decorative PVD chromium coatings for polymer substrates. In: *Annual Technical Conference - ANTEC, Conference Proceedings*
37. S K, M Chavan N, D SR (2019) Cold spraying: A low temperature variant of thermal spray techniques to deposit metallic materials. *Front Adv Mater Res.* <https://doi.org/10.34256/famr1914>
38. Silvello A, Cavaliere PD, Albaladejo V, et al (2020) Powder properties and processing conditions affecting cold spray deposition. *Coatings.* <https://doi.org/10.3390/coatings10020091>
39. Yin S, Cavaliere P, Aldwell B, et al (2018) Cold spray additive manufacturing and repair: Fundamentals and applications. *Addit. Manuf.* 21:628–650
40. Rokni MR, Feng P, Widener CA, Nutt SR (2019) Depositing Al-Based Metallic Coatings onto Polymer Substrates by Cold Spray. *J Therm Spray Technol.* <https://doi.org/10.1007/s11666-019-00911-y>
41. Perna AS, Viscusi A, Astarita A, et al (2019) Manufacturing of a Metal Matrix Composite Coating on a Polymer Matrix Composite Through Cold Gas Dynamic Spray Technique. *J Mater Eng Perform.* <https://doi.org/10.1007/s11665-019-03914-6>
42. Gillet V, Aubignat E, Costil S, et al (2019) Development of low pressure cold sprayed copper coatings on carbon fiber reinforced polymer (CFRP). *Surf Coatings Technol* 364:306–316. <https://doi.org/10.1016/j.surfcoat.2019.01.011>
43. Che H, Vo P, Yue S (2019) Investigation of Cold Spray on Polymers by Single Particle Impact Experiments. *J Therm Spray Technol* 28:135–143. <https://doi.org/10.1007/s11666-018-0801-4>
44. Perna AS, Viscusi A, Astarita A, et al (2019) Experimental study of functionalized polymer matrix composite

- with multi-material metal coatings produced by means of cold spray technology. In: *Key Engineering Materials*
45. Chu X, Che H, Yue S (2019) Understanding the cold spray deposition characteristics of mixed metal powders. *MRS Adv.* <https://doi.org/10.1557/adv.2019.418>
  46. Papa I, Russo P, Astarita A, et al (2019) Influence of the metallic cold spray deposition on the low-velocity impact behaviour of composite laminates. In: *Key Engineering Materials*
  47. Lomonaco P, Weiller S, Feki I, et al (2019) Cold spray technology to promote conductivity of short carbon fiber reinforced polyether-ether-ketone (PEEK). In: *Key Engineering Materials*
  48. Che H, Gagné M, Rajesh PSM, et al (2018) Metallization of Carbon Fiber Reinforced Polymers for Lightning Strike Protection. *J Mater Eng Perform.* <https://doi.org/10.1007/s11665-018-3609-y>
  49. Chen C, Xie X, Xie Y, et al (2018) Metallization of polyether ether ketone (PEEK) by copper coating via cold spray. *Surf Coatings Technol* 342:209–219. <https://doi.org/10.1016/j.surfcoat.2018.02.087>
  50. Stenson C, McDonnell KA, Yin S, et al (2018) Cold spray deposition to prevent fouling of polymer surfaces. *Surf Eng.* <https://doi.org/10.1080/02670844.2016.1229833>
  51. Małachowska A, Winnicki M, Stachowicz M, Korzeniowski M (2018) Metallisation of polycarbonates using a low pressure cold spray method. *Surf Eng* 34:251–258. <https://doi.org/10.1080/02670844.2016.1277843>
  52. Dong S, Liao H (2018) Substrate pre-treatment by dry-ice blasting and cold spraying of titanium. *Surf Eng.* <https://doi.org/10.1080/02670844.2016.1210894>
  53. Che H, Liberati A, Vo P, Yue S (2018) Cold spray of mixed sn-zn and sn-al powders on carbon fiber reinforced polymers. In: *Materials Science Forum*
  54. Che H, Chu X, Vo P, Yue S (2018) Metallization of Various Polymers by Cold Spray. *J Therm Spray Technol.* <https://doi.org/10.1007/s11666-017-0663-1>
  55. Bortolussi V, Figliuzzi B, Willot F, et al (2018) Morphological modeling of cold spray coatings. *Image Anal Stereol.* <https://doi.org/10.5566/ias.1894>
  56. Che H, Chu X, Vo P, Yue S (2017) Cold spray of mixed metal powders on carbon fibre reinforced polymers. *Surf Coatings Technol.* <https://doi.org/10.1016/j.surfcoat.2017.09.052>
  57. Kromer R, Danlos Y, Aubignat E, et al (2017) Coating deposition and adhesion enhancements by laser surface texturing—metallic particles on different classes of substrates in cold spraying process. *Mater. Manuf. Process.*
  58. Małachowska A, Winnicki M, Konat Ł, et al (2017) Possibility of spraying of copper coatings on polyamide 6 with low pressure cold spray method. *Surf Coatings Technol* 318:82–89. <https://doi.org/10.1016/j.surfcoat.2017.02.001>
  59. Che H, Vo P, Yue S (2017) Metallization of carbon fibre reinforced polymers by cold spray. *Surf Coatings Technol* 313:236–247. <https://doi.org/10.1016/j.surfcoat.2017.01.083>
  60. Lupoi R, Stenson C, McDonnell KA, et al (2016) Antifouling coatings made with Cold Spray onto polymers: Process characterization. *CIRP Ann - Manuf Technol* 65:545–548. <https://doi.org/10.1016/j.cirp.2016.04.015>
  61. Ye H, Wang J (2014) Preparation of aluminum coating on Lexan by cold spray. *Mater Lett.* <https://doi.org/10.1016/j.matlet.2014.08.119>
  62. Gardon M, Melero H, Garcia-Giralt N, et al (2014) Enhancing the bioactivity of polymeric implants by means of cold gas spray coatings. *J Biomed Mater Res - Part B Appl Biomater.* <https://doi.org/10.1002/jbm.b.33134>
  63. Vucko MJ, King PC, Poole AJ, et al (2014) Assessing the antifouling properties of cold-spray metal embedment using loading density gradients of metal particles. *Biofouling.* <https://doi.org/10.1080/08927014.2014.906584>
  64. Ganesan A, Yamada M, Fukumoto M (2013) Cold spray coating deposition mechanism on the thermoplastic and thermosetting polymer substrates. In: *Journal of Thermal Spray Technology.* pp 1275–1282
  65. Gardon M, Latorre A, Torrell M, et al (2013) Cold gas spray titanium coatings onto a biocompatible polymer. *Mater Lett* 106:97–99. <https://doi.org/10.1016/j.matlet.2013.04.115>

66. King PC, Poole AJ, Horne S, et al (2013) Embedment of copper particles into polymers by cold spray. *Surf Coatings Technol* 216:60–67. <https://doi.org/10.1016/j.surfcoat.2012.11.023>
67. Vucko MJ, King PC, Poole AJ, et al (2013) Polyurethane seismic streamer skins: an application of cold spray metal embedment. *Biofouling*. <https://doi.org/10.1080/08927014.2012.741682>
68. Ganesan A, Affi J, Yamada M, Fukumoto M (2012) Bonding behavior studies of cold sprayed copper coating on the PVC polymer substrate. *Surf Coatings Technol* 207:262–269. <https://doi.org/10.1016/j.surfcoat.2012.06.086>
69. Vucko MJ, King PC, Poole AJ, et al (2012) Cold spray metal embedment: an innovative antifouling technology. *Biofouling*. <https://doi.org/10.1080/08927014.2012.670849>
70. Giraud D, Borit F, Guipont V, et al (2012) Metallization of a polymer using cold spray: Application to aluminum coating of polyamide 66. In: *Proceedings of the International Thermal Spray Conference*
71. Affi J, Okazaki H, Yamada M, Fukumoto M (2011) Fabrication of aluminum coating onto CFRP substrate by cold spray. *Mater Trans*. <https://doi.org/10.2320/matertrans.T-M2011807>
72. Zhou XL, Chen AF, Liu JC, et al (2011) Preparation of metallic coatings on polymer matrix composites by cold spray. *Surf Coatings Technol* 206:132–136. <https://doi.org/10.1016/j.surfcoat.2011.07.005>
73. Lupoi R, O'Neill W (2010) Deposition of metallic coatings on polymer surfaces using cold spray. *Surf Coatings Technol* 205:2167–2173. <https://doi.org/10.1016/j.surfcoat.2010.08.128>
74. Sturgeon A, Dunn B, Celotto S, O'Neill B (2006) Cold sprayed coatings for polymer composite substrates. In: *European Space Agency, (Special Publication) ESA SP*
75. Zhang D, Shipway PH, McCartney DG (2005) Cold gas dynamic spraying of aluminum: The role of substrate characteristics in deposit formation. *J Therm Spray Technol* 14:109–116. <https://doi.org/10.1361/10599630522666>
76. Qi X, Wu X, Gong Y, et al (2021) Interlaminar mechanical properties of nano- and short-aramid fiber reinforced glass fiber-aluminum laminates: a comparative study. *J Mater Sci*. <https://doi.org/10.1007/s10853-021-06003-z>
77. Cai Y, An X, Zou Q, et al (2021) Mechanical properties and failure mechanisms of composite laminates with classical fabric stacking patterns. *J Mater Sci*. <https://doi.org/10.1007/s10853-021-06073-z>
78. Khraponichev K, Incerti D, Carolan D, Fergusson A (2021) Effect of rapid manufacturing on the performance of carbon fibre epoxy polymers. *J Mater Sci*. <https://doi.org/10.1007/s10853-020-05675-3>
79. Huang Z, Nie X, Xia Y (2004) Effect of strain rate and temperature on the dynamic tensile properties of GFRP. *J Mater Sci*. <https://doi.org/10.1023/B:JMISC.0000026956.45427.68>
80. Walker M (2018) *Microstructure and bonding mechanisms in cold spray coatings*. Mater. Sci. Technol. (United Kingdom)
81. Viscusi A, Bruno M, Esposito L, Testa G (2020) An experimental/numerical study of bonding mechanism in cold spray technology for metals. *Int J Adv Manuf Technol*. <https://doi.org/10.1007/s00170-020-06060-9>
82. Chen C, Xie Y, Huang R, et al (2018) On the role of oxide film's cleaning effect into the metallurgical bonding during cold spray. *Mater Lett*. <https://doi.org/10.1016/j.matlet.2017.09.024>
83. Grujicic M, Zhao CL, DeRosset WS, Helfritsch D (2004) Adiabatic shear instability based mechanism for particles/substrate bonding in the cold-gas dynamic-spray process. *Mater Des*. <https://doi.org/10.1016/j.matdes.2004.03.008>
84. Tiamiyu AA, Sun Y, Nelson KA, Schuh CA (2021) Site-specific study of jetting, bonding, and local deformation during high-velocity metallic microparticle impact. *Acta Mater*. <https://doi.org/10.1016/j.actamat.2020.10.057>
85. Liu H, Liu J, Ding Y, et al (2020) The behaviour of thermoplastic and thermoset carbon fibre composites subjected to low-velocity and high-velocity impact. *J Mater Sci*. <https://doi.org/10.1007/s10853-020-05133-0>
86. Birca A, Gherasim O, Grumezescu V, Grumezescu AM (2019) Introduction in thermoplastic and thermosetting polymers. In: *Materials for Biomedical Engineering: Thermoset and Thermoplastic Polymers*

87. Sun C, Zhou X, Xie C, Liu B (2020) Investigating hard/soft combinations of cold spraying by Eulerian approach. *Surf Eng.* <https://doi.org/10.1080/02670844.2019.1710036>
88. Wu G, Xie P, Yang H, et al (2021) A review of thermoplastic polymer foams for functional applications. *J. Mater. Sci.*
89. Bae G, Xiong Y, Kumar S, et al (2008) General aspects of interface bonding in kinetic sprayed coatings. *Acta Mater* 56:4858–4868. <https://doi.org/10.1016/j.actamat.2008.06.003>
90. Zhang Y, Xu X (2020) Machine learning glass transition temperature of polymers. *Heliyon.* <https://doi.org/10.1016/j.heliyon.2020.e05055>
91. Qiao Y, Salviato M (2019) Strength and cohesive behavior of thermoset polymers at the microscale: A size-effect study. *Eng Fract Mech* 213:100–117. <https://doi.org/10.1016/j.engfracmech.2019.03.033>
92. Che H, Vo P, Yue S (2017) Metallization of carbon fibre reinforced polymers by cold spray. *Surf Coatings Technol.* <https://doi.org/10.1016/j.surfcoat.2017.01.083>
93. Che H, Vo P, Yue S (2017) Metallization of various polymers by cold spray. In: *Proceedings of the International Thermal Spray Conference.* pp 98–103
94. Liberati AC, Che H, Vo P, Yue S (2021) Influence of Secondary Component Hardness When Cold Spraying Mixed Metal Powders on Carbon Fiber Reinforced Polymers. *J Therm Spray Technol.* <https://doi.org/10.1007/s11666-021-01197-9>
95. Raletz F, Vardelle M, Ezo'o G (2006) Critical particle velocity under cold spray conditions. *Surf Coatings Technol.* <https://doi.org/10.1016/j.surfcoat.2006.04.061>
96. Canales H, Cano IG, Dosta S (2020) Window of deposition description and prediction of deposition efficiency via machine learning techniques in cold spraying. *Surf Coatings Technol.* <https://doi.org/10.1016/j.surfcoat.2020.126143>
97. Yin S, Suo X, Su J, et al (2014) Effects of substrate hardness and spray angle on the deposition behavior of cold-sprayed Ti particles. In: *Journal of Thermal Spray Technology*
98. Xie Y, Chen C, Planche MP, et al (2019) Strengthened Peening Effect on Metallurgical Bonding Formation in Cold Spray Additive Manufacturing. *J Therm Spray Technol.* <https://doi.org/10.1007/s11666-019-00854-4>
99. Liberati AC, Che H, Vo P, Yue S (2020) Observation of an Indirect Deposition Effect while Cold Spraying Sn-Al Mixed Powders onto Carbon Fiber Reinforced Polymers. *J Therm Spray Technol.* <https://doi.org/10.1007/s11666-019-00967-w>
100. Schmidt T, Gärtner F, Assadi H, Kreye H (2006) Development of a generalized parameter window for cold spray deposition. *Acta Mater* 54:729–742. <https://doi.org/10.1016/j.actamat.2005.10.005>
101. Tsai JT, Akin S, Zhou F, et al (2021) Establishing a Cold Spray Particle Deposition Window on Polymer Substrate. *J. Therm. Spray Technol.*
102. Assadi H, Kreye H, Gärtner F, Klassen T (2016) Cold spraying – A materials perspective. *Acta Mater* 116:382–407. <https://doi.org/10.1016/j.actamat.2016.06.034>
103. Bortolussi V, Figliuzzi B, Willot F, et al (2020) Electrical Conductivity of Metal–Polymer Cold Spray Composite Coatings onto Carbon Fiber-Reinforced Polymer. *J Therm Spray Technol.* <https://doi.org/10.1007/s11666-020-00999-7>
104. Wong W, Vo P, Irissou E, et al (2013) Effect of particle morphology and size distribution on cold-sprayed pure titanium coatings. *J Therm Spray Technol.* <https://doi.org/10.1007/s11666-013-9951-6>
105. Barr CJ, Wang L, Coffey JK, Daver F (2017) Influence of surface texturing on scratch/mar visibility for polymeric materials: a review. *J. Mater. Sci.*
106. Rubino F, Astarita A, Carlone P (2018) Thermo-mechanical finite element modeling of the laser treatment of titanium cold-sprayed coatings. *Coatings.* <https://doi.org/10.3390/coatings8060219>
107. Astarita A, Mandolino C, Lertora E, et al (2017) Effect of fibre laser marking on surface properties and corrosion resistance of a Fe-Ni-Cr alloy. In: *AIP Conference Proceedings*

108. Papyrin A (2001) Cold spray technology. *Adv Mater Process*
109. Gholampour A, Ozbakkaloglu T (2020) A review of natural fiber composites: properties, modification and processing techniques, characterization, applications. *J. Mater. Sci.*
110. Rokni MR, Widener CA, Champagne VK, Crawford GA (2015) Microstructure and mechanical properties of cold sprayed 7075 deposition during non-isothermal annealing. *Surf Coatings Technol.* <https://doi.org/10.1016/j.surfcoat.2015.07.016>
111. Li CJ, Li WY (2003) Deposition characteristics of titanium coating in cold spraying. *Surf Coatings Technol.* [https://doi.org/10.1016/S0257-8972\(02\)00919-2](https://doi.org/10.1016/S0257-8972(02)00919-2)
112. Steenkiste THV, Smith JR, Teets RE (2002) Aluminum coatings via kinetic spray with relatively large powder particles. *Surf Coatings Technol.* [https://doi.org/10.1016/S0257-8972\(02\)00018-X](https://doi.org/10.1016/S0257-8972(02)00018-X)
113. Gärtner F, Stoltenhoff T, Voyer J, et al (2006) Mechanical properties of cold-sprayed and thermally sprayed copper coatings. *Surf Coatings Technol.* <https://doi.org/10.1016/j.surfcoat.2005.10.007>
114. Raabe D, Sun B, Kwiatkowski Da Silva A, et al (2020) Current Challenges and Opportunities in Microstructure-Related Properties of Advanced High-Strength Steels. *Metall Mater Trans A Phys Metall Mater Sci* 51:5517–5586. <https://doi.org/10.1007/s11661-020-05947-2>
115. Che H, Liberati A, Vo P, Yue S (2018) Cold spray of mixed sn-zn and sn-al powders on carbon fiber reinforced polymers. In: *Materials Science Forum*. pp 1892–1897
116. Irissou E, Legoux JG, Arsenault B, Moreau C (2007) Investigation of Al-Al<sub>2</sub>O<sub>3</sub> cold spray coating formation and properties. In: *Proceedings of the International Thermal Spray Conference*
117. Alghadi AM, Tirkes S, Tayfun U (2020) Mechanical, thermo-mechanical and morphological characterization of ABS based composites loaded with perlite mineral. *Mater Res Express.* <https://doi.org/10.1088/2053-1591/ab551b>
118. Goldbaum D, Shockley JM, Chromik RR, et al (2012) The effect of deposition conditions on adhesion strength of Ti and Ti6Al4V cold spray splats. *J. Therm. Spray Technol.*
119. Prisco U, Squillace A, Astarita A, Carrino L (2018) Morphology of titanium coatings deposited through single pass cold spraying. *Mater Manuf Process.* <https://doi.org/10.1080/10426914.2016.1198035>
120. Stenson C, McDonnell KA, Yin S, et al (2018) Cold spray deposition to prevent fouling of polymer surfaces. *Surf Eng* 34:193–204. <https://doi.org/10.1080/02670844.2016.1229833>
121. Kabir SMF, Mathur K, Seyam A-FM (2020) A critical review on 3D printed continuous fiber-reinforced composites: History, mechanism, materials and properties. *Compos Struct* 232:111476. <https://doi.org/10.1016/j.compstruct.2019.111476>
122. Sanei SH, Popescu D (2020) 3D-Printed Carbon Fiber Reinforced Polymer Composites: A Systematic Review. *J. Compos. Sci.* 4
123. Stoltenhoff T, Kreye H, Richter HJ (2002) An analysis of the cold spray process and its coatings. *J Therm Spray Technol* 11:542–550. <https://doi.org/10.1361/105996302770348682>
124. Rokni MR, Feng P, Widener CA, Nutt SR (2019) Depositing Al-Based Metallic Coatings onto Polymer Substrates by Cold Spray. *J Therm Spray Technol* 28:1699–1708. <https://doi.org/10.1007/s11666-019-00911-y>
125. Che H, Chu X, Vo P, Yue S (2018) Metallization of Various Polymers by Cold Spray. *J Therm Spray Technol* 27:169–178. <https://doi.org/10.1007/s11666-017-0663-1>
126. Giraud D, Borit F, Guipont V, et al (2012) Metallization of a polymer using cold spray: Application to aluminum coating of polyamide 66. In: *Proceedings of the International Thermal Spray Conference*. pp 265–270
127. Ganesan A, Yamada M, Fukumoto M (2013) Cold spray coating deposition mechanism on the thermoplastic and thermosetting polymer substrates. In: *Journal of Thermal Spray Technology*. pp 1275-1282 <https://doi.org/10.1007/s11666-013-9984->
128. Viscusi A, Perna AS, Astarita A, et al (2019) Experimental study of cold sprayed metallic coatings on thermoplastic matrix composites. In: *Key Engineering Materials*. pp 68–73

129. Bielousova O, Kocimski J, Maev RG, et al (2016) Localisation of deformation in cold gas dynamic spraying. *Surf Eng.* <https://doi.org/10.1179/1743294415Y.0000000059>
130. Mejlej VG, Falkenberg P, Türck E, Vietor T (2017) Optimization of Variable Stiffness Composites in Automated Fiber Placement Process using Evolutionary Algorithms. In: *Procedia CIRP*
131. Che H, Chu X, Vo P, Yue S (2017) Cold spray of mixed metal powders on carbon fibre reinforced polymers. *Surf Coatings Technol* 329:232–243. <https://doi.org/10.1016/j.surfcoat.2017.09.052>
132. Goyal T, Walia RS, Sidhu TS (2012) Effect of parameters on coating density for cold spray process. *Mater Manuf Process.* <https://doi.org/10.1080/10426914.2011.566906>
133. Goyal T, Walia RS, Sidhu TS (2012) Study of coating thickness of cold spray process using Taguchi method. *Mater Manuf Process.* <https://doi.org/10.1080/10426914.2011.564249>
134. Li WY, Zhang C, Guo XP, et al (2008) Effect of standoff distance on coating deposition characteristics in cold spraying. *Mater Des.* <https://doi.org/10.1016/j.matdes.2007.02.005>
135. Bakshi SR, Laha T, Balani K, et al (2007) Effect of carrier gas on mechanical properties and fracture behaviour of cold sprayed aluminium coatings. *Surf Eng.* <https://doi.org/10.1179/174329407X161618>
136. Raelison RN, Aubignat E, Planche MP, et al (2016) Low pressure cold spraying under 6 bar pressure deposition: Exploration of high deposition efficiency solutions using a mathematical modelling. *Surf Coatings Technol.* <https://doi.org/10.1016/j.surfcoat.2016.05.068>
137. Li WY, Liao H, Li CJ, et al (2007) Numerical simulation of deformation behavior of Al particles impacting on Al substrate and effect of surface oxide films on interfacial bonding in cold spraying. *Appl Surf Sci.* <https://doi.org/10.1016/j.apsusc.2006.11.020>
138. Kang K, Yoon S, Ji Y, Lee C (2008) Oxidation dependency of critical velocity for aluminum feedstock deposition in kinetic spraying process. *Mater Sci Eng A.* <https://doi.org/10.1016/j.msea.2007.09.010>
139. Li CJ, Li WY, Liao H (2006) Examination of the critical velocity for deposition of particles in cold spraying. *J. Therm. Spray Technol.*
140. Gilmore DL, Dykhuizen RC, Neiser RA, et al (1999) Particle velocity and deposition efficiency in the cold spray process. *J Therm Spray Technol.* <https://doi.org/10.1361/105996399770350278>
141. Ye H, Wang J (2014) Preparation of aluminum coating on Lexan by cold spray. *Mater Lett* 137:21–24. <https://doi.org/10.1016/j.matlet.2014.08.119>
142. Prisco U (2015) Size-dependent distributions of particle velocity and temperature at impact in the cold-gas dynamic-spray process. *J Mater Process Technol.* <https://doi.org/10.1016/j.jmatprotec.2014.09.013>
143. Kromer R, Danlos Y, Aubignat E, et al (2017) Coating deposition and adhesion enhancements by laser surface texturing—metallic particles on different classes of substrates in cold spraying process. *Mater Manuf Process* 32:1642–1652. <https://doi.org/10.1080/10426914.2017.1364750>
144. Huang R, Fukunuma H (2012) Study of the influence of particle velocity on adhesive strength of cold spray deposits. In: *Journal of Thermal Spray Technology*
145. Varinor GD, Guipont V, Giraud D, et al (2012) Metallization of a polymer using cold spray: Application to aluminum coating of polyamide 66 Characterization and modeling of coating properties and microstructure evolution View project Metallization of a Polymer Using Cold Spray: Application to Aluminum
146. Trexler MD, Carter R, de Rosset WS, et al (2012) Cold Spray Fabrication of Refractory Materials for Gun Barrel Liner Applications. *Mater Manuf Process* 27:820–824. <https://doi.org/10.1080/10426914.2011.648690>
147. Viscusi A, Della Gatta R, Delloro F, et al (2021) A novel manufacturing route for integrated 3D-printed composites and cold-sprayed metallic layer. *Mater Manuf Process.* <https://doi.org/10.1080/10426914.2021.1942908>
148. Della Gatta R, Viscusi A, Perna AS, et al (2021) Cold spray process for the production of AlSi10Mg coatings on glass fibers reinforced polymers. *Mater Manuf Process* 36:106–121. <https://doi.org/10.1080/10426914.2020.1813895>
149. Moridi A, Hassani-Gangaraj SM, Guagliano M, Dao M (2014) Cold spray coating: review of material systems and future perspectives. *Surf Eng* 30:369–395. <https://doi.org/10.1179/1743294414Y.0000000270>

150. Schmidt T, Gärtner F, Assadi H, Kreye H (2006) Development of a Generalized Parameter Window for Cold Spray Deposition. *Acta Mater* 54:. <https://doi.org/10.1016/j.actamat.2005.10.005>
151. Viscusi A, Astarita A, Genna S, Leone C (2018) On the influence of different superficial laser texturing on the deposition of powders through cold spray process. *Trans Inst Met Finish* 96:34–40. <https://doi.org/10.1080/00202967.2018.1403096>
152. Assadi H, Gärtner F, Stoltenhoff T, Kreye H (2003) Bonding mechanism in cold gas spraying. *Acta Mater* 51:4379–4394. [https://doi.org/10.1016/S1359-6454\(03\)00274-X](https://doi.org/10.1016/S1359-6454(03)00274-X)
153. Ko KH, Choi JO, Lee H (2016) The interfacial restructuring to amorphous: A new adhesion mechanism of cold-sprayed coatings. *Mater Lett* 175:13–15. <https://doi.org/10.1016/j.matlet.2016.03.132>
154. Luo XT, Li CX, Shang FL, et al (2014) High velocity impact induced microstructure evolution during deposition of cold spray coatings: A review. *Surf. Coatings Technol.* 254:11–20
155. Champagne VK, West MK, Reza Rokni M, et al (2016) Joining of Cast ZE41A Mg to Wrought 6061 Al by the Cold Spray Process and Friction Stir Welding. *J Therm Spray Technol* 25:143–159. <https://doi.org/10.1007/s11666-015-0301-8>
156. Hassani-Gangaraj M, Veysset D, Champagne VK, et al (2018) Adiabatic shear instability is not necessary for adhesion in cold spray. *Acta Mater* 158:430–439. <https://doi.org/10.1016/j.actamat.2018.07.065>
157. Bae G, Jang J Il, Lee C (2012) Correlation of particle impact conditions with bonding, nanocrystal formation and mechanical properties in kinetic sprayed nickel. *Acta Mater* 60:3524–3535. <https://doi.org/10.1016/j.actamat.2012.03.001>
158. Grujicic M, Zhao CL, DeRosset WS, Helfritsch D (2004) Adiabatic shear instability based mechanism for particles/substrate bonding in the cold-gas dynamic-spray process. *Mater Des* 25:681–688. <https://doi.org/10.1016/j.matdes.2004.03.008>
159. Champagne VK (2007) V.K. Champagne, *The Cold Spray Materials Deposition Process. Fundamental an Applications*, 2007.
160. Leland TW, Mansoori G a (1986) *Basic Principles of Classical and Statistical Thermodynamics*. 1–35
161. Faizan-Ur-Rab M, Zahiri SH, Masood SH, et al (2016) Application of a holistic 3D model to estimate state of cold spray titanium particles. *Mater Des* 89:1227–1241. <https://doi.org/10.1016/j.matdes.2015.10.075>
162. Johnson KL (1989) *Contact Mechanics*. Cambridge University Press, Cambridge
163. Jackson RL, Green I, Marghitu DB (2010) Predicting the coefficient of restitution of impacting elastic-perfectly plastic spheres. *Nonlinear Dyn* 60:217–229. <https://doi.org/10.1007/s11071-009-9591-z>
164. Dieter GE (2011) *Mechanical metallurgy*. McGraw-Hill
165. Morye SS, Hine PJ, Duckett RA, et al (2000) Modelling of the energy absorption by polymer composites upon ballistic impact. *Compos Sci Technol* 60:2631–2642. [https://doi.org/10.1016/S0266-3538\(00\)00139-1](https://doi.org/10.1016/S0266-3538(00)00139-1)
166. Della Gatta R, Viscusi A, Perna AS, et al (2021) Feasibility of steel powder deposition on composites through cold spray. *Mater Manuf Process* 36:281–291. <https://doi.org/10.1080/10426914.2020.1832693>

## List of figures

**Fig. 1** - Number of published papers

**Fig. 2** Working schemes of high-pressure **a** and low-pressure **b** cold spray

**Fig. 3** - Schematic representation of the interaction of a cold-sprayed Cu particle on **a** PVC, **b** epoxy resin [64]

**Fig. 4** - SEM images of cold sprayed Cu powder on **a** HDPE and **b** PTFE [60]

**Fig. 5** - Optical micrographs of cold sprayed Cu coatings at 425 °C at 1.0 MPa on **a** ABS and **b** PEEK [54]

**Fig. 6** - Distribution of temperature and effective plastic strain of a single Cu particle depositing onto PEEK substrate at different gas pressures [49]

**Fig. 7** - SEM images showing voids and cavities at the impact spots on CFRP substrate left by copper particles at two different gas temperatures: 425 °C (on the left) and 250 °C (on the right) [43]

**Fig. 8** - The schematization of crack filling mechanism for thermosetting bonding [92]

**Fig. 9** - SEM acquisition of a Sn-10Al5083 coating on CFRP **a** before spraying and **b** after spraying and peeling [94]

**Fig. 10** - Schematization of the cold spray window of deposition for polymer [93]

**Fig. 11** - Illustrative sketch of indirect deposition mechanisms: **a** re-deposition of rebounding powders and **b** deposition of laterally swept powders [99]

**Fig. 12** - Prediction of the deposition behavior for different typologies of metallic powders cold sprayed on polymer substrates [73]

**Fig. 13** - Micrographs of cold sprayed aluminium coating on **a** tin interlayer and **b** enlargement of the selected area [51]

**Fig. 14** - Schematic representation of cold sprayed particle interaction with polymer substrate: **a** dendritic copper and **b** tin [64].

**Fig. 15** - Post-treated pictures of **a** mix of M/F/M Cu and **b** mix of L/F/L Cu [42]

**Fig. 16** - Optical micrographs of the cross-section for copper coating: **a** low speed 5 bar and **b** high speed 30 bar nozzle inlet pressure onto glass-fiber reinforced composite [73]

**Fig. 17** - Deposition efficiency of various powders with respect to process gas temperature and pressure: **a** 1 MPa, **b** 2 MPa, **c** 3 MPa [64]

**Fig. 18** - SEM images showing copper particles cold sprayed onto PEEK at **a** 425 °C and **b** 350 °C, and **c** the craters at the PEEK surface at 350 °C [43]

**Fig. 19** - Numerical and experimental observations of a single particle impact on planar **a** and textured **b** PEEK surface [57]

**Fig. 20** - **a** Top and **b** cross-section micrographs of the CFRP samples after cold spray of Sn powder

**Fig. 21** - Electrical conductivity measurements for various coatings cold sprayed at 300°C, 60 psi [53]

**Fig. 22** - Volume resistivity of aluminum cold sprayed onto CFRP [72]

**Fig. 23** - Coating thickness of **a** 7075 Al with 1, 3, and 5 passes, and **b** pure Al with 2, 4, and 6 passes [40]

**Fig. 24** - Exemplificative sketch of laminate build-up in two different configurations.

**Fig. 25** - SEM acquisition and particle size distribution of AlSi10Mg **a**) **b**) and Steel 316L **c**) **d**) powders

**Fig. 26** - Scheme of different direction of coating characterization.

**Fig. 27** - Top view acquisition with SEM **(a)** and ImageJ **(b)**.

**Fig. 28**- Profile extraction with LeicaMap for maximum coating height analysis.

**Fig. 29** - Schematization of hybrid composite structure made of basalt-epoxy substrate, PLA film and AlSi10Mg cold sprayed powder.

**Fig. 30** - Simple sketch of FFF technology for the 3D-printed polymer-based materials.

**Fig. 31** - Scan pattern for the panels' manufacturing.

**Fig. 32** - Layup sequences and stratification of 3D-printed composite substrates. (For the clarity of the picture, the layup sequence repetition was not drawn throughout the panel thickness for reinforced laminates).

**Fig. 33** - Illustrative sketch of Onyx-based matrix printing strategy by varying the infill density: **a**) 30%, **b**) 40%, **c**) 50%

**Fig. 34** - Simple scheme of a 0/90 symmetric configuration of reinforced samples. The figure highlights the superficial matrix thickness of the outermost surfaces: **a**) one layer, **b**) two layers; **c**) three layers

**Fig. 35** - Coating tracks made of AlSi10Mg powders produced by CS on both the pure Onyx (3D-O<sub>1</sub>) and the reinforced (3D-F<sub>1</sub>) specimens with one layer of matrix on the outermost surfaces

**Fig. 36** - Cross-section photography of the distorted panel; *d* is the distance between the lowest and the highest points of the sample

**Fig 37** - Top view acquisition of AlSi10Mg coatings sprayed with air on GFRP-1 laminate **(a)** **(b)** **(c)** and GFRP-2 laminate **(d)** **(e)** **(f)** at fixed pressure  $p = .5$  MPa.

**Fig 38** - Top view acquisition of an AlSi10Mg coating sprayed with nitrogen (a) and air (b) at fixed pressure  $p = .6$  MPa and standoff SoD = 35 mm.

**Fig 39** - Top views of boundary (a) and bulk (b) region of a single sprayed track.

**Fig 40** - Surface coverage measurements.

**Fig. 41** - Maximum coating height of AlSi10Mg samples sprayed on GFRP-1 with air (a), GFRP-2 with air (b) and GFRP-2 with nitrogen (c).

**Fig. 42** - Cross-section of AlSi10Mg coating on GFRP-2 sprayed with air at fixed pressure  $p=0.6$  MPa and SoD=35 mm.

**Fig. 43** -Coating thickness of AlSi10Mg samples sprayed on GFRP-1 with air (a), GFRP-2 with air (b) and GFRP-2 with nitrogen (c).

**Fig. 44** -Cross-section of AlSi10Mg coating on GFRP-1 sprayed with air at fixed pressure  $p=0.5$  MPa and SoD=25 mm.

**Fig. 45** - SEM acquisition of AlSi10Mg coating.

**Fig. 46** - Influence of SoD on coating thickness at 0.5 MPa (a) and 0.6 MPa (b).

**Fig. 47** - Influence of SoD on surface coverage at 0.5 MPa (a) and 0.6 MPa (b).

**Fig. 48** - SEM magnification of steel coating on GFRP-2 S.O.=25 mm  $p=5$  bar a) boundary b) bulk.

**Fig. 49** - SEM magnification of boundary zones of steel coatings on GFRP-2 at  $p=0.5$  MPa and a) S.O.=20mm, b) S.O.=25mm, c) S.O.=35mm.

**Fig. 50** - Surface Coverage measurements.

**Fig. 51** - Coating Height measurements.

**Fig. 52** - Penetration Depth measurements.

**Fig. 53** - Sem magnification of cross-section of steel coating.

**Fig 54** - SEM cross-section images of untreated (a) and PLA treated (b) metallised BS-epoxy surfaces

**Fig. 55**- Load-displacement curves comparison for three impact energy levels ( $U = 10$  J, 20 J, 30 J) relative to neat composites systems (neat).

**Fig. 56** - Load-displacement curves comparison for three impact energy levels ( $U = 10$  J, 20 J, 30 J) relative to coated composites systems (coated).

**Fig. 57** - Load-displacement comparison between coated and neat composite at  $U = 10, 20, 30$  J.

**Fig. 58** - Percentage ratio between the absorbed energy,  $U_a$ , and the impact energy,  $U$ , for the three tested conditions and for both neat and coated samples.

**Fig. 59** - Absorbed energy trend variation for the three tested conditions and for both neat and coated samples.

**Fig. 60** - Indentation depth. measurements for the three tested conditions and for both neat and coated samples.

**Fig. 61** - C-scan acquisition for both neat and coated samples for the three tested conditions

**Fig. 62** - Delamination area,  $A$ , for the three tested conditions and for both neat and coated samples.

**Fig. 63** - Real picture of 3D-printed laminate (FO configuration) reporting the confocal microscope observations of both the front and the back faces of the panel.

**Fig. 64** - Cross-section SEM image of a coated specimen. The particles are completely locked into the surface texture.

**Fig. 65** - Optical observations of the boundary portion of a coated specimen. The surface texturing is evident with the particles get entangled in the space between two contiguous polymer-based filaments.

**Fig.66** - Surface coverage for different substrates and temperatures.

**Fig.66** - Surface coverage for different substrates and temperatures.

**Fig. 67** - SEM images of the surface of the coatings for the three layup sequences a) FO, b) LFC and c) HFC, respectively. The temperature was set at 250°C.

**Fig. 68** - Coating height evaluation for different deposition temperature values on different composite layup sequences.

- Fig. 69** - Confocal acquisitions of the top-surface of the uncoated pure Onyx samples
- Fig. 70** - Confocal acquisitions of the top surface of the coated pure Onyx samples highlighting the infill density
- Fig. 71** - Height parameters from confocal analyses
- Fig. 72** - Pure Onyx panels profiles after the cold spray deposition of AlSi10Mg powder
- Fig. 73** - Results of the substrate distortion of pure Onyx panels calculated through Eq. 1
- Fig. 74** - SEM top-view micrographs of the coated surfaces
- Fig. 75** - Particles splat size from SEM images. The dotted lines evidence the mean splat size
- Fig. 76** - Splat size distribution analysis for 3D-O<sub>2,30</sub> e 3D-F<sub>2,30</sub> samples
- Fig. 77** - Results of the adhesion strength tests for both pure Onyx (a) and reinforced (b) samples
- Fig. 78** - Area fractions of the dolly surface for the pure Onyx samples
- Fig. 79** - Effect of the fibres on cold spray deposition. a) Mean coating height of pure Onyx and fibre reinforced panels; b) percentage of deformed particles due to deposition; c) adhesion strength values
- Fig. 80** SEM images of 3D-F<sub>3,40</sub> and 3D-O<sub>3,40</sub> samples. The penetration depth is calculated as the distance of the deepest point reached by the coating from the substrate main plane
- Fig. 81** - Influence of the infill density on CS deposition. a) Mean coating height; b) percentage of deformed particles; c) adhesion strength values
- Fig. 82** - Influence of the superficial matrix layer thickness. a) Mean coating height; b) percentage of deformed particles; c) adhesion strength values
- Fig. 83** - Representative scheme describing the energy balance.
- Fig. 84** - Deformation of a single particle upon impact.  $F$  is the compressive force applied to the particle
- Fig. 85** - Schematic side view of a fibre in a composite deformed during a ballistic impact
- Fig. 86** - Schematic description of the main energy contribution to the bonding in CS process
- Fig. 87** - Positioning of aluminum dolly for adhesion test on a) unreinforced substrate b) reinforced substrate.
- Fig. 88** - Adhesion tests results for a) unreinforced substrates b) reinforced substrates.
- Fig. 89** - Cold spray deposition of aluminum particles on unreinforced polymeric substrates varying the impact velocity: a)  $v_2 = 225$  m/s (Poor deposition); b)  $v_3 = 400$  m/s (effective deposition).
- Fig. 90** - Macrograph of CS deposition on fiber-reinforced composite substrates at  $v_3 = 550$  m/s showing erosion of the substrate.
- Fig. 91** - Sketches of the impacts for increasing  $\Delta E$  values (a given  $\Delta E$  for each row in the figure) with different substrates: a) impact of a particle on a pure polymeric substrate, b) impact of a particle on a composite substrate.
- Fig. 92** - Predictive simulations through *Vi-Pe-R-A* equation showing the trend of  $Ep$  and  $Ea$  with the particle size for three different impact velocities:  $v_1 = 100$  m/s,  $v_2 = 225$  m/s and  $v_3 = 400$  m/s.
- Fig. 93** - Plot of  $Ep$  and  $Ea$  by varying the particle impact velocity for three different powder materials: a) aluminum b) steel c) copper.
- Fig. 94** - Deposition window when cold spraying aluminum particles (30  $\mu\text{m}$ ) on PP substrate.
- Fig. 95** - Plot of  $Ep$  and  $Ea$  by varying the fiber volume percentage for two different impact velocities,  $v_1 = 225$  m/s and  $v_2 = 304$  m/s. Aluminum particles on reinforced PP substrate.

## List of tables

**Table 1** - List of papers on CS deposition on polymers in the last until 2019

**Table 2** - Mean value of the thickness of the superficial layer for the two typologies of GFRP.

**Table 3** - GFRP sample with different parameters combination

**Table 4** – 3D substrate with different reinforcement infill

**Table 5** - 3D-panels with different matrix infill and different superficial matrix layer

**Table 6** - Main parameters required for the implementation of the model.

**Table 7** - Experimental vs. theoretical results for cold spray deposition of aluminum particles on unreinforced polymeric substrates.

**Table 8** - Experimental vs. theoretical results for cold spray deposition of aluminum particles on fiber-reinforced polymer substrates.

**Table 9** - Results from the literature cases: deposition of copper on ABS and PEEK substrates under different processing conditions.

**Table 10** - Results from the literature cases: deposition of powders with different dimensions on a fiber-reinforced polymer.

**Table 11** - Single energy contribution to particle adhesion for an aluminum particle on composite and pure polymeric substrate ( $v = 400$  m/s), where  $EPLA(s)$  and  $EPLA(p)$  are the energy values required to plastically deform the substrate and the particle, respectively;  $Eload$  is the energy required for the loading of the fibers and  $ET$  is the thermal energy.